ELUCIDATION OF FUNDAMENTAL CHEMICAL SYSTEMS THROUGH THE USE OF HIGH-LEVEL *AB INITIO* QUANTUM CHEMICAL METHODS

by

PRESTON R. HOOBLER

(Under the Direction of Henry F. Schaefer III)

ABSTRACT

A goal of any scientist is to gain an understanding for the subject matter at hand. Within quantum chemistry understanding can be achieved through the in-depth study of small systems which retain key features of larger, more chemically interesting species. Within combustion chemistry, the n-propylperoxy radical is the smallest peroxy radical system with an energetically favorable pathway to the formation of the all-important hydroperoxyalkyl radical, a species that is key to low-temperature combustion phenomena. The five rotamers that are formed within the deep potential energy well as the n-propylperoxy radical forms are considered. Focal point analysis and second order vibrational perturbation theory (VPT2) are utilized to differentiate the energies and vibrational frequencies of these nearly isoenergetic species. They hydrogen cyanide dimer represents a small linear system which exhibits hydrogen-bonding phenomena. Results are obtained for this system utilizing a robust combination of method and basis set. The effect of substitution with common isotopes upon vibrational frequencies is investigated using VPT2. Finally, the consideration of simple aluminum (I) compounds, whose valence electron structure mimics that of carbenes are considered. The effect of several substituents, at varying degrees of electrophilicity are investigated. In order to determine the relative energetic favorability, two different schemes, one isodesmic the other hypohomodesmotic are used to determine evaluate the relative energies of formation of different carbene derivatives

INDEX WORDS: peroxy radicals, combustion, hydrogen bonding, second order vibrational perturbation theory, aluminyl anion, coupled-cluster theory, focal point analysis

ELUCIDATION OF FUNDAMENTAL CHEMICAL SYSTEMS THROUGH THE USE OF HIGH-LEVEL *AB INITIO* QUANTUM CHEMICAL METHODS

by

PRESTON R. HOOBLER

B.S., Huntington University, 2014

A Dissertation Submitted to the Graduate Faculty
of the University of Georgia in Partial Fulfillment
of the Requirements for the Degree

Doctor of Philosophy

Athens, Georgia

2018

ELUCIDATION OF FUNDAMENTAL CHEMICAL SYSTEMS THROUGH THE USE OF HIGH-LEVEL *AB INITIO* QUANTUM CHEMICAL METHODS

by

PRESTON R. HOOBLER

Major Professor: Henry F. Schaefer III

Committee: Gary Douberly

Geoffrey Smith

Electronic version approved:

Suzanne Barbour

Dean of the Graduate School

University of Georgia

December 2018

ACKNOWLEDGEMENTS

My first and foremost acknowledgment goes to my Lord, Jesus Christ, who has sustained me through this time. He has taught me that his plans for my life are complete, even if I can't see the end of them. He has also used wonderful people in my life during this time, who deserve to be thanked for being used by Him.

The second acknowledgment goes to my wonderful, lovely wife Abbey. She has supported me through the roughest moments, of which there are plenty when pursuing your doctorate. Moreover, she has shown me grace that I would not have shown myself and pointed me back to our Lord and his grace. Not to mention that she put up with me scheduling my prospectus on her birthday. I am forever sorry that this happened. I hope we're laughing about that someday. Abbey, I love you very much.

My parents were huge supports to me during the process. Mom, I love you and thank you for your support. Dad, it was a joy growing in our relationship over the past few years. As I've started my own household, you have been an incredible example to me. You've been a great example of trusting in hard times and moving forward even though it looks bleak. You have talked me off the proverbial ledge many times. Dad, I love you.

To my siblings, siblings-in-law, in-laws, and my wonderful niece. Times I've spent with you as a break from the process of pursuing this degree have been some of the sweetest times. I love you all.

To the Faith Presbyterian family and particularly Steven Brooks, thank you. Steven, you have been a wonderful friend and accountability partner in my life. Thank you for all of your support.

To my fellow CCQC students. You have been encouragement when I needed it. You have been my mentors, mentees and everything in between. This experience was made because of you. I thank you.

To Dr. Turney, I can't thank you enough for your patience and persistence with me. I have come to you many times with frustrations and received kind patient answers. Thank you.

To Dr. Schaefer, I often describe my process of coming to graduate school as being plucked out of an Indiana cornfield. Indeed, I had no thoughts of pursuing a Ph.D. until you came and met with me at HU. You saw in me something that I did not see in myself and have pulled out of me something I did not know was there. My life is changed because of the generosity you have shown to me and the belief you've shown in me. Thank you.

TABLE OF CONTENTS

CHAPTER 1

INTRODUCTION AND LITERATURE REVIEW

1.1 Hartree–Fock Theory

Hartree–Fock theory is a way of determining the electronic wavefunction of a many electron system as the product of many one-electron wavefunctions. The start of the theory comes from the Schrödinger equation written famously as follows:

$$\hat{H}\Psi = E\Psi \tag{1.1}$$

The wavefunction Ψ is expressed in the form of a Slater determinant.[1] The Slater determinant for a wavefunction of N electrons in N spin orbitals (ψ) has the form:

$$|\Psi\rangle = \frac{1}{\sqrt{N!}} \begin{vmatrix} \psi_1(x_1) & \psi_2(x_1) & \cdots & \psi_N(x_1) \\ \psi_1(x_2) & \psi_2(x_2) & \cdots & \psi_N(x_2) \\ \vdots & \vdots & \ddots & \vdots \\ \psi_1(x_N) & \psi_2(x_N) & \cdots & \psi_N(x_N) \end{vmatrix} = |\psi_1(x_1)\psi_2(x_2)\cdots\psi_N(x_N)\rangle \tag{1.2}$$

Where the last form of the wavefunction is written as a product of one electron spin orbitals in Dirac notation. The prefactor in front of the determinant is a normalization factor that accounts for the fact that any electron could be in any orbital. Using this formalism yields a wavefunction as the product of one electron wavefunctions with the proper anti-symmetry due to the fermionic nature of electrons.

In the original equation (1.1), it is impossible to find an exact solution to the wavefunction Ψ but we can approximate it by solving the equation iteratively until our answer sufficiently converges on a solution. The goal is then to find some wavefunction Φ that is a close approximation to the exact wavefunction, Ψ. The new form of the equation is:

$$\hat{H}|\Psi\rangle = E|\Psi\rangle \rightarrow \hat{H}|\Phi\rangle = E|\Phi\rangle \tag{1.3}$$

This is a standard eigenvalue problem. The form of the Hamiltonian operator, known as the Fock operator [1] within Hartree–Fock theory, obtains the energy for an electron i within the system being studied. The Fock term for electron i within:

$$H_i = F_i = -\frac{1}{2}\nabla_i^2 - \sum_N \frac{Z_N}{r_{iN}} + \sum_j \langle ij||ij\rangle \tag{1.4}$$

Where the first two terms are considered the one-electron energy operators, a kinetic energy operator and a term describing the coulombic attraction between electrons an nuclei. These terms can be conveniently be stored in a matrix (**h**). The energy for electron i whose eigenvalue is stored in the matrix (**h**) is:

$$h_i = -\frac{1}{2}\nabla_i^2 - \sum_N \frac{Z_N}{r_{iN}} \tag{1.5}$$

The last term in equation 1.4 is called the r_{12} term. It describes the repulsive forces felt by an electron from the other electrons within the system. Although the first two terms are easily solved for, this term, is very difficult and computationally costly to solve for exactly. As it is written, the term describes the antisymmetrized form of the two electron energy whereby the locations of two electrons are correlated. Often, the two terms that are present are expressed as such:

$$\sum_j \langle ij||ij\rangle = \sum_j \langle ij|ij\rangle - \langle ij|ji\rangle = \sum_j \mathbf{J}_{ij} - \mathbf{K}_{ij} \tag{1.6}$$

Where the **J** and **K** matrices contain the values of the Coulomb and exchange energy terms, respectively. The form of the operator makes it so that no two electrons can occupy the same space. The coulombic forces felt by an electron are said to be the average electronic effect of all electrons.

1.1.1 Solving for the Wavefunction Using Roothaan Equations

Following the example of Szabo and Ostlund in their excellent book "Modern Quantum Chemistry: Introduction to Advanced Electronic Structure Theory", [1] we use a set of one particle basis functions with which to represent our wavefunction. We can call these basis functions χ_i. These basis functions will be used to build up our determinantal wavefunction $|\Phi\rangle$ which is an approximation to the exact wavefunction and a determinant as expressed in equation 1.1. This approximate solution is composed of eigenfunctions ϕ_a which are linear combinations of our basis functions

$$\phi_a = \sum_i C_{ai}\chi_i \qquad . \tag{1.7}$$

We can define a density matrix, which describes the probability of finding an electron in a certain space within our basis. In order to find this probability, we need to sum over the individual probabilities that each electron is found in a space described by a basis function. This can be done two ways, by either restricting the spin state of the functions or not. In the later case, you must treat all alpha orbitals with one summation and all beta orbitals with different summation. The terms of the density matrix which we show here is just a summation of the coefficients between two basis functions:

$$D_{ab} = \sum_i C_{ai} C_{bi}^* \tag{1.8}$$

Where we sum over all of the occupied orbitals (i). These get stored in the density matrix $\mathbf{D}$, which gets updated every iteration of the procedure.

In our given basis, we can represent our wavefunction in terms of these expansion coefficients. In practice, these coefficients are stored in a matrix $\mathbf{C}$ which contains all expansion coefficients, which describe molecular orbitals. These molecular orbitals are one-particle wavefunctions that can spread over an entire molecule. Molecular orbitals are the most important result coming from Hartree–Fock theory. Solving for the appropriate $\mathbf{C}$ becomes the task for solving the Schrödinger equation as we have set up the problem here. We can express the energy of a single eigenfunction (ϕ_a) by using equation 1.6 and the Fock operator ($\hat{F}$)

$$\hat{F}|\sum_i C_{ai}\chi_i\rangle = \varepsilon_a|\sum_i C_{ai}\chi_i\rangle \quad . \tag{1.9}$$

Here we have made the substitution ε for E because the eigenvalues (molecular orbital energies) we obtain using this method are not exact but only approximations. To make our method solvable, we multiply each side the by a complex conjugate of the basis function. To obtain:

$$\sum_i C_{ai}\langle\chi_j^*|\hat{F}|\chi_i\rangle = \varepsilon_a \sum_i C_{ai}\langle\chi_j^*|\chi_i\rangle \tag{1.10}$$

where the coefficients and energies have been factored out from the integrals which only depend upon the basis functions. The final term on the right side represents the overlap between the two basis functions. These terms can be stored in a matrix, often denoted as $\mathbf{S}$. The Fock operator ($\hat{F}$) between the two basis functions can be seen as an element of a matrix known as the Fock matrix $\mathbf{F}$. If we generalize these terms as matrices representing the terms across our entire basis, we obtain the following expression:

$$\mathbf{FC} = \mathbf{SC}\varepsilon \tag{1.11}$$

Where the energies (ε_a) are stored in a diagonal matrix (ε) whose elements are the energies of the eigenfunctions contained as columns within the coefficient matrix. The last preparation we need to do is to make an orthogonalization matrix which will allow us to guarantee that our molecular orbitals will be orthonormal to one another. It turns out that this matrix is the overlap matrix raised to the negative one-half power.

The first step of obtaining a Hartree–Fock solution is to compute the necessary integrals. The necessary integrals include the overlap integrals, the one electron kinetic energy integrals, coulombic attraction integrals between electrons and nuclei, and the two electron repulsion integrals. A thorough review and pedagogical explanation of these integrals can be found in the paper by Murphy, Turney and Schaefer. [2]

The next step is to form an initial guess as to the Fock matrix. There are several ways that this can be done, however, it is common to initialize the Fock matrix as identical to the **h** matrix. This is called the "core" guess. After the first iteration, the density matrix will be refined and the Coulomb and exchange terms will grow in. The Fock matrix, formed at the beginning of each iteration, can be computed as follows.

$$\mathbf{F} = \mathbf{h} + \mathbf{J} - \mathbf{K} \tag{1.12}$$

The resulting Fock matrix is diagonalized and the electronic energy can be computed by summing over all occupied orbitals and adding in nuclear repulsion terms. The same can be accomplished by the following summation:

$$E_{HF} = \sum_i \varepsilon_i + V_N \tag{1.13}$$

Where $f\varepsilon_i$ are the eigenvalues (occupied orbital energies) of the Fock matrix and V_N represents the positive nuclear repulsion terms.

In order to take an iterative step toward the solution of equation 1.10, we need to transform the Fock matrix from our initial basis to the molecular orbital basis.

$$\mathbf{S}^{-\frac{1}{2}}\mathbf{F}\mathbf{C} = \mathbf{S}^{-\frac{1}{2}}\mathbf{S}\mathbf{C} = \mathbf{S}^{\frac{1}{2}}\mathbf{C}\varepsilon \tag{1.14}$$

Next we multiply by the identity matrix (**I**) in the form of ($\mathbf{S}^{-\frac{1}{2}}\mathbf{S}^{\frac{1}{2}}$) resulting in a standard eigenvalue problem:

$$\mathbf{F}'\mathbf{C}' = \mathbf{C}'\varepsilon \tag{1.15}$$

Where the following transformations have taken place:

$$\mathbf{F}' = \mathbf{S}^{-\frac{1}{2}}\mathbf{F}\mathbf{S}^{-\frac{1}{2}} \tag{1.16}$$

Obtaining the eigenfunction matrix of this transformed Fock-Matrix ($\mathbf{F}'$) gives you the new transformed coefficient matrix $\mathbf{C}'$. These can be back transformed into new coefficient matrices, in the initial basis, by multiplying the transformed coefficient matrix by the inverse square of the overlap matrix.

$$\mathbf{C} = \mathbf{S}^{-\frac{1}{2}}\mathbf{C}' \tag{1.17}$$

These back-transformed coefficient matrices are used to form a new density matrix. This density matrix is fed back into the formation of a new **J** and **K** matrices which are used to form a new Fock matrix. The energy is checked again, and if the energy is close enough to the previous iteration, or "self-consistent", the process is over and the current coefficient matrix contains the eigenfunctions which are molecular orbitals. If convergence is not achieved at the current iteration, then the new Fock matrix is obtained and the process continues to another iteration.

1.2 Coupled-Cluster Methods

The problem with Hartree–Fock theory is that it only approximately treats the problem of electron correlation. The wavefunction is not exact because Hartree–Fock theory describes the repulsive forces that electrons exert on each other as an average force, which is not a fully accurate description. Describing more accurately how the electrons approach each other and relax away from each other, known as electron-electron correlation, leads to a better description of the wavefunction.

The exact wavefunction within a basis can represented as the sum of the ground state determinant obtained from Hartree–Fock, mixed in with all excited determinants within the Hartree–Fock solution. For a system of N electrons this requires the treatment of all excitations from singles to N-tuple excitations. The wavefunction (Ψ_{exact}) is then expressed as:

$$|\Psi_{\text{exact}}\rangle = c_0|\Psi_0\rangle + \Sigma_{ia}c_i^a|\Psi_i^a\rangle + \ldots + \Sigma_{ijkl\ldots abcd\ldots}c_{ijkl\ldots}^{abcd\ldots}|\Psi_{ijkl\ldots}^{abcd\ldots}\rangle \tag{1.18}$$

Where the final term considers all possible combinations of exciting all possible electrons from occupied orbitals (i,j,k...) into all possible unoccupied or virtual orbitals (a,b,c...). This method of obtaining the exact wavefunction becomes prohibatively costly as systems of even moderate size are considered. When all possible combinations are considered this is called Full Configuration-Interaction (FCI). Many methods

seek to approximate this limit. One such method is Coupled-Cluster theory[3,4] which treats only certain excitations of the ground state wavefunction. Coupled-Cluster (CC) does systematically converge upon FCI so that as higher orders of excitations are included in the CC treatment, the wavefunction that is obtained approaches that of an FCI treatment. Coupled-Cluster theory seeks to converge toward FCI by explicitly including higher order excitations at lower levels of CC treatment.

Coupled-cluster theory is a "post Hartree–Fock" method because it uses the Hartree–Fock wavefunction as a starting point and describes "excitations" from this wavefunction. This is similar to the FCI approach and indeed, coupled-cluster does converge quickly to the same answer as FCI.

When deriving coupled-cluster equations, we make use of second quantized operators. The two types of these operators are known as creation and annihilation operators. They have the following effects:

$$\hat{a}_i^\dagger|\rangle = |\phi_i\rangle \tag{1.19}$$

and

$$\hat{a}_i|\phi_i\rangle = |\rangle \tag{1.20}$$

Where the † symbol denotes a creation operator. The creation operator acts on a wavefunction, in our case an empty wavefunction, known as a vacuum state ($|\rangle$), and "creates" a particle in orbital i. The annihilation operator eliminates an electron in orbital i from the wavefunction, returning the empty wavefunction in this case. Paired together they can be used as an excitation operator:

$$\hat{a}_i^\dagger \hat{a}_j|\Phi\rangle = |\Phi_i^a\rangle \tag{1.21}$$

Where a particle has been taken from (annihilated) orbital i and put into (created) orbital a within some reference wavefunction Φ. The resulting excited wavefunction is Φ_i^a. Combinations for these operators form the basis for the cluster operator which acts upon the Hartree–Fock wavefunction to express a Coupled Cluster wavefunction as a linear combination of the ground (Hartree–Fock) and excited wavefunctions. This involves splitting the orbitals from Hartree–Fock into low-energy "occupied" orbitals and higher energy "virtual" orbitals.

The cluster operator ($\hat{T}$) can be expressed as a sum of operators which give different numbers of excitations. The simplest operator, $\hat{T}_1$ which describes single excitations can be expressed as follows:

$$\hat{T}_1 = \sum_i \hat{t}_i = \sum_{ia} t_i^a a_a^\dagger a_i \tag{1.22}$$

Here we sum over all of the single excitations that from an occupied orbital i to a virtual orbital a which my be factored in to our wavefunction. Coupled-cluster includes higher order terms which can be generically expressed in the following way:[4]

$$\hat{T}_n = \left(\frac{1}{n!}\right)^2 \sum_{i,j,k\ldots a,b,c\ldots}^{n} t_{ijk\ldots}^{abc\ldots} a_a^\dagger a_b^\dagger a_c^\dagger \ldots a_k a_j a_i \tag{1.23}$$

The full cluster operator not only contains terms like the one above, but also contains terms which are comprised of higher powers of each of the single, double, triple, etc. operator. For example, the full cluster operator contains the following term which is the squared form the single excitation operator:

$$\frac{1}{2}\hat{T}_1^2 = \sum_{ij} \hat{t}_i \hat{t}_j = \sum_{ijab} t_i^a t_j^b a_a^\dagger a_b^\dagger a_j a_i \tag{1.24}$$

One can determine that the cluster operator can be expanded in a power series of excitation operators. This means that the cluster operator at its limit can be expressed as an exponential operator which contains all orders of excitation raised to all powers. The exact coupled-cluster wavefunction can be expressed as this

$$|\Psi_{CC}\rangle = e^{\hat{T}}|\Phi_0\rangle \tag{1.25}$$

It can be realized that acting upon this wavefunction with an energy operator such as the electronic Hamiltonian ($\hat{H}$) would yield the coupled cluster energy.

$$\hat{H}e^{\hat{T}}|\Phi_0\rangle = \hat{H}|\Psi_{CC}\rangle = E_{CC}|\Psi_{CC}\rangle \tag{1.26}$$

By acting on the left with an excited state wavefunction the expression for the coupled-cluster amplitudes. These amplitudes describe how the excited state wavefunction is coupled to the ground state wavefunction through the cluster operator.

$$\langle\Phi_{ij\ldots}^{ab\ldots}|\hat{H}e^{\hat{T}}|\Phi_0\rangle = E\langle\Phi_{ij\ldots}^{ab\ldots}|e^{\hat{T}}|\Phi_0\rangle \tag{1.27}$$

An important part of this theory involves its truncation. It is helpful now to express the one-electron Hamiltonian operator in second-quantized form:

$$\hat{H} = \sum_{pq} h_p^q a_q^\dagger a_p + \sum_{pqrs} \langle\phi_p\phi_q||\phi_r\phi_s\rangle a_p^\dagger a_q^\dagger a_s a_r \tag{1.28}$$

Where p, q, r, and s are generic indices which can refer to any orbital, whether it can be found in the

occupied or virtual orbitals. A key requirement of an energy term or amplitude term in coupled-cluster is that the Hamiltonian and the specific operator within the expansion of the cluster operator be able to "connect." This means that they must share at least one index (p, q, ...) or the term does not contribute to the overall coupled cluster equations. Since the terms in the Hamiltonian have at most four indices, the Hamiltonian can only connect to four excitation operators.[4] This means that a $\hat{T}_4^4$ term which describes a 16-tuple excitation in the wavefunction may survive while a $\hat{T}_1^5$ term which only describes a quintuple excitation will not contribute to the coupled-cluster equations.

1.3 Second-Order Vibrational Perturbation Theory

Molecular vibrations are typically treated using the harmonic approximation. In this case, the potential of the vibrational motion is assumed to be quadratic, centered at the equilibrium value of the vibrational coordinate, also called a normal coordinate. Normal coordinates are defined as the eigenvectors of the second derivative energy matrix, known as the Hessian. Assuming that the Hessian was mass-weighted, the frequencies associated with the normal coordinates are found using the eigenvalues of the matrix. Because the potential of each coordinate is assumed to be quadratic, the frequencies are merely related to the curvature (second-derivative) of the potential. This approximation is fairly good when the molecule is near 0 K, and the vibrations are near the bottom of a potential, where it is most harmonic in character. This can be seen in figure 1.1. At the equilibrium value of both curves, the two potentials are nearly identical. However, the two deviate from one another the further from equilibrium coordinate r is displaced.

Realistic molecular vibrations do not have quadratic potentials. For example, bond stretches are better modeled by a Morse potential. This potential accounts for the fact that the energy of the system rises faster as nuclei are pushed together (a bond is compressed) than when they are pulled apart (a bond is stretched). As bonds are stretched, they are weakened and the curvature decreases to the point where the bond breaks and there should be no increase in energy as the previously bonded atoms go further apart. This anharmonic behavior needs to be accounted for if computed frequencies are going to match the fundamental frequencies observed in an experimental setting.

Because computations treat molecules at 0 K, where the potential of vibrations is most harmonic, small perturbative correction to account for anharmonicity is generally enough to bring computed frequencies into decent agreement with those observed in spectroscopic experiment. Vibrational perturbation theory[5,6] utilizes higher order derivatives to address the anharmonicity of vibrations. Within second order vibrational perturbation theory (VPT2), third and fourth derivatives of the potential energy surface are computed and new vibrational frequencies can be obtained using the following equation:[5]

Figure 1.1: A diagram of a morse potential (blue) overlaid with a harmonic potenial (red). Both potentials describe the potential energy surface with respect to a generic coordinate r.

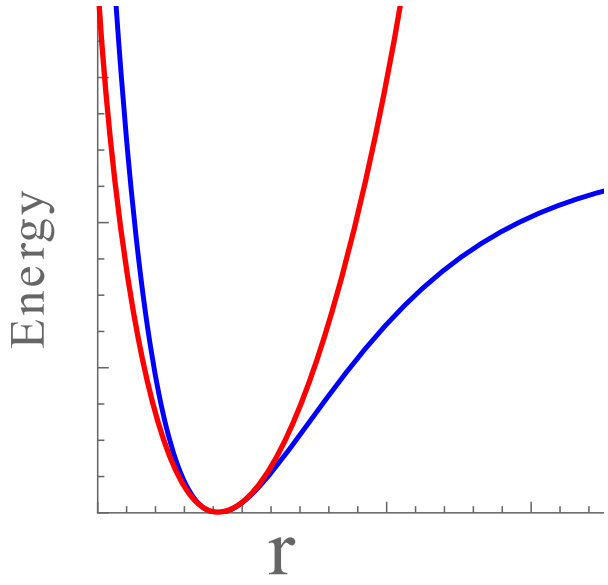

$$\nu_r = \omega_r + 2\chi_{rr} + \frac{1}{2}\sum_{r\neq s}\chi_{rs} \tag{1.29}$$

In this equation the value of ν_r and ω_r are the new anharmonic vibrational frequency and the harmonic vibrational frequency for mode r, respectively. The (χ_{rs}) are the anharmonicity constants. These constants are the product of third- and fourth-derivatives of the potential energy surface known as cubic and quartic force constants respectively, along with the harmonic frequencies and equilibrium rotational constants. The values for these anharmonicity constants have the following mathematical form within the VPT2 approximation:[5?]

$$\chi_{rr} = \frac{1}{16}\phi_{rrrr} - \frac{1}{16}\sum_{s}\phi_{rrs}^2\frac{(8\omega_r^2 - 3\omega_s^2)}{\omega_s(4\omega_r^2 - \omega_s^2)} \tag{1.30}$$

and

$$\chi_{rs} = \frac{1}{4}\phi_{rrss} - \frac{1}{4}\sum_{t}\phi_{rst}\frac{\omega_t(\omega_t^2 - \omega_r^2 - \omega_s^2)}{\Delta_{rst}} + \left[A_e(\zeta_{rs}^{(a)})^2 + B_e(\zeta_{rs}^{(b)})^2 + C_e(\zeta_{rs}^{(c)})^2\right]\left(\frac{\omega_r}{\omega_s} + \frac{\omega_s}{\omega_r}\right) \tag{1.31}$$

where ω_r is the harmonic frequency for mode r, ϕ_{rrr} and ϕ_{rrrr} are the cubic and quartic force constants, respectively. The first term represents the "diagonal" terms of the VPT2 analysis. The much more complicated equation 1.31 represents those "off diagonal" terms, which describes the coupling of two different

vibrational modes within the analysis. As such, a few terms need to be included. The last term of this equation includes the equilibrium rotational constants A_e, B_e, and C_e along with ζ terms. These terms represent the coupling of the two vibrational modes r and s through molecular rotations about each of the inertial axes. The final term from the denominator of the summation is equal to:[5]

$$\Delta_{rst} = (\omega_r + \omega_s + \omega_t)(\omega_r + \omega_s - \omega_t)(\omega_r - \omega_s + \omega_t)(\omega_r - \omega_s - \omega_t) \tag{1.32}$$

A difficulty associated with this type of analysis is the presence of "resonance" terms which exist in the summations present within both terms. A "resonance" occurs when the denominator within the summation goes to nearly zero because of an accidental degeneracy. When the denominator approaches zero, the term grows erroneously large and the frequencies obtained from the perturbative treatment of anharmonicity suffer in quality. These resonances are known as Fermi resonances. An example of how these resonances can be dealt with is found in section five of the second chapter of this dissertation.

1.4 Natural Bond Orbital Analysis

Hartree–Fock Theory obtains the wavefunction of a molecule as a product of one-electron wavefunctions that are potentially spread through the entire molecule (hence they are called molecular orbitals). Natural Bond Orbital (NBO) theory[7–9] seeks to describe the wavefunction in terms of what are called localized orbitals. These orbitals help describe a Lewis type bonding concept in a simple easy to visualize way. In an excellent review by Reed, Curtiss, and Weinhold,[9] the authors describe the process of determining NBOs as part of a series in which different types of orbitals may be obtained.

$$input \rightarrow NAOs \rightarrow NHOs \rightarrow NBOs \tag{1.33}$$

Natural orbitals, as defined in the review above, are eigenfunctions (ϕ_i) of the one-particle reduced density matrix. The elements of this matrix are the overlap of the two functions sandwiching the density operator which represents the integration over all electrons except for one in each case. Written in second-quantized form, the elements of the matrix look as such:

$$\Gamma_{ij} = \sum_{ij} \langle \chi_i | \phi_k \rangle \langle \phi_k | \chi_j \rangle \tag{1.34}$$

If this density matrix is computed with the atomic basis, it is possible to partition the density matrix Γ into atomic blocks where each block on the diagonal describes the atomic centered densities for atoms (A, B, ...)

$$\mathbf{\Gamma} = \begin{bmatrix} \Gamma_{AA} & \Gamma_{AB} \\ \Gamma_{BA} & \Gamma_{BB} \end{bmatrix} \tag{1.35}$$

The above density matrix corresponds to a two-atom system. By diagonalizing the Γ_{AA} and Γ_{BB} matrices, one can obtain eigenfunctions which correspond to the natural atomic orbitals (NAOs). The eigenvalues obtained, which are the corresponding occupancies of these NAOs, can be used to classify the orbitals as either core orbitals or lone pair orbitals if the occupation is close to two, bonding orbitals if occupancy is close to one or non-bonding orbitals if the occupancy is near zero. The procedure to the natural hybrid orbitals (NHOs)[10,11] and natural bond orbitals (NBOs) requires that the terms from the core orbitals and lone pair orbitals be zeroed out in the density matrix $\mathbf{\Gamma}$. Diagonalizing this new matrix, including the off-diagonal, inter-atomic terms, gives eigenfunctions that correspond to the NBOs, which can be partitioned into atomic centered NHOs.

$$C_i^{AB} = \begin{bmatrix} c_b^A \\ c_a^B \end{bmatrix} \tag{1.36}$$

Where C_i^{AB} describes an NBO between atoms A and B. This eigenvector is then shown to be a combination of the NHO c_b^A, an NHO on atom A pointed toward atom B, and the corresponding NHO on atom B pointed toward atom A. We can form bonding or anti-bonding NBOs by respectively adding or subtracting the NHOs from one another. This leads to bonding orbitals which have occupancies which are close to two, and anti-bonding orbitals which have occupancies close to zero.

Natural population analysis involves summing of the density in all orbitals of an atom. For any atom (A), we can define the natural population (q) as:[8]

$$q^{(A)} = \sum_i \langle \sigma_i^{(A)} | \hat{\Gamma} | \sigma_i^{(A)} \rangle \tag{1.37}$$

Where the natural population is the sum of the density of all orbitals (σ_i) centered on atom A. The value of this atomic density can tell how much charge transfer (either gaining or losing of electrons) has occurred for atom (A) within the system of chemical interest.

One of the most powerful and telling analyses that is part of NBO is the determination of non-Lewis contributions to the bonding effects. This is done using a second-order perturbative analysis of the energy:[7,8,12]

$$\Delta E^{(2)}_{i \to j^*} = -2 \frac{\langle \sigma_i | \hat{F} | \sigma_j^* \rangle^2}{\epsilon_{j^*} - \epsilon_i} \tag{1.38}$$

The numerator term on the right contains the bonding orbital (σ_i) and the antibonding orbital (σ_j^*) surrounding an energy operator, which in this case is the Fock operator ($\hat{F}$). The denominator is the difference in energy of the antibonding orbital and the bonding orbital. These terms help describe donations from occupied natural bonding orbitals to unoccupied natural antibonding orbitals. Analysis of these terms can give excellent information on delocalization effects within the electronic structure of a molecule. The program reports three values for each interaction of this type. First the ΔE, value is reported with large values indicating that a strong energetically lowering interaction occurs between two NBOs. The magnitude of this first value is decided by both the numerator and the denominator on the right side of the previous equation. The more relevant value would be a large numerator which signifies a large overlap of the two orbitals, while a small denominator may be coincidental.

1.5 Focal Point Analysis

There are three main approximations made when solving the many-electron Schrödinger equation. The first is the incompleteness of the basis set. An infinite basis set, also known as the complete basis set, would yield the lowest possible Hartree–Fock energy which is achieved by unlimited flexibility to describe the cloud of electrons. The complete basis set does not in reality have a representation as one cannot always add more basis functions to a set used to compute an energy. Instead we use basis sets of manageable size which can be realistically used in computations. As we will discuss in more detail later, by building up the size of basis sets in a systematic way, we can extrapolate what the energy would be at the complete basis set limit.

The second approximation is made regarding the correlation treatment of the wavefunction. As discussed in the section above on coupled-cluster theory, a wavefunction that accurately describes how electrons interact with one another can be achieved by expressing the wavefunction as a linear combination of the ground-state wavefunction and excited wavefunctions which result from excitations from orbitals in the ground-state wavefunction. Just basis sets are utilized to approach the complete basis set in some known way, coupled-cluster can be used to approach the FCI limit, utilizing higher orders of excitation.

The third main approximation that we make is that to ignore the relativity of the system which is valid for first and second row elements but not for larger elements. Electrons toward the core of large elements move at speeds that approach the speed of light and thus their mass changes. This has an effect upon the shapes of orbitals, particularly by contracting s and p orbitals while expanding d and f orbitals,[13] also changing the energy of the system.

Focal Point Analysis (FPA)[14–16] focuses upon the first two approximations while adding corrections accounting for relativistic effects. The results of a FPA are often expressed within a table of values that looks like the following:

Table 1.1: An example incremented focal point table.

	HF	$+\delta$ MP2	$+\delta$ CCSD	$+\delta$ CCSD(T)	$+\delta$ CCSDT	$+\delta$ CCSDT(Q)	$+\delta$ CCSDTQ	NET
aug-cc-pVDZ	+0.34	−2.30	+1.06	−0.40	+0.10	−0.05	+0.01	[−1.23]
aug-cc-pVTZ	+1.24	−2.28	+1.10	−0.38	[+0.10]	[−0.05]	[+0.01]	[−0.26]
aug-cc-pVQZ	+1.24	−2.22	+1.10	−0.38	[+0.10]	[−0.05]	[+0.01]	[−0.20]
aug-cc-pV5Z	+1.26	[−2.20]	[+1.09]	[−0.38]	[+0.10]	[−0.05]	[+0.01]	[−0.16]
CBS LIMIT	[+1.27]	[−2.17]	[+1.09]	[−0.38]	[+0.10]	[−0.05]	[+0.01]	[−0.13]

Where each value, except for Hartree–Fock values, is the difference in total energy from the previous column. Each column represents an increase in the amount of correlation treatment with the values closest to that of FCI are on the right hand side of the table, and each new row describes an increase in the cardinality of the basis set. For the purposes of this study, the correlation consistent basis sets designed by Dunning[17] are used for all FPA results. These basis sets exhibit the systematic convergence to the complete basis set limit that is integral to FPA.

All values in brackets are either the result of extrapolations to the CBS limit or the result of additivity. The later comes from the fact that at higher levels of correlation, the corrections should be very small and thus basis set should not impact the value of the energy significantly. These values are not extrapolated, but are treated as additive corrections to the electronic energy to aid in the approach of FCI. Extrapolation techniques are different between HF and correlated methods.

The HF energy extrapolations utilize the equations presented by Feller[18] which uses energies obtained using three basis sets of increasing cardinality.

$$E_X = E_\infty + Be^{-CX} \tag{1.39}$$

Here the E_∞ is the CBS limit of the energy, B and C are variables to be solved for and E_X is the HF energy obtained using each basis set. Note that we use 3 and 4 for the TZ and QZ energies respectively. Utilizing three basis sets, we have a system of three equations and three unknowns which means that we have a fully determined system. The solutions for B and C are generally not regarded, but the value for E_∞ is incredibly important. The solution for the CBS energy has the following general form:

$$E_\infty = E_{X3} - \frac{(E_{X3} - E_{X2})^2}{E_{X1} - 2E_{X2} + E_{X3}} \tag{1.40}$$

And the expression for the HF/CBS energy in Table 1.1 is:

$$E_\infty = E_{5Z} - \frac{(E_{5Z} - E_{QZ})^2}{E_{TZ} - 2E_{QZ} + E_{5Z}} \tag{1.41}$$

The correlated energies, those obtained at the MP2 level and higher, are only extrapolated using a two-point extrapolation devised by Helgaker:[19]

$$E_X = E_\infty + BX^{-3} \tag{1.42}$$

Herein, the extrapolations are often done using the TZ and QZ energies. Again, if we compute the energy using two different basis sets of cardinality X1 and X2, we have a system of two equations with two unknowns (E_∞ and B). Solving for the CBS energy, we get the following equation:

$$E_\infty = E_{X2} - \frac{E_{X2} - E_{X1}}{X_2^{-3} - X_1^{-3}} \times X_2^{-3} \tag{1.43}$$

These extrapolations typically sufficiently deal with basis set effects. One detail to consider however, is the energetic convergence observed for the energies within the extrapolation scheme. The obtained CBS energy does change based upon which energies are used for the extrapolation. It is better to extrapolate using energies that are obviously converging on the same answer. This is easily seen in a focal point table and is worth consideration when using FPA.

Corrections to account for relativistic as well as non-electronic energy values are often added to further refine the energies. For reaction energies, the energies of reactants and products have vibrational energy even at 0K. The so-called zero point vibrational energy correction is achieved by adding the values obtained from reactants and products at the geometries used to model these processes. When hydrogens are present

in a system, it may be that a slight breakdown of the Born–Oppenheimer approximation may affect results. A third correction that is often added is a computation accounting for the fact that often core electrons are not treated with correlation. There are also several ways to account for relativistic effects. All additive corrections result from single point calculations done at identical levels of correlation treatment with basis sets of identical cardinality.

A nice feature of focal point analysis is that it allows for error bars to be put on the computed energy for a system. The correction at the highest level of correlation can serve as the precision for the calculation. Often this results that are converged to within chemical accuracy, 1 kcal mol^{-1}, for the energy a system being studied at a given level of theory and basis set.

CHAPTER 2

INVESTIGATING THE GROUND-STATE ROTAMERS OF THE *N*-PROPYLPEROXY RADICAL*

* Reprinted from Hoobler, P. R.; Turney, J. M.; and Schaefer, H. F., *J. Chem. Phys.* 2016, 145 174301, with the permission of AIP Publishing.

2.1 Abstract

The *n*-propylperoxy radical has been described as a molecule of critical importance to studies of low temperature combustion. *Ab initio* methods were used to study this three-carbon alkylperoxy radical, normal propylperoxy. Reliable CCSD(T)/ANO0 geometries were predicted for the molecule's five rotamers. For each rotamer, energetic predictions were made using basis sets as large as the cc-pV5Z in conjunction with coupled cluster levels of theory up to CCSDT(Q). Along with the extrapolations, corrections for relativistic effects, zero-point vibrational energies, and diagonal Born–Oppenheimer corrections were used to further refine energies. The results indicate that the lowest conformer is the *gauche-gauche* (GG) rotamer followed by the *gauche-trans* (0.12 kcal mol^{-1} above GG), *trans-gauche* (0.44 kcal mol^{-1}), *gauche′-gauche* (0.47 kcal mol^{-1}), and *trans-trans* (0.57 kcal mol^{-1}). Fundamental vibrational frequencies were obtained using second-order vibrational perturbation theory (VPT2). This is the first time anharmonic frequencies have been computed for this system. The most intense IR features include all but one of the C-H stretches. The O-O fundamental (1063 cm^{-1} for the GG structure) also has a significant IR intensity, 19.6 km mol^{-1}. The anharmonicity effects on the potential energy surface were also used to compute vibrationally averaged $r_{g,0K}$ bond lengths, accounting for zero-point vibrations present within the molecule.

2.2 Introduction

Low-temperature combustion occurs between 600–900 K,[20,21] and is comprised of cool flame oscillations involving free radical pathways. In this temperature regime, the barrierless, exothermic reaction between alkyl radicals and molecular oxygen[22] strongly influences combustion dynamics. At this point, several subsequent reactions can proceed through energetically submerged transition states with respect to the initial reactants. The fate of alkylperoxy radicals is dependent on temperature, pressure, and the alkyl chain length (C_nH_{2n+1}) among other factors. This diverse chemistry was reviewed by Zádor, Taatjes and Fernandes in 2011.[23] For species with $n \leq 2$ the reaction products are dominated by the concerted elimination of hydroperoxy radical ($HOO^{\bullet}$) and formation of hydroxyl radicals ($^{\bullet}OH$), the species believed to be the key to low-temperature combustion. Note that at elevated temperatures, the kinetic rate for the reverse reaction ($ROO^{\bullet} \rightarrow R^{\bullet} + O_2$) becomes non-negligible due to its barrierless nature. This leads to what is call the "Negative Temperature Coefficient" (NTC) region where increasing temperatures counterintuitively lead to a delay in combustion.[24–27]

In this work, we consider the *n*-propylperoxy radical (3 carbon atoms).[27–31] This molecule is often considered to be an ideal combustion compound for theoretical examination because of its manageable size coupled with a combustion mechanism containing intermediates of interest. The most crucial propylperoxy

intermediate[25,32,33] is formed by way of an internal hydrogen abstraction. This process occurs through a ring-like transition state, resulting in a carbon centered radical, often denoted as QOOH. Until recently,[34] no QOOH species had been directly characterized, though the existence of these combustion intermediates has been included in most kinetic models.[35] The difficulty in achieving this feat is due to the highly-transient nature of these intermediates. A 5- and a 6-membered ring transition state are available to *n*-propylperoxy radical for the formation of QOOH. The barriers corresponding to both ringed species lie lower in energy than reactants. While it is true that the six-membered ring transition state lies lower in energy than the 5-membered ring,[29,32,36] both are considered integral to the kinetic model of n-propylperoxy combustion. The QOOH species can undergo a second addition of molecular oxygen to form a peroxyalkylhydroperoxy radical ($^{\bullet}$OOQOOH). The kinetics of the formation and decomposition of this combustion species has become of interest recently.[37] The decomposition of $^{\bullet}$OOQOOH intermediate is believed to result in an increase in the number of radicals present in a combustion system. It is the increase in total number of radicals, in particular hydroxyl radicals, that leads to propagation and sustained low-temperature ignition. Since the *n*-propylperoxy radical system is the smallest system that can achieve the transition state of interest in route to the QOOH intermediate, it provides a unique opportunity for investigation using high-level theory. The knowledge gained by studying this relatively simple system can then be applied to much larger systems which are more prevalent within actual combustion models.

It is possible that under the right conditions, the *n*-propylperoxy radical species can relax into a deep potential well that is roughly 30 kcal mol^{-1} below that of the reactants in lieu of continuing through the available combustion pathways. The focus of this paper is to investigate what happens to the radical species once it can be found in this well.

The *n*-propylperoxy radical contains three degrees of freedom with regard to dihedral angles, two of which are considered to be of greater importance the third less so. The dihedral that is often of least interest involves the rotation of the terminal methyl group of the molecule. The other two dihedrals are the ∠OOCC and the ∠OCCC. If one of these angles has a value of 180°, it is described as *trans*, whereas if the value of the dihedral is roughly ±60°, it is described as *gauche*. There are five rotamers, isomers due to rotation, that can be formed through combinations of these two dihedrals angles. The common naming system for these rotamers is to describe the ∠OOCC first and the ∠OCCC second. The only rotamer of the five with any symmetry is the *trans-trans* (TT) rotamer which has C_s symmetry. There also exist *trans-gauche* (TG) and *gauche-trans* (GT), which are both C_1 structures. The last two rotamers both contain two *gauche* dihedral angles, made distinct by the fact that the *gauche-gauche* (GG) rotamer contains dihedrals of the same sign while the *gauche*′*-gauche* (G′G) structure has dihedrals of opposite sign.

As the n-propylperoxy radical has gained scientific attention, it has been the interest of several different theoretical studies. A 2005 study by Merle et al. considered the rotamers on the ground state potential energy surface and found their relative energies to lie within one kcal mol^{-1} at the CBS-QB3 level of theory. They also reported a population analysis using a Boltzmann distribution at 298K. What Hadad and coworkers found at three different levels of theory was that all five of these ground state rotamers made up a significant portion of the population at 298K. This suggests that, if observed, a sample of this radical species would likely contain a mixture of all five of the rotamers being studied.[36]

The 2005 study of Tarczay, Zalyubovsky and Miller[38] also included a theoretical investigation of the five rotamers. They also found the rotamers to lie very close in energy. At their "best" level of theory (G2) they found the energies of the conformers to be within 180 cm^{-1} of each other. Along with this analysis they also used the equation of motion coupled-cluster with single and double excitations (EOM-CCSD) method to compute the $\tilde{A}\leftarrow\tilde{X}$ excitation energy for each rotamer. The theoretical results were compared to experimentally obtained spectra from the same group.[39] The spectra used for experimental comparison were obtained using cavity ringdown spectroscopy (CRDS) which allows for the observation of these non-intense transitions. Matching their theoretical results with experimental results, they were able to reasonably label the excitation peaks from the CRDS spectrum with three of the five rotamers. A last piece of interesting analysis was done to determine barriers of rotation between each of the rotamers. With the B3LYP/6-31+G* method, the two different dihedral angles were scanned (0°to 180°for ∠OOCC and 0°to 360°for ∠CCCO). The results showed that the maximum barrier heights between any of the rotamers was approximately 1000 cm^{-1} ($\sim$ 2.86 kcal mol^{-1}). As they state in the paper, this relatively low barrier supports the notion that each of these rotamers would exist in equilibrium with one another at 298 K.[38] One would also expect this to be true at combustion temperatures.

Some of the first spectroscopy done on peroxy radicals was done with UV absorption spectroscopy. The n-propylperoxy radical was studied with this method.[40] However, this method does not allow for the mass specific study of peroxy radicals. The UV absorption studied corresponds to the $\tilde{B}\leftarrow\tilde{X}$ transition which is a dissociative absorption. This absorption is not strongly dependent upon the non-peroxy moiety. Thus it is an effective way to determine the presence, but not identity of peroxy radicals. The advent of cavity ring-down spectroscopy (CRDS) has greatly aided the study of peroxy radicals by increasing the sensitivity of measurements within the IR region. This method has been successfully applied to n-propylperoxy radical in order to study the $\tilde{A}\leftarrow\tilde{X}$ transition.[39,41]

To date, experimental spectra have not been reported that allow the resolution of fundamental vibrational transitions for this system. In light of this, we have predicted harmonic vibrational frequencies for the n-propylperoxy radical along with anharmonic corrections using VPT2 theory. The fundamental frequencies

reported in this paper should aid in the assignment of experimentally obtained vibrational spectra. This interplay of theory and experiment is well precedented within the field of peroxy radicals and related combustion species.[42–45] We seek to provide spectroscopic information in line with this precedent for n-propylperoxy radical. Our analysis should aid in the spectral identification of this molecule from experimental studies. Further, an attempt to differentiate the rotamers and provide a method of specific rotamer detection may allow for the determination of the conformational make-up of this species within combustion systems. This would provide insight into the effect of rotamer populations on low-temperature combustion phenomena.

The reference geometry of each rotamer was optimized by using coupled-cluster theory, incorporating single, double, and perturbative triple excitations [CCSD(T)] with the Atomic Natural Orbital (ANO) basis set proposed by Almöf and Taylor.[46] All geometry optimizations were completed with an unrestricted Hartree–Fock (UHF) reference along with a frozen core (1s-like molecular orbitals of carbon and oxygen) approximation.[47] The ANO family of basis sets was chosen because it appears to perform well within VPT2 theory when compared to similarly sized basis sets.[48] Given the relatively large system being studied, the ANO0 basis set (comparative in size to the Dunning cc-pVDZ basis set) made computations of anharmonic frequencies feasible. Initial harmonic frequencies were checked to make sure that no imaginary frequencies existed, ensuring that we had optimized to a true minimum on the potential energy surface in the case of each rotamer.

Anharmonic corrections to the potential energy surface for each rotamer were accounted for using second-order vibrational perturbation theory (VPT2) at the UHF-CCSD(T)/ANO0 level of theory. The full cubic force field was obtained along with the semi-diagonal portion of the quartic force field. These were obtained by numerical differentiation of analytic second derivatives. The CFOUR program was utilized for all computations.[49]

In the case of resonances between a vibration and a single overtone, resonances were dealt with by building 2×2 matrices with anharmonic frequencies on the diagonal with cubic force-constants making up the off-diagonal elements. By diagonalizing these matrices, corrections to the computed anharmonic frequencies were obtained. In the case of both the GG and G′G rotamers, a single fundamental frequency was found to be in resonance with two different overtones. This required the building of a 3×3 matrix with cubic force constants between the fundamental frequency with each of the overtones and Darling–Dennison coefficients representing the interactions between the overtones. The process of identifying and these resonances was done using the PyVPT2 program.[50]

Accurate relative energies for the rotamers were determined using the focal point analysis technique,[14,15,51] making use of the reference geometries at the UHF-CCSD(T)/ANO0 level of theory. Extrapolation to the complete basis set limit was done for both Hartree–Fock (HF) energies (three point extrapolation) and cor-

relation energies (two point extrapolation) obtained using the Dunning correlation consistent cc-pVXZ (X = T, Q, 5) basis sets[52] via the following extrapolation functions:[18,19]

$$E_{\mathrm{HF}}(X) = E_{\mathrm{HF}}^{\infty} + ae^{-bX} \tag{2.1}$$

and

$$E_{\mathrm{corr}}(X) = E_{\mathrm{corr}}^{\infty} + aX^{-3} \tag{2.2}$$

Included in the analyses were high level correlation computations through coupled cluster theory including single, double, triple and perturbative quadruple excitations [CCSDT(Q)]. These CCSDT(Q) computations were done using the MRCC code of Kállay interfaced with CFOUR.[53,54] In order to correct for the frozen-core approximation that was used during the single point energy computations, an auxiliary core correlation correction(Δ_{core}) was computed. This correction represents the difference between all electron (AE) and frozen core (FC) single point energies that were computed using the Dunning correlation consistent triple-zeta basis set including core functions (cc-pCVTZ).

$$\Delta_{\mathrm{core}} = [\text{AE-CCSD(T)/cc-pCVTZ}] - [\text{FC-CCSD(T)/cc-pCVTZ}] \tag{2.3}$$

Also included in the corrections were anharmonic zero point vibrational energy corrections (Δ_{AZPVE}). In each case, this correction was obtained during the computations to determine the anharmonicity of the potential energy surface. Due to the fact that our system contains a relatively large number of hydrogens, we had to consider the possibility of non-adiabatic effects. In order to assure that we have a high level of reliability with regard to such effects, diagonal Born-Oppenheimer corrections (Δ_{DBOC}) were predicted at the HF/cc-pVTZ level of theory.[55,56] Final corrections were added to our results to account for relativistic effects (Δ_{rel}). These relativistic corrections were obtained by adding the mass-velocity and Darwin one-electron terms computed with the AE-CCSD(T)/cc-pVTZ method.[57,58]

As one last piece of analysis, the vibrationally averaged equilibrium parameters ($r_{g,0K}$) were computed and compared to the equilibrium internuclear distances (r_e). These results are reported in Table 2.7. Following the example of Copan, Schaefer, and Agarwal[43], the vibrationally averaged bond lengths are obtained through the following Taylor expansion of the bond lengths in terms of normal modes of vibration:

$$r_{g,0K} = \langle r \rangle_{g,0K} \approx r_e + \sum_s (\frac{\partial r}{\partial Q_s})_e \langle Q_s \rangle_{g,0K} + \frac{1}{2} \sum (\frac{\partial^2 r}{\partial Q_s^2})_e \langle Q_s^2 \rangle_{g,0K} \tag{2.4}$$

2.3 Results

2.3.1 Fundamental Vibrational Frequencies

We present our anharmonic vibrational frequencies for all five rotamers in Table 2.1. Each column contains the set of harmonic frequencies, anharmonic corrections, and final anharmonic fundamental frequencies for a particular structure. It is worth noting that we do not follow the standard convention in our designation of the frequencies for the symmetric TT rotamer. Given that the rotamer has C_s symmetry, convention would require us to report all a′ fundamentals followed by all a″ modes. For ease of comparison with our C_1 rotamers, which have no point group symmetry, we have more appropriately reported the fundamentals in decreasing order of frequency. Our harmonic frequencies show general agreement with previous research done on this system.[36] The anharmonic corrections to these frequencies may be understood in terms of the primary bonds involved in each vibrational mode. Those vibrational frequencies which correspond to C–H bond stretches (modes 1–7) exhibit large anharmonic corrections, generally above 100 cm^{-1} in magnitude. All other modes have anharmonic corrections that are below 50 cm^{-1} in magnitude. Any resonances that were found between fundamentals and overtones were corrected for using the PyVPT2 program described in the theoretical methods section of this paper.[50] Those frequencies which were subject to resonance are labeled within the tables, along with which overtone band(s) provide the resonance interaction.

Comparing vibrational frequencies between different rotamers is complicated by the lack of symmetry present in four of the five species studied. In Table 2.2 we have labeled some of the more recognizable frequencies. The easiest assignment to be made is that for the O-O stretch. For each rotamer, this is reported as ν_{19}. The frequencies we report for this mode are 1063 cm^{-1} for the GG rotamer, 1060 cm^{-1} for the GT, 1073 cm^{-1} for the TG, 1064 cm^{-1} for the G′G, and 1072 cm^{-1} for the TT. These frequencies span a range of only 13 cm^{-1}. This comparison indicates that this mode is not largely dependent upon the alkyl portion of the molecule. As may be seen in Table 2.2, these modes are among the most intensely IR active modes for each of the five rotamers. This fundamental should appear in any IR spectrum of the molecule. Unfortunately, except at very high resolution, this mode would not be a good candidate for differentiating

the rotamers, due the fact that there is no large variation in this fundamental across the five rotamers.

The C-O stretching modes are similar to the O-O stretching modes in that the range of frequencies over which these modes occur is modest but moreso than found for the O-O stretch. The fundamental band which primarily contains the C-O stretch is ν_{21}. From Table 2.1, the reported fundamentals for this mode range from 908–953 cm^{-1}. The intensities associated with this mode fall in one of two camps, where the intensities reported for the TG, TT, and G′G rotamers are approximately twice the intensities reported for the GT and GG rotamers. With all of this in mind, it may be possible to specifically detect the TT rotamer [ν(CC) = 953 cm^{-1}] which has a favorable combination of high IR intensity and distinct frequency. For the other rotamers, any unresolved spectrum might not be helpful for rotamer specific detection.

The two C-C bond stretching modes offer the best hope for rotamer specification. The modes involving these two stretches are ν_{13} for the C_α-C_β stretch and ν_{12} for the C_β-C_γ stretch. Combining the analysis of these two modes is much more useful in this case than looking at them individually. The most distinct of the rotamers is likely the higher energy (by only 0.5 kcal mol^{-1}) G′G rotamer. From Table 2.2, it can be seen that only ν_{13} is predicted to appear as a fairly strong peak within an IR spectrum, while for the other C-C stretching mode ν_{12}, the IR intensity is small (0.7 km mol^{-1}). The TG rotamer essentially shares the same frequencies for both modes with differences of 3 cm^{-1} and 5 cm^{-1} for ν_{12} and ν_{13} respectively. The differentiating factor between the G′G and TG rotamers comes with their relative frequencies. By comparison with the strong O-O stretch (intensities 19–28 km mol^{-1}), the ν_{13} C_α-C_β intensity for the G′G rotamer is about half as intense, while the ν_{13} intensity for the TG rotamer is only about one fifth as intense. In this way, these two rotamers may be differentiated from one another and are distinct enough from the other rotamers that a well resolved experimental spectrum might be able to distinguish either the G′G or the TG from the other rotamers. The TT rotamer is the next most easily identifiable rotamer. From Table 2.2, the frequencies for the two C-C modes are essentially identical, differing by 2 cm^{-1}, and should appear as one, fairly intense peak, particularly in matrix isolation. The last two rotamers, the GT and GG, present a challenge for this combined analysis. Neither of these two rotamers is predicted to have an intense band for either of these modes. Further, the frequencies for the modes of interest only differ by 5 cm^{-1} and 10 cm^{-1}. This combined analysis, even appended with information from more modes, will have a difficult time differentiating these two rotamers from one another. Our global analysis of the C-C stretching modes however, does get us closer to rotamer specific detection.

The lowest frequency torsion modes within each of the conformers have also been assigned. In four of our five rotamers, we find that the lowest frequency mode largely involves the torsion about the ∠OOCC dihedral angle. The exception is the GT conformer where this torsion is assigned to ν_2. The fundamental frequencies for this mode lie between 69 and 113 cm^{-1}, most of which fall in the lower end of this range. Considering

the ∠OCCC dihedral, we find that the torsional motion involving this dihedral can be assigned to ν_2, again the exception being the GT rotamer. The frequencies for this motion lie between 98 and 145 cm^{-1}. The last dihedral degree of freedom involving the terminal methyl group can generally be assigned to ν_3 with the exception of the TT rotamer where ν_4 is assigned to this mode. The frequencies assigned to terminal methyl rotation range from 173 to 227 cm^{-1}. It is interesting to note that the theoretical frequencies span a range of 54 cm^{-1}. A slight dependence upon the OOCC dihedral angle can be observed. Rotamers with a *gauche* dihedral angle at this position have higher frequencies corresponding to terminal methyl rotation, while those rotamers with a *trans* dihedral at this position have lower frequencies.

Given the slight dependence upon the OOCC dihedral angle on the torsional modes a future avenue of study presents itself. A coupled rotor analysis of the torsional modes can be performed to project out their effect on the remaining vibrational modes. Tarczay and co-workers[38] predicted rotational barriers of roughly 250–1000 cm^{-1} associated with transformations between rotamers of the *n*-propylperoxy radical, and we find the barrier for terminal methyl rotation to be roughly 900 cm^{-1} using B3LYP and a triple-ζ quality basis set. Given that the rotational barriers within the *n*-propylperoxy radical are of this magnitude, we are confident that VPT2 can offer a valid treatment of these modes.

As noted in Table 2.1, each rotamer shows a resonance between one of the C-H stretching fundamentals and at least one overtone band. All of the resonances observed are between fundamental C-H stretching modes and first overtones of ∠HCH bends. For both the GG and G′G rotamers, a single C-H stretching fundamental (ν_7 for GG and ν_6 for G′G) is in resonance with two separate ∠HCH bending overtones (ν_8 and ν_9). All of the modes associated with these frequencies involve the terminal methyl group. These resonances require the building of 3×3 contact matrices in order to be resolved. The corrections for these resonances were +36 cm^{-1} in each case. For the TG rotamer, there is found a fundamental which suffers from resonance with a single overtone. This resonance also occurs between the fundamental involving the terminal C-H stretch (ν_7) and a terminal methyl ∠HCH bend (ν_8). The applied correction was 14 cm^{-1}, much smaller than that for the GG and G′G resonances. This is likely due to the fact that the resonance only involves a single overtone instead of two.

The remaining pair of rotamers, GT and TT, suffer from two separate resonances between a single C-H stretch and a single ∠HCH bend. The first of these resonances occurs between the ν_6 stretch and the ν_8 bend for each rotamer. Both of these modes involve the $C_\beta H_2$ group of the molecule. This resonance is in contrast to the GG and G′G rotamers which only display resonances involving the terminal methyl moiety. The second pair of resonances do involve the terminal methyl group. These occur between the ν_6 stretching and the ν_8 bending modes. The corrections applied to account for both of these resonances were roughly the same as that for the TG. This is likely due to the fact that each interaction accounted for was

between a single fundamental and a single overtone. All of the resonances discussed within this section have been noted in Table 2.1 along with identification of which fundamentals and overtones participate in each resonance. Specific values for the applied corrections along with cubic force constants associated with resonances have been included in the Supplemental Information for this paper. A potential dependence upon the ∠OCCC dihedral angle might be inferred from these observations. Further study would be required to draw conclusions based upon the ∠OCCC dihedral angle (or terminal ∠CCCC dihedral angle in any larger alkylperoxy molecule) and its effect upon the types of resonances that plague a particular alkylperoxy IR spectrum.

Table 2.1: Harmonic (ω), anharmonic corrections ($\delta\nu$), and final fundamental frequencies (ν) for the *gauche-trans* (GT), *trans-gauche* (TG), *trans-trans* (TT), *gauche-gauche* (GG), and *gauche′-gauche* (G′G) rotamers for the *n*-propylperoxy radical obtained using the ANO0/CCSD(T) level of theory (cm^{-1}). See Figure 2.1 for the structural differences between the five rotamers.

	GT			TG			TT			GG			G′G		
Mode	ω	$\delta\nu$	ν	ω	$\delta\nu$	ν	ω	$\delta\nu$	ν	ω	$\delta\nu$	ν	ω	$\delta\nu$	ν
1	3148	−152	2996	3146	−148	2999	3143	−154	2989	3148	−152	2996	3152	−152	3001
2	3139	−148	2991	3142	−155	2987	3140	−148	2992	3144	−147	2997	3148	−151	2997
3	3128	−148	2980	3132	−147	2985	3128	−149	2979	3132	−148	2985	3135	−148	2986
4	3110	−147	2963	3102	−147	2955	3105	−147	2958	3108	−147	2961	3096	−146	2949
5	3076	−122	2954	3075	−113	2962	3073	−108	2965	3077	−124	2954	3079	−126	2953
6	3062	-104^{1}	2958	3054	−113	2941	3060	-98^{2}	2962	3055	−117	2938	3052	-88^{3}	2967
7	3045	-78^{4}	2967	3049	-90^{5}	2959	3046	-77^{6}	2969	3048	-84^{7}	2964	3045	−114	2931
8	1517	−44	1473	1515	−32	1483	1520	−43	1477	1514	−43	1471	1512	−41	1471
9	1509	−42	1467	1512	−53	1459	1510	−41	1468	1508	−45	1463	1507	−41	1466
10	1502	−47	1454	1501	−44	1457	1509	−41	1469	1486	−42	1444	1483	−39	1443
11	1487	−42	1445	1484	−45	1439	1500	−49	1451	1484	−40	1444	1478	−38	1441
12	1420	−36	1384	1423	−34	1389	1421	−34	1387	1423	−34	1389	1426	−34	1392
13	1409	−38	1371	1404	−42	1362	1415	−26	1389	1396	−35	1361	1395	−38	1357
14	1327	−30	1296	1372	−33	1340	1328	−29	1299	1374	−34	1340	1377	−34	1343
15	1322	−29	1293	1308	46	1354	1320	−32	1289	1302	−31	1271	1301	−22	1279
16	1281	−34	1248	1253	−32	1221	1261	−33	1228	1281	−31	1249	1282	−32	1250
17	1200	−29	1171	1168	−29	1139	1171	−30	1141	1187	−30	1156	1183	−27	1156
18	1133	−27	1106	1133	−27	1106	1157	−27	1130	1115	−28	1087	1115	−28	1087
19	1094	−35	1060	1104	−31	1073	1101	−29	1072	1096	−33	1063	1098	−34	1064
20	1056	−27	1028	1079	−25	1053	1064	−29	1035	1051	−16	1035	1061	−19	1042
21	961	−26	935	939	−24	915	980	−27	953	947	−18	930	932	−25	908
22	897	−12	885	913	−14	899	921	−15	906	895	−21	874	919	−14	905
23	876	−15	861	892	−16	876	891	−10	881	863	−15	848	844	−18	826
24	761	−5	757	752	−9	744	761	−5	756	757	−10	747	769	−9	760
25	557	−7	550	517	−5	513	488	−5	483	543	−5	538	525	17	542
26	373	−8	365	379	1	380	400	−5	394	431	−4	427	426	−5	421
27	262	0	261	301	−5	295	243	−12	231	290	−7	283	308	−4	304
28	241	−14	227	204	−15	189	198	−25	173	226	−8	218	236	−10	226
29	122	−9	113	134	−2	132	123	−3	120	153	−8	145	121	−6	115
30	102	−4	98	76	−6	69	82	−7	75	81	−4	77	97	−13	83

2.3.2 Energetics

The focal point results provide definitive results concerning the relative energies of the different rotamers. The GG conformer lies lowest in energy. For each of the conformers, we have computed correlation corrections

Table 2.2: Fundamental frequncies (cm^{-1}) paired with the corresponding harmonic infrared intensities (km mol^{-1}) for each rotamer of the *n*-propylperoxy radical.

		GT		TG		TT		GG		G′G	
Stretch	Mode	ν	Int.	ν	Int.	ν	Int.	ν	Int.	ν	Int.
C–H	1	2996	16.4	2999	28.3	2989	19.3	2996	16.1	3001	43.3
C–H	2	2991	18.1	2987	20.5	2992	26.3	2997	14.5	2997	21.0
C–H	3	2980	26.8	2985	15.5	2979	22.9	2985	23.4	2986	10.0
C–H	4	2963	4.2	2955	0.5	2958	9.7	2961	13.6	2949	0.3
C–H	5	2954	22.6	2962	28.1	2965	13.7	2954	22.7	2953	20.2
C–H	6	2958	12.9	2941	9.0	2962	10.7	2938	14.4	2923	11.4
C–H	7	2967	23.0	2959	20.8	2969	23.4	2921	20.8	2931	20.3
	8	1473	5.1	1483	6.0	1477	3.3	1471	6.1	1471	8.0
	9	1467	5.6	1459	6.5	1468	8.8	1463	5.6	1466	6.4
	10	1454	1.0	1457	0.6	1469	4.6	1444	0.4	1443	0.2
	11	1445	3.8	1439	0.8	1451	2.7	1444	4.1	1441	1.1
C_β–C_γ	12	1384	4.7	1389	0.8	1387	4.1	1389	3.2	1392	0.7
C_α–C_β	13	1371	3.2	1362	4.9	1389	9.0	1361	2.9	1357	13.1
	14	1296	6.5	1340	0.8	1299	11.1	1340	6.5	1343	9.0
	15	1293	0.8	1354	4.0	1289	0.9	1271	1.7	1279	0.0
	16	1248	3.7	1221	1.8	1228	1.3	1249	4.5	1250	0.3
	17	1171	2.9	1139	2.6	1141	2.3	1156	1.3	1156	1.1
	18	1106	4.1	1106	0.6	1130	3.6	1087	5.1	1087	0.6
O–O	19	1060	19.3	1073	23.4	1072	27.6	1063	19.6	1064	28.4
	20	1028	1.7	1053	0.7	1035	3.3	1035	1.8	1042	4.0
	21	935	9.7	915	16.0	953	15.3	930	8.5	908	16.7
	22	885	7.5	899	2.4	906	4.6	874	6.4	905	4.3
	23	861	6.7	876	7.0	881	0.7	848	6.4	826	1.2
	24	757	0.8	744	1.9	756	0.6	747	1.1	760	1.7
	25	550	2.9	513	2.6	483	6.2	538	3.1	542	6.5
	26	365	3.4	380	3.7	394	1.3	427	3.4	421	2.1
	27	261	1.3	295	3.2	231	0.5	283	0.4	304	0.0
	28	227	1.3	189	0.0	173	0.9	218	1.3	226	1.9
	29	113	0.6	132	1.3	120	1.7	145	1.5	115	2.6
	30	98	0.8	69	1.1	75	0.2	77	0.1	83	0.8

through CCSDT(Q). In every case, our results show good convergence at this level of correlation with the largest difference between CCSDT/cc-pVDZ and CCSDT(Q)/cc-pVDZ being 0.02 kcal mol^{-1}. None of the relative corrections for core-correlation, zero-point vibrational energy or relativistic effects is larger than 0.01 kcal mol^{-1}, and most often these should be considered to be nearly nil, given the numerical precision associated with these results.

Considering the other computed energetic corrections evaluated here, it may be seen that the system is fairly well behaved. Neither the core-correlation nor the DBOC corrections significantly adjust our predictions at the precision of 0.01 kcal mol^{-1}. The largest correction predicted was the AZPVE correction obtained from the anharmonic corrections to the potential energy surface. The AZPVE correction for the lowest energy conformer (GG) is 62.19 kcal mol^{-1} ($\sim$21750 cm^{-1}) the AZPVE values reported in the focal

point tables are relative to this. AZPVE serves to further distance our higher energy rotamers from the GG rotamer by 0.07 kcal mol^{-1} in the case of the TG rotamer and 0.08 kcal mol^{-1} in the case of the TT rotamer. The corrections themselves can be found in the reported focal point analysis tables (Tables 2.3–2.6).

Table 2.3: Focal point comparison of the energy difference between the *gauche-trans* (GT) rotamer and lowest energy *gauche-gauche* (GG) rotamer (kcal mol^{-1}).

Basis Set	ΔE_e[UHF]	δ[MP2]	δ[SD]	δ[SD(T)]	δ[SDT]	δ[SDT(Q)]	ΔE_e[SDT(Q)]
cc-pVDZ	+0.07	+0.36	−0.09	+0.03	−0.00	+0.00	[+0.36]
cc-pVTZ	−0.17	+0.42	−0.11	+0.05	[−0.00]	[+0.00]	[+0.19]
cc-pVQZ	−0.24	+0.42	−0.10	+0.05	[−0.00]	[+0.00]	[+0.13]
cc-pV5Z	−0.26	[+0.42]	[−0.10]	[+0.05]	[−0.00]	[+0.00]	[+0.12]
CBS	[−0.26]	[+0.42]	[−0.09]	[+0.05]	[−0.00]	[+0.00]	[+0.12]
ΔE_e (final) = ΔE_e[CBS CCSDT(Q)] + $\Delta E_{\mathrm{AZPVE}}$[CCSD(T)/ANO0] + Δ_{core}[CCSD(T)/cc-pCVTZ] + Δ_{rel}[CCSD(T)/cc-pCVTZ] + Δ_{DBOC}[HF/aug-cc-pVTZ] = 0.12 − 0.00_2 + 0.00_{01} + 0.00_3 + 0.00_1 = **0.12** kcal mol^{-1}							

Table 2.4: Focal point comparison of the energy difference between the *trans-gauche* (TG) rotamer and lowest energy *gauche-gauche* (GG) rotamer (kcal mol^{-1}).

Basis Set	ΔE_e[UHF]	δ[MP2]	δ[SD]	δ[SD(T)]	δ[SDT]	δ[SDT(Q)]	ΔE_e[SDT(Q)]
cc-pVDZ	+0.01	+0.63	+0.00	+0.14	+0.00	+0.02	[+0.80]
cc-pVTZ	−0.25	+0.59	+0.01	+0.16	[+0.00]	[+0.02]	[+0.53]
cc-pVQZ	−0.34	+0.58	+0.01	+0.16	[+0.00]	[+0.02]	[+0.42]
cc-pV5Z	−0.37	[+0.58]	[+0.01]	[+0.16]	[+0.00]	[+0.02]	[+0.40]
CBS	[−0.37]	[+0.58]	[+0.00]	[+0.16]	[+0.00]	[+0.02]	[+0.38]
ΔE_e (final) = ΔE_e[CBS CCSDT(Q)] + $\Delta E_{\mathrm{AZPVE}}$[CCSD(T)/ANO0] + Δ_{core}[CCSD(T)/cc-pCVTZ] + Δ_{rel}[CCSD(T)/cc-pCVTZ] + Δ_{DBOC}[HF/aug-cc-pVTZ] = 0.38 + 0.07 − $0.00_5{}^8$ + 0.00_1 + 0.00_2 = **0.44** kcal mol^{-1}							

Table 2.5: Focal point comparison of the energy difference between the *gauche′-gauche* (G′G) rotamer and lowest energy *gauche-gauche* (GG) rotamer (kcal mol^{-1})

Basis Set	ΔE_e[UHF]	δ[MP2]	δ[SD]	δ[SD(T)]	δ[SDT]	δ[SDT(Q)]	ΔE_e[SDT(Q)]
cc-pVDZ	+0.92	−0.28	+0.08	−0.06	+0.00	−0.01	[+0.65]
cc-pVTZ	+0.84	−0.30	+0.08	−0.06	[+0.00]	[−0.01]	[+0.55]
cc-pVQZ	+0.81	−0.33	+0.09	−0.07	[+0.00]	[−0.01]	[+0.50]
cc-pV5Z	+0.80	[−0.34]	[+0.10]	[−0.07]	[+0.00]	[−0.01]	[+0.48]
CBS	[+0.80]	[−0.35]	[+0.10]	[−0.08]	[+0.00]	[−0.01]	[+0.47]
ΔE_e (final) = ΔE_e[CBS CCSDT(Q)] + $\Delta E_{\mathrm{AZPVE}}$[CCSD(T)/ANO0] + Δ_{core}[CCSD(T)/cc-pCVTZ] + Δ_{rel}[CCSD(T)/cc-pCVTZ] + Δ_{DBOC}[HF/aug-cc-pVTZ] = 0.47 + 0.02 + 0.00_1 + 0.00_4 + 0.00_{02} = **0.49** kcal mol^{-1}							

2.3.3 Structures

The equilbrium geometries reported were all obtained at the ANO0/CCSD(T) level of theory. A strict convergence criterium (RMS force gradient $\leq 10^{-6}$) was required to ensure that the geometries obtained

Table 2.6: Focal point comparison of the energy difference between the *trans-trans* (TT) rotamer and lowest energy *gauche-gauche* (GG) rotamer (kcal mol^{-1})

Basis Set	ΔE_e[UHF]	δ[MP2]	δ[SD]	δ[SD(T)]	δ[SDT]	δ[SDT(Q)]	ΔE_e[SDT(Q)]
cc−pVDZ	+0.12	+0.99	−0.11	+0.16	−0.00	+0.02	[+1.18]
cc−pVTZ	−0.41	+0.96	−0.10	+0.20	[−0.00]	[+0.02]	[+0.66]
cc−pVQZ	−0.55	+0.96	−0.10	+0.20	[−0.00]	[+0.02]	[+0.52]
cc−pV5Z	−0.58	[+0.96]	[−0.10]	[+0.20]	[−0.00]	[+0.02]	[+0.49]
CBS	[−0.59]	[+0.96]	[−0.10]	[+0.20]	[−0.00]	[+0.02]	[+0.49]
ΔE_e (final) = ΔE_e[CBS CCSDT(Q)] + $\Delta E_{\mathrm{AZPVE}}$[CCSD(T)/ANO0] + Δ_{core}[CCSD(T)/cc-pCVTZ] + Δ_{rel}[CCSD(T)/cc-pCVTZ] + Δ_{DBOC}[HF/aug-cc-pVTZ] = 0.49 + 0.08 − 0.00_4 + 0.00_2 − 0.00_4 = **0.57** kcal mol^{-1}							

were precise. The expectation of the spin-squared operator was found in each case to ensure that spin-contamination was not greatly affecting our data. In every case, the expectation value was between 0.7611 and 0.7618. This can be compared to the ideal value of 0.75 for any doublet electronic state. This good agreement allows further confidence in the validity of the present theoretical predictions.

Examining the geometries of all five rotamers, one can see that they are reasonably consistent. Comparing the O-O bond length present in the peroxy moiety, one finds little difference. These bond lengths differ between 1.344 and 1.346 Å for the five rotamers. The C-O bond distances show roughly the same amount of variance. These C-O bond distances fall between 1.458 and 1.461 Å. The reported C_α-C_β equilibrium bond distances only range from 1.523 to 1.526 Å. Likewise, the reported C_β-C_γ equilibrium bond lengths lie between 1.535 and 1.536 Å. Much like their energies, the rotamers are similar with regard to the bond distances between backbone atoms. The angles within all five rotamers are also reasonably similar to one another. Figure 1 contains representations for all of the rotamers for general comparison of geometries. Figure 2 shows the equilibrium structure of the lowest energy rotamer with bond distances and angles labeled.

Because the rotamers are defined in terms of dihedrals, Newman projections for each of the rotamers have been provided (Figure 2.3) in order to explicitly represent the dihedral angles of interest. It is of note that the molecules do not always adhere to the intuitive 60°*gauche* dihedral and 180°*trans* dihedral. One particular offender is the G′G rotamer whose OOCC dihedral is closer to 90 °than either of the idealized dihedrals.

Figure 2.1: Equilibrium structures including point-group symmetry for each of the rotamers of the *n*-propylperoxy radical computed with the CCSD(T)/ANO0 method. See Supplemental Information for bond distances and angles.

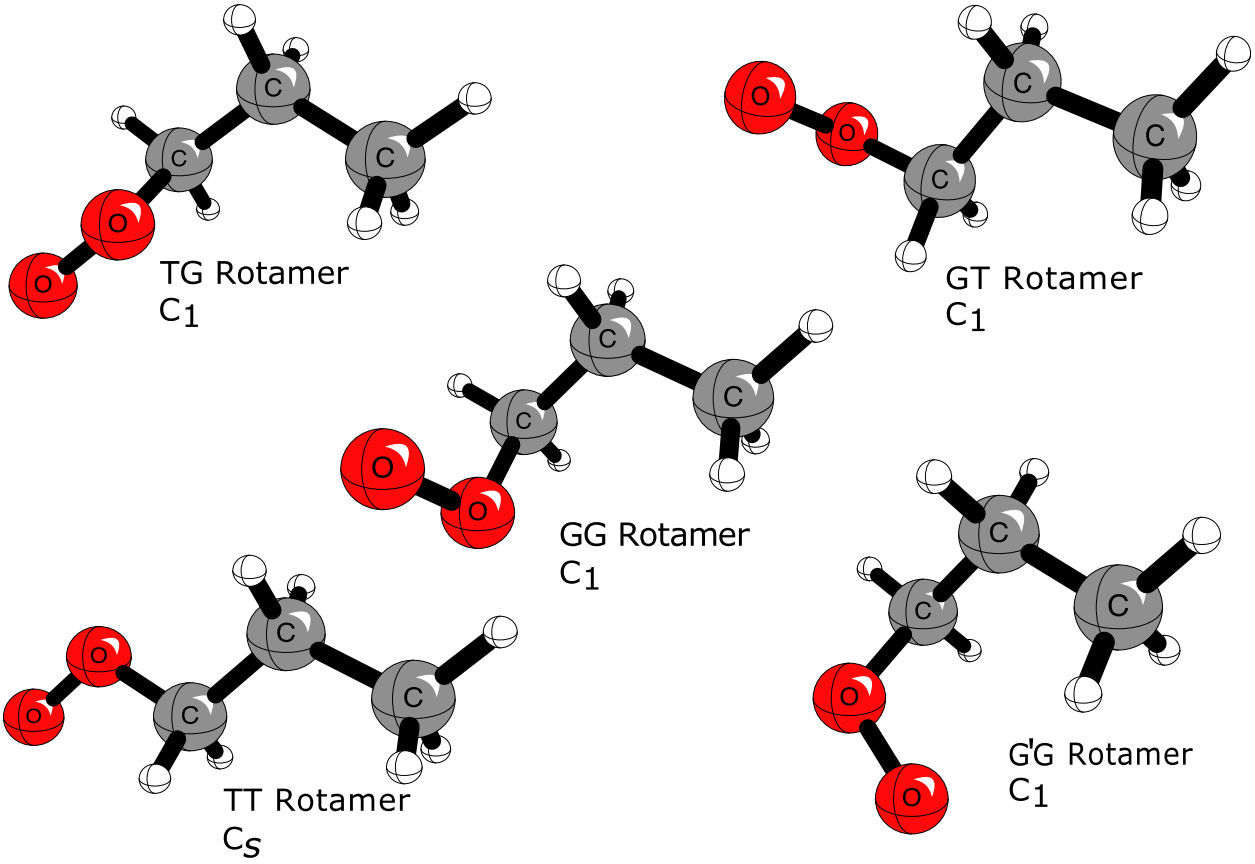

The effects of vibrational averaging are reported in Table 2.7. As can be seen from the table, the vibrational averaging leads to an increase in bond distances in every case. As the molecule vibrates, the nuclei are on average further from one anther. The greatest corrections for vibrational averaging occur for bonds between carbon and hydrogen. This reflects the fact that these C-H bonds which contain the lightest element will undergo relatively large amplitude vibrations. These corrections are very systematic and lie between 0.0214 and 0.0221 Å. Heavier nuclei generally undergo smaller amplitude vibrations. Thus, bond lengths involving these heavier atoms, carbon and oxygen in the case of the *n*-propylperoxy radical, experience smaller corrections when vibrationally averaged. The smallest corrections observed were found in the distance of the O-O bond. Given that the heaviest element present in the *n*-propylperoxy radical is oxygen, this is our most massive bond. The corrections for the O-O bond distance lie between 0.0065 and 0.0068 Å, a full order of magnitude below the corrections for the C-H bond distances. These results support the notion that internuclear distances involving bonds between heavier atoms will see smaller vibrationally averaged corrections than those of bonds involving light atoms such as hydrogen.

Figure 2.2: Equilibrium structure of the lowest energy *gauche-gauche*(GG) conformer of the *n*-propylperoxy radical, computed with the CCSD(T)/ANO0 method, including labeled bond distances in Å and selected bond angles in degrees

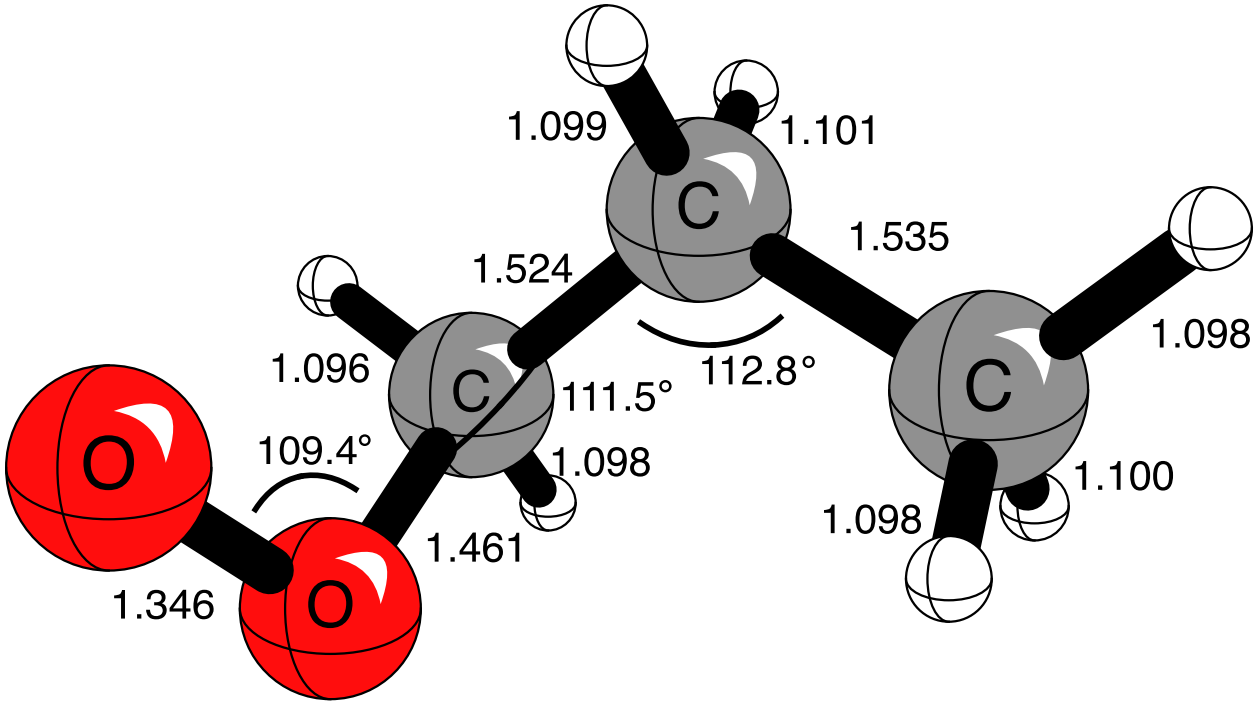

2.4 Conclusion

The five ground state rotamers of the *n*-propylperoxy radical have been studied using high-level *ab initio* methods. Structures for all five of the rotamers are reported with the coupled cluster theory. Geometries for all five rotamers are compared to one another and found to be similar with the exception of the characteristic dihedral angles of these rotamers. Vibrationally corrected bond lengths utilizing the cubic force constants obtained during anharmonic VPT2 computations are also reported. In every case, zero-point vibrations lead to extended bond lengths. The amount of this vibrational extension is related to the anharmonicity experienced by the vibrational modes involving the stretching of these bonds. The C-H bonds, whose bond stretching modes have anharmonic corrections of roughly 150 cm^{-1} experience the greatest degree of extension while the smallest extensions are reported for the O-O bonds whose anharmonic corrections are between 29–35 cm^{-1}.

Accurate relative single-point energies at the CCSDT(Q)/CBS level of theory are reported for each of the rotamers by use of the focal point approach. The lowest energy rotamer is found to be the GG rotamer, followed by the GT, TG, TT and G′G rotamers repectively. The resulting energies, much like the structures, are similar. The reported energies suggest that any population of the *n*-propylperoxy radical would likely

Figure 2.3: Newmann projections for the OOCC and OCCC dihedral angels for each ground state rotamer of the *n*-propylperoxy radical.

GPG OCCC

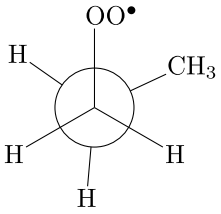

GPG OOCC

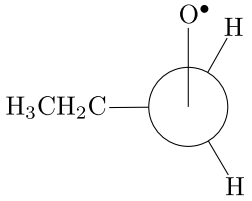

GG OCCC

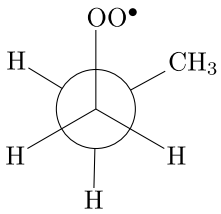

GG OOCC

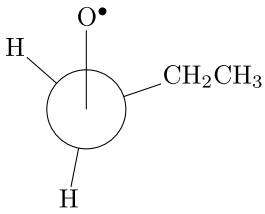

GT OCCC

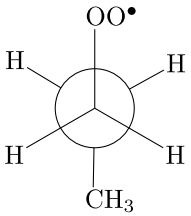

GT OOCC

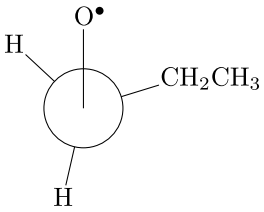

TG OCCC

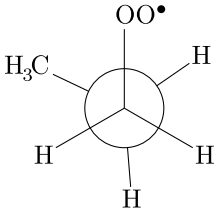

TG OOCC

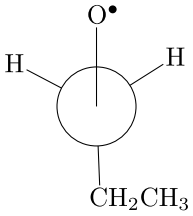

TT OCCC

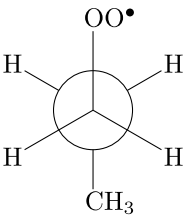

TT OOCC

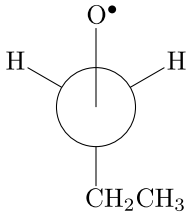

Table 2.7: Equilibrium bond lengths (r_e) versus vibrationally averaged bond lengths (r_g) at 0 K for each of the rotamers of the *n*-propylperoxy radical.

	GG		GT		TG		GPG		TT	
ΔE (kcal mol^{-1})	0.0		0.12		0.44		0.49		0.57	
Bond	r_e	$r_{g,0K}$	r_e	$r_{g,0K}$	r_e	$r_{g,0K}$	r_e	$r_{g,0K}$	r_e	$r_{g,0K}$
O2–O1	1.3456	1.3524	1.3459	1.3527	1.3442	1.3508	1.3460	1.3526	1.3449	1.3514
O2–C$_\alpha$	1.4611	1.4730	1.4578	1.4692	1.4606	1.4725	1.4596	1.4715	1.4583	1.4698
C$_\alpha$–H1	1.0965	1.1183	1.0982	1.1203	1.0970	1.1189	1.0965	1.1183	1.0977	1.1196
C$_\alpha$–H2	1.0985	1.1205	1.0973	1.1192	1.0977	1.1196	1.0978	1.1199	1.0977	1.1196
C$_\alpha$–C$_\beta$	1.5239	1.5347	1.5234	1.5346	1.5227	1.5336	1.5260	1.5369	1.5219	1.5331
C$_\beta$–H3	1.0990	1.1209	1.0986	1.1204	1.1000	1.1219	1.1001	1.1220	1.0994	1.1213
C$_\beta$–H4	1.1008	1.1228	1.0995	1.1214	1.1003	1.1222	1.1014	1.1234	1.0994	1.1213
C$_\beta$–C$_\gamma$	1.5350	1.5469	1.5357	1.5475	1.5357	1.5476	1.5348	1.5466	1.5361	1.5478
C$_\gamma$–H5	1.0976	1.1192	1.0974	1.1188	1.0974	1.1189	1.0969	1.1184	1.0973	1.1187
C$_\gamma$–H6	1.0977	1.1191	1.0992	1.1209	1.0977	1.1192	1.0979	1.1194	1.0991	1.1207
C$_\gamma$–H7	1.0996	1.1212	1.0994	1.1210	1.0995	1.1210	1.0988	1.1205	1.0991	1.1207

contain a mixture of all five rotamers. This mixing of energetically close states leads to difficulty in rotamer specific spectroscopic detection of the *n*-propylperoxy radical. In light of this, fundamental frequencies have been reported in order to assist with this difficult spectroscopic interrogation. With a goal of differentiating the spectra reported for the rotamers, analyses of both the frequencies and intensities of the fundamental vibrational modes is carried out. It is predicted that the most propitious way to specifically detect a given rotamer may be to analyze the C-C bond stretching modes, reported in Table 2.1 as ν_{12} and ν_{13}, occurring near 1400 cm^{-1}. Even if this rotamer-specific detection is not achieved, advances in spectroscopy may soon be able to obtain a vibrationally resolved spectrum for the *n*-propylperoxy radical molecule. The spectroscopic predictions presented in this paper should aid in the assignment of such spectra.

2.5 Supplementary Information

2.5.1 *gauche-gauche* (GG) rotamer

Relative energy: 0.0 kcal mol^{-1}

Molecular point group: C_1

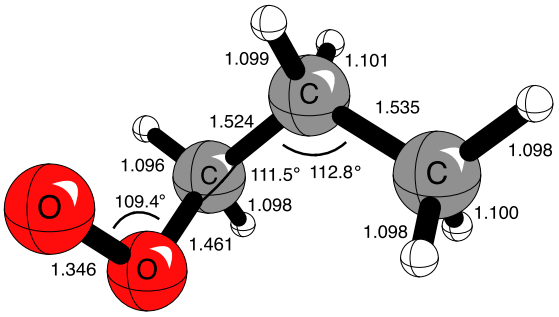

Atom	x	y	z
O	−1.022188	0.044387	−0.615324
O	−1.699747	0.531878	0.440134
C	−0.069169	−0.963637	−0.156620
H	−0.621764	−1.687479	0.454072
H	0.270570	−1.442645	−1.084930
C	1.088390	−0.331312	0.606541
H	0.681960	0.176785	1.492283
H	1.729505	−1.149731	0.968311
C	1.903747	0.646000	−0.251477
H	2.728086	1.080861	0.328312
H	1.272449	1.466989	−0.615327
H	2.335012	0.136394	−1.125171

Table 2.8: Harmonic (ω), anharmonic corrections ($\delta\nu$), and final fundamental frequencies (ν) for the *gauche-gauche* (GG), rotamers for the *n*-propylperoxy radical obtained using the ANO0/CCSD(T) level of theory (cm^{-1}).

	GT		
Mode	ω	$\delta\nu$	ν
1	3148	−152	2996
2	3144	−147	2997
3	3132	−148	2985
4	3108	−147	2961
5	3077	−124	2954
6	3055	−117	2938
7	3048	−127	2957[9]
8	1514	−43	1471
9	1508	−45	1463
10	1486	−42	1444
11	1484	−40	1444
12	1423	−34	1389
13	1396	−35	1361
14	1374	−34	1340
15	1302	−31	1271
16	1281	−31	1249
17	1187	−30	1156
18	1115	−28	1087
19	1096	−33	1063
20	1051	−16	1035
21	947	−18	930
22	895	−21	874
23	863	−15	848
24	757	−10	747
25	543	−5	538
26	431	−4	427
27	290	−7	283
28	226	−8	218
29	153	−8	145
30	81	−4	77

2.5.2 *gauche-trans* (GT) rotamer

Relative energy: 0.12 kcal mol^{-1}

Molecular point group: C_1

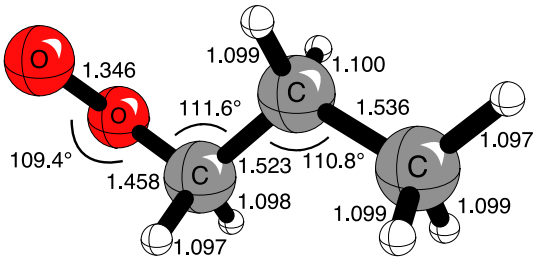

Atom	x	y	z
O	-1.332905	0.483927	-0.275569
O	-1.870963	-0.647561	0.215953
C	0.016465	0.648077	0.251031
H	0.275090	1.686783	0.005438
H	-0.030652	0.529420	1.340884
C	0.989454	-0.336863	-0.384633
H	0.640853	-1.357027	-0.173464
H	0.974973	-0.200940	-1.475639
C	2.409357	-0.129053	0.162280
H	3.111280	-0.838146	-0.294549
H	2.439123	-0.279186	1.250801
H	2.771950	0.887115	-0.048771

Table 2.9: Harmonic (ω), anharmonic corrections ($\delta\nu$), and final fundamental frequencies (ν) for the *gauche-trans* (GT), rotamers for the *n*-propylperoxy radical obtained using the ANO0/CCSD(T) level of theory (cm^{-1}).

	GT		
Mode	ω	$\delta\nu$	ν
1	3148	−152	2996
2	3139	−148	2991
3	3128	−148	2980
4	3110	−147	2963
5	3076	−122	2954
6	3062	−104[10]	2958
7	3045	−78[11]	2967
8	1517	−44	1473
9	1509	−42	1467
10	1502	−47	1454
11	1487	−42	1445
12	1420	−36	1384
13	1409	−38	1371
14	1327	−30	1296
15	1322	−29	1293
16	1281	−34	1248
17	1200	−29	1171
18	1133	−27	1106
19	1094	−35	1060
20	1056	−27	1028
21	961	−26	935
22	897	−12	885
23	876	−15	861
24	761	−5	757
25	557	−7	550
26	373	−8	365
27	262	0	261
28	241	−14	227
29	122	−9	113
30	102	−4	98

2.5.3 *trans-gauche* (TG) rotamer

Relative energy: 0.44 kcal mol^{-1}

Molecular point group: C_1

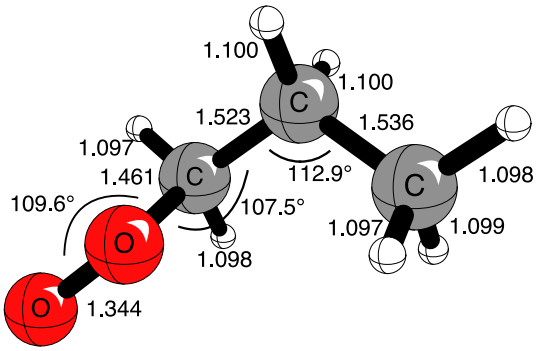

Atom	x	y	z
O	-0.888382	-0.294622	-0.347498
O	-2.141970	-0.237133	0.134378
C	-0.074460	0.743337	0.279912
H	-0.514752	1.713538	0.018794
H	-0.127727	0.597497	1.366589
C	1.346074	0.593511	-0.247641
H	1.332465	0.688641	-1.343409
H	1.928554	1.443253	0.138747
C	2.001355	-0.731941	0.167321
H	1.435732	-1.588108	-0.221715
H	3.028013	-0.797253	-0.215616
H	2.040897	-0.820754	1.262467

Table 2.10: Harmonic (ω), anharmonic corrections ($\delta\nu$), and final fundamental frequencies (ν) for the *trans-gauche* (TG), rotamers for the *n*-propylperoxy radical obtained using the ANO0/CCSD(T) level of theory (cm^{-1}).

	GT		
Mode	ω	$\delta\nu$	ν
1	3146	−148	2999
2	3142	−155	2987
3	3132	−147	2985
4	3102	−147	2955
5	3075	−113	2962
6	3054	−113	2941
7	3049	−90[12]	2959
8	1515	−32	1483
9	1512	−53	1459
10	1501	−44	1457
11	1484	−45	1439
12	1423	−34	1389
13	1404	−42	1362
14	1372	−33	1340
15	1308	46	1354
16	1253	−32	1221
17	1168	−29	1139
18	1133	−27	1106
19	1104	−31	1073
20	1079	−25	1053
21	939	−24	915
22	913	−14	899
23	892	−16	876
24	752	−9	744
25	517	−5	513
26	379	1	380
27	301	−5	295
28	204	−15	189
29	134	−2	132
30	76	−6	69

2.5.4 *gauche′-gauche* (G′G) rotamer

Relative energy: 0.47 kcal mol^{-1}

Molecular point group: C_1

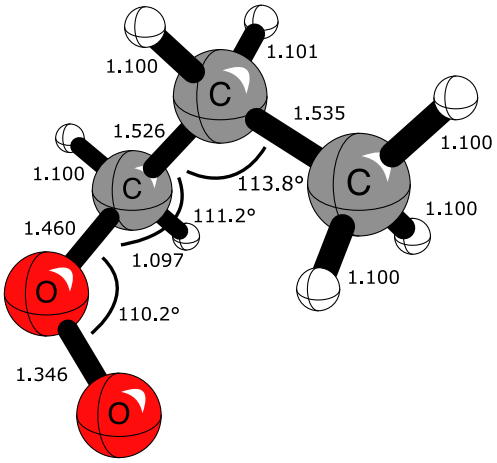

Atom	x	y	z
O	-1.148334	0.345857	-0.389118
O	-1.484118	-0.841571	0.148453
C	-0.074306	0.963495	0.382459
H	-0.211801	0.669616	1.429861
H	-0.243214	2.042403	0.270134
C	1.295472	0.561285	-0.156560
H	1.356756	0.850623	-1.216194
H	2.040772	1.167793	0.381752
C	1.613219	-0.931130	0.009072
H	0.898111	-1.552928	-0.543425
H	2.621049	-1.151417	-0.366668
H	1.568712	-1.227244	1.066320

Table 2.11: Harmonic (ω), anharmonic corrections ($\delta\nu$), and final fundamental frequencies (ν) for the *gauche-trans* (GT), rotamers for the *n*-propylperoxy radical obtained using the ANO0/CCSD(T) level of theory (cm^{-1}).

	GT		
Mode	ω	$\delta\nu$	ν
1	3152	−152	3001
2	3148	−151	2997
3	3135	−148	2986
4	3096	−146	2949
5	3079	−126	2953
6	3052	−129	2959[13]
7	3045	−114	2931
8	1512	−41	1471
9	1507	−41	1466
10	1483	−39	1443
11	1478	−38	1441
12	1426	−34	1392
13	1395	−38	1357
14	1377	−34	1343
15	1301	−22	1279
16	1282	−32	1250
17	1183	−27	1156
18	1115	−28	1087
19	1098	−34	1064
20	1061	−19	1042
21	932	−25	908
22	919	−14	905
23	844	−18	826
24	769	−9	760
25	525	17	542
26	426	−5	421
27	308	−4	304
28	236	−10	226
29	121	−6	115
30	97	−13	83

2.5.5 *trans-trans* (TT) rotamer

Relative energy: 0.57 kcal mol^{-1}

Molecular point group: C_s

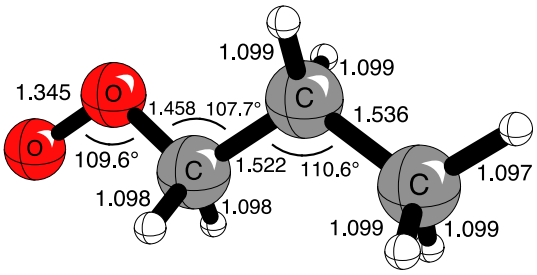

Atom	x	y	z
O	-1.187097	0.472788	-0.000016
O	-2.291325	-0.294882	0.000028
C	-0.001656	-0.376569	-0.000034
H	-0.040110	-1.010972	0.894891
H	-0.040160	-1.011002	-0.894936
C	1.218215	0.533416	0.000001
H	1.183048	1.184488	0.885133
H	1.183058	1.184542	-0.885092
C	2.511501	-0.295357	0.000005
H	3.393351	0.357582	0.000153
H	2.568278	-0.939440	-0.888807
H	2.568251	-0.939472	0.888796

Table 2.12: Harmonic (ω), anharmonic corrections ($\delta\nu$), and final fundamental frequencies (ν) for the *gauche-trans* (GT), rotamers for the *n*-propylperoxy radical obtained using the ANO0/CCSD(T) level of theory (cm^{-1}).

	GT		
Mode	ω	$\delta\nu$	ν
1	3143	−154	2989
2	3140	−148	2992
3	3128	−149	2979
4	3105	−147	2958
5	3073	−108	2965
6	3060	−98[14]	2962
7	3046	−77[15]	2969
8	1520	−43	1477
9	1510	−41	1468
10	1509	−41	1469
11	1500	−49	1451
12	1421	−34	1387
13	1415	−26	1389
14	1328	−29	1299
15	1320	−32	1289
16	1261	−33	1228
17	1171	−30	1141
18	1157	−27	1130
19	1101	−29	1072
20	1064	−29	1035
21	980	−27	953
22	921	−15	906
23	891	−10	881
24	761	−5	756
25	488	−5	483
26	400	−5	394
27	243	−12	231
28	198	−25	173
29	123	−3	120
30	82	−7	75

2.5.6 Resonances

In each case, the GG and G′G rotamer show two type-1Fermi resonances. In order to resolve these resonances, contact matrices were constructed between the fundamental frequency and the frequencies of each of the overtones. The fundamental frequency in each matrix interacts with the overtones via cubic force constants. The interaction between overtones occurs via Darling-Dennison constants which are quartic force constants between the overtones. We follow the same analysis as Li, Agarwal, Allen, and Schaefer.[44] The analysis for the GG rotamer is as follows:

$$\begin{pmatrix} \nu_7 & \phi_{7,8,8}/4 & \phi_{7,9,9}/4 \\ \phi_{7,8,8}/4 & \nu_8 * 2 & K_{8,8,9,9}/2 \\ \phi_{7,9,9}/4 & K_{8,8,9,9}/2 & \nu_9 * 2 \end{pmatrix} = \begin{pmatrix} 2920.7 & 24.5123 & 24.9006 \\ 24.5123 & 2941.3 & 0.454157 \\ 24.9006 & 0.454157 & 2926.2 \end{pmatrix}$$

Diagonalizing this matrix gives the following eigenvalues:

$$\begin{pmatrix} 2964.1 & 0 & 0 \\ 0 & 2932.9 & 0 \\ 0 & 0 & 2891.3 \end{pmatrix}$$

The selected eigenvalue (2964 cm^{-1}) reduces the anharmonic correction from –127 cm^{-1} to –84 cm^{-1}.

The same analysis was applied to the resonances associated with the G′G rotmer.

$$\begin{pmatrix} \nu_6 & \phi_{6,8,8}/4 & \phi_{6,9,9}/4 \\ \phi_{6,8,8}/4 & \nu_8 * 2 & K_{8,8,9,9}/2 \\ \phi_{6,9,9}/4 & K_{8,8,9,9}/2 & \nu_9 * 2 \end{pmatrix} = \begin{pmatrix} 2923.1 & -24.72 & -26.09 \\ -24.72 & 2941.5 & 0.9428 \\ -26.09 & 0.9428 & 2931.8 \end{pmatrix}$$

Diagonalizing this matrix gives us the following eigenvalues:

$$\begin{pmatrix} 2967.3 & 0 & 0 \\ 0 & 2935.8 & 0 \\ 0 & 0 & 2893.3 \end{pmatrix}$$

The adjusted frequency becomes 2967 cm^{-1} and the anharmonic correction is reduced from –129 cm^{-1} to –88 cm^{-1}

CHAPTER 3

FUNDAMENTAL VIBRATIONAL ANALYSES OF THE HCN MONOMER, DIMER AND ASSOCIATED ISOTOPOLOGUES*

*Reprinted from P.R. Hoobler, J.M. Turney, J. Agarwal, and H.F. Schaefer, *ChemPhysChem*, doi:10.1002/cphc.201800728, with permission from Wiley Publishing

3.1 Abstract

In this work we provide high level *ab initio* treatments of the structures, vibrational frequencies, and electronic energies of the HCN monomer and dimer systems along with several isotopologues. The plethora of information related to this system within the literature is summarized and serves as a basis for comparison with the results of this paper. The geometry of the dimer and monomer are reported at the all electron coupled-cluster singles, doubles, and perturbative triples level of theory [AE-CCSD(T)] with the correlation consistent quadruple-zeta quality basis sets with extra core functions (cc-pCVQZ) from Dunning. The theoretical geometries and electronic structures are further analyzed through the use of the Natural Bond Orbital (NBO) method and Natural Resonance Theory (NRT). At the AE-CCSD(T)/cc-pCVQZ level of theory, the full cubic with semi-diagonal quartic force field for nine dimer and four monomer isotopologues (the parent isotopologue along with ^{15}N, ^{13}C, and D derivatives) were obtained to treat the anharmonicity of the vibrations via second order vibrational perturbation theory (VPT2). Lastly, the enthalpy change associated with the formation of the dimer from two monomer units was determined using the focal point analysis. Computations including coupled-cluster through perturbative quadruples as well as basis sets up to six-zeta quality, including core functions (cc-pCVXZ, X=D,T,Q,5,6) were used to extrapolate to the AE-CCSDT(Q)/CBS energy associated with this hydrogen-bond forming process. After appending anharmonic zero-point vibrational, relativistic, and diagonal Born–Oppenheimer corrections, we report a value of –3.93 kcal mol^{-1} for the enthalpy of formation. To our knowledge, each set of results (geometries, vibrational frequencies, and energetics) reported in this study represents the highest-level and most reliable theoretical predictions reported for this system.

3.2 Introduction

The study of small, fundamental chemical systems has a rich history within *ab initio* quantum chemistry.[59] The ability to predict small spectroscopic effects with high-accuracy and glean insight into the underlying chemical behavior attracts chemists, both theoretical and experimental, to investigate systems like the hydrogen cyanide (HCN) dimer. The latest studies on the linear dimer system study both its spectroscopy[60] and stabilization by complexation with a Lewis acid.[61] The monomer has also been of great interest to those studying pre-biotic chemistry[62–66] due to the fact that its reactive polymerization can lead to the formation of simple amino acids via diaminomaleonitrile,[65] a tetramer of HCN.

The linear chains formed by the hydrogen-bonded polymerization of HCN have been of great interest to those studying the cooperative effect of hydrogen-bonding interactions on polymeric properties within the gas phase.[67–74] The dielectric constants found in the liquid[75] and crystal phases[76] of HCN also suggest a cooperation of interactions between monomer units.

The interaction between monomers gives rise to spectral features that are of interest within this study. The lowest frequency vibrational modes in the spectrum are degenerate inter-monomer bending modes. These modes have frequencies measured near 40 cm^{-1} by gas phase IR.[77] Low frequency modes with large amplitudes are notoriously hard to accurately treat due to the "flatness" of the potential energy surface associated with these modes. These modes may present a challenge for modern vibrational analysis methods such as second-order vibrational perturbation theory (VPT2). Also interesting is the coupling of the C–H stretching modes with the lower frequency modes of the dimer. It is here that a distinction between the proton donor monomer and the proton acceptor monomer is necessary. In their 1999 study, Nauta and Miller concluded that the internal (donor monomer) C–H stretch couples more favorably with lower frequency modes than the external (acceptor monomer) C–H stretch.[78] Coupled analysis of these modes is made more difficult due to the reliance of the internal C–H stretch upon the highly anisotropic inter-monomer interaction.

Prior experimental work on the dimer system includes crystal studies[76,79,80] as well as studies of the dielectric constant of liquid phase HCN.[75] Several groups employing microwave spectroscopy[81–84] have determined the rotational r_0 structure and rotational constants of the parent and substituted isotopologues of the dimer. Several IR studies, utilizing matrix isolation,[85–91] gas phase,[60,77,92–97] and super-fluid helium,[78] have also added to the wealth of experimental results available for this dimer system. These experimental findings are complimented by many theoretical studies.[67,68,71,80,98–109] The fact that the HCN dimer has been so well characterized, coupled with the size and symmetry of the system, allows us the opportunity to study the system at a high level and determine the efficacy of our high-level methods to describe a non-covalently bound system.

Many microwave studies and rotationally resolved IR studies report values for the rotational constant of the HCN dimer. The earliest study to report the rotational constant for this dimer system was that of Legon et al.[81] This study reported rotational constants for the isotopically di-substituted dimers for both deuterium and ^{15}N. This work was closely followed by Brown et al.[82] who measured a value for the rotational constant in agreement with that of Legon et al. Along with the parent isotope, they also investigated the rotational constant of the di-substituted ^{15}N dimer isotope. From their study they were also able to obtain centrifugal distortion constants (D_J). Buxton, Campbell, and Flygare[83] later measured the rotational spectrum of the dimer, and reported a rotational constant that was roughly 40 MHz lower than that of the previous studies for the parent isotope. The Buxton study was able to achieve much colder temperatures[110] (<10K)

for their rotational spectrum leading them to conclude that the previous studies had not measured the vibrational ground state.[83] Along with corrected rotational constants, they reported a reliable r_0 structure for the dimer and isotopically substituted species.[83] A later study by Fillery-Travis, Legon, Willoughby, and Buckingham[84] would add rotational constants, centrifugal distortion contants, and nuclear quadrupole coupling constants for the deuterated, ^{15}N dimer isotopologue. Rotationally resolved IR studies such as that of Jucks and Miller,[77] have reported rotational constants for the vibrational ground state that support the values measured by Buxton and co-workers.

The most recent study of the dimer system, published by Mihrin and co-workers,[60] studied the dimer via Fourier transform tera-Hz spectroscopy. Utilizing this method, they were able to observe, to a very high precision, the fundamental vibrational frequency, ν_8 which they refer to as the "donor libration" vibrational mode. This represents the first time that this particular mode has been experimentally observed. In addition to the high-level experiment, they report theoretical results at the CCSD(T)-F12b/aug-cc-pVQZ level of theory.

Another recent vibrational study on the dimer system was performed via superfluid helium nanodroplet infrared spectroscopy. This study, performed by Nauta and Miller in 1999,[78] reports a frequency of 3308.07 cm^{-1} for the acceptor C–H stretch (ν_1) as well as a frequency of 3237.57 cm^{-1} for the donor C–H stretch (ν_2). For the C–N stretching modes, an argon matrix study by Pacansky in 1977 reports frequencies of 2112 and 2093 cm^{-1} for ν_3 and ν_4, respectively.[86] Pacansky was also able to assign peaks for the degenerate H-C-N bending for both monomer units. The higher frequency of the bending modes belongs to the bonded HCN bend while the lower frequency belongs to the free HCN bend. Finally, Jucks and Miller[94] were able to assign the lowest frequency dimer bending mode in their rotational resolved gas-phase IR study.

The goal of this research is to provide a comprehensive, very high level theoretical treatment of the HCN dimer as an example dealing with a linear polyatomic system that contains important long-range, anisotropic interactions.

3.2.1 Theoretical Methods

Reference geometries for both the monomer and dimer were optimized using the coupled-cluster singles, doubles, and perturbative triples [CCSD(T)] level of theory. This level of theory was coupled with the cc-pCVQZ basis set, a large (396 functions for the dimer and 198 functions for the monomer), quadruple-ζ basis set that also includes tight functions necessary for describing the core ($1s$-like) electrons of carbon and nitrogen in the HCN monomer and dimer. By including the core electrons explicitly within the computations we obtain AE-CCSD(T)/cc-pCVQZ geometries. This pairing of theory and basis set has been shown to provide good results for anharmonic analysis of linear systems containing carbon multiple bonds.[111,112]

Complimenting these geometry optimizations, natural bond orbital theory along with natural resonance theory have been used to elucidate meaningful bonding effects relevant to the dimer geometry. This analysis was done at the B3LYP/cc-pVTZ level of theory within the NBO 5.0[113] computational suite with utilization of natural resonance theory.[114–116]

Vibrational analysis for the monomer and dimer species along with isotopologues was performed via VPT2, utilizing full cubic and semi-diagonal quartic force-fields. The equilibrium geometry used for each of the isotopologues was the AE-CCSD(T)/cc-pCVQZ geometry of the parent. This is valid because without vibrational averaging, the equilibrium geometry is based upon electronic structure and independent of the mass of nuclei. In order to compute the semi-diagonal quartic force field, normal coordinates were used, which are by nature mass-dependent. The result of this was that each istopologue was obtained with a unique set of displacements. Further analysis testing the effect of removing ν_5 and ν_9, along with the associated force constants, from the VPT2 treatment was done using the PYVPT2 program of Agarwal.[50]

The focalpoint analysis (FPA)[14–16,117] was used to accurately determine the enthalpy of formation of the dimer from two monomer units. Using the aforementioned reference geometries, single point energies computed with coupled-cluster theory up through perturbative quadruple excitations [CCSDT(Q)], utilizing Dunning's core basis sets through six-ζ quality (cc-pCV6Z). Extrapolations to the complete basis set (CBS) limit were made via Feller's[18] three-point scheme for Hartree–Fock (HF) energies

$$E_{\mathrm{HF}}(X) = E_{\mathrm{HF}}^{\infty} + ae^{-bX} \tag{3.1}$$

and Helgaker's[19] two-point extrapolation scheme for correlated methods:

$$E_{\mathrm{corr}}(X) = E_{\mathrm{corr}}^{\infty} + aX^{-3} \tag{3.2}$$

Within single-point energy computations, approximations were accounted for using several well-known corrections. In order to account for possible non-adiabatic effects the diagonal Born–Oppenheimer correction was computed at the HF/cc-pCVTZ level of theory. Corrections for the non-relativistic assumption concerning the wave function were computed using second-order direct perturbation theory of the Dirac equation (DPT2)[118–122] computed at the CCSD(T)/cc-pCVTZ level of theory. The final correction to the electronic energies was the addition of zero-point vibrational energies. These corrections were based upon the anharmonic frequencies obtained from the VPT2 treatment previously described. The enthalpy of formation of the dimer from monomer units was determined as the difference in twice the monomeric enthalpy and the final enthalpy of the dimer. All optimized geometries, force constants, and single point energies were obtained using CFOUR 2.0.[49]

3.3 Results

Figure 3.1: The equlibrium geometry of the HCN monomer and dimer obtained with the AE-CCSD(T)/cc-pCVQZ level of thoery. All bond lengths labeled in Angstroms.

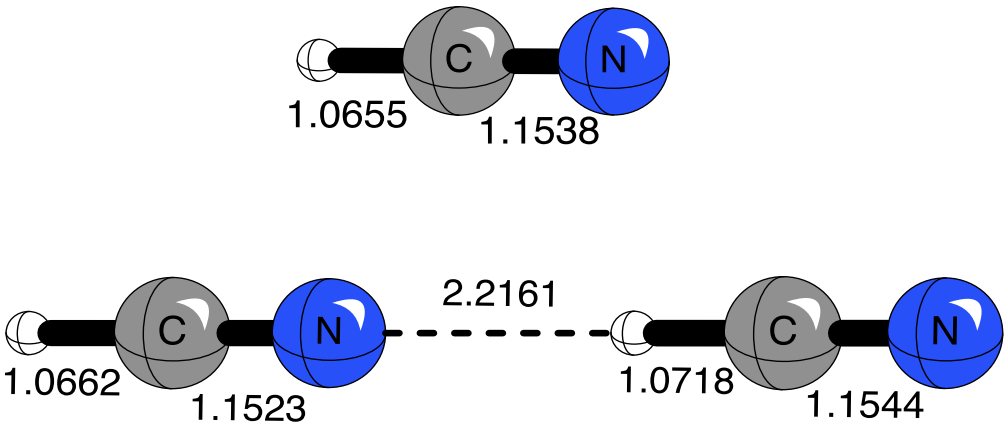

3.3.1 Geometry

The geometry for the dimer may be compared with previous studies. Buxton and co-workers[83] reported a rotationally determined r_0 structure for the dimer with an inter-monomer C$\cdots$N of 3.2874 Å. By adding the C-H and N$\cdots$H distances of our r_e geometry we can report this distance at 3.2879 Å. This result is closer to experiment than should be expected when comparing r_0 to r_e structures. However, when paired with the computed rotational constant at the AE-CCSD(T)/cc-pCVQZ which shows excellent agreement (Table 3.1), we can be confident that we have the correct structure for the dimer.

Table 3.1: Rotational constants (MHz) for the HCN dimer and several isotopomers obtained at the AE-CCSD(T)/cc-pCVQZ level of theory.

Isotopologue	B_e	B_0	B_0 exp.
$HC^{14}N\cdots HC^{14}N$	1748.115	1740.547	1745.810[a]
$HC^{15}N\cdots HC^{15}N$	1686.742	1679.399	1684.288[a]
$HC^{15}N\cdots HC^{14}N$	1732.607	1724.884	1729.921[a]
$HC^{14}N\cdots HC^{15}N$	1702.388	1695.337	1700.302[a]
$DC^{14}N\cdots DC^{14}N$	1661.720	1657.209	1661.18[b]
$DC^{15}N\cdots DC^{15}N$	1605.445	1600.933	1604.495[c]
$DC^{15}N\cdots HC^{15}N$	1607.496	1601.122	1605.695[c]
$HC^{15}N\cdots DC^{15}N$	1684.941	1679.569	1683.374[c]

a - Buxton *et al.*[83] *b* - Georgiou *et al.*[123] *c* - Fillery-Travis *et al.*[84]

Table 3.2: Comparison of the Natural Populations of the C-H σ^* orbitals within the HCN monomer, and analogous monomer-like units within the dimer.

σ^*_{CH}	Population
Monomer	0.011
Donor HCN	0.023
Acceptor HCN	0.010

It can be seen that the monomer-like fragments of the dimer show some distortion with respect to the lone monomer. In fact, three of the four bonds within the monomer units show at least a slight lengthening with the largest such increase occuring in the proton-donor C–H bond. The only bond to contract slightly is the proton-acceptor C–N triple bond. These results may be viewed in light of the current understanding of hydrogen-bonding as studied by electronic structure theory. Our NBO-NRT results, discussed below, will become helpful in resolving these trends.

Comparing the orbital occupations for the monomer and dimer, it may be seen that the electron population within the antibonding σ^*_{CH} orbital of the proton donor increases with dimer formation. In fact, the population more than doubles, going from a natural population of 0.011 in the lone monomer to 0.023 in the dimer, according to NBO theory. The populations of the σ^*_{CH} orbitals are reported in Table 3.2. The σ^*_{CH} of the proton acceptor actually sees a slight decrease in population which alone would cause the bond length to contract. However, this effect is met with a corresponding decrease in population of the σ_{CH} orbital. These effects appear to nearly perfectly cancel out, and the result is a bond length that is only slightly elongated.

The changes to the lengths of the triple bonds present in the dimer can be better understood through this same NBO analysis. According to the NBO analysis, there are relevant donations from the σ C-N bonding orbitals into the adjacent σ^* C-H antibonding orbitals on the same monomer unit. At the same time, NBO shows a donation from the σ C-H bonding orbitals into the adjacent σ^* C-N antibonding orbitals. The combined effect of these donations should lead to a bond stretching. Overall, the outer C-N triple bond experiences a slight stretching although very slight and is almost unchanged due to dimer formation. The

Table 3.3: Natural population analysis comparing the HCN monomer and dimer systems.

Atom	Natural Charge	Core	Valence	Rydberg	Total
HCN Dimer					
H	0.231	0.000	0.768	0.001	0.769
C	0.131	1.999	3.840	0.029	5.869
N	−0.350	2.000	5.318	0.032	7.350
H	0.240	0.000	0.758	0.002	0.760
C	0.078	1.999	3.891	0.032	5.922
N	−0.330	2.000	5.301	0.030	7.330
HCN Monomer					
H	0.222	0.000	0.776	0.002	0.778
C	0.078	1.999	3.892	0.031	5.922
N	−0.300	2.000	5.271	0.030	7.300

internal C-N triple bond, however, shows a slight contraction, meaning that another effect is overtaking the loss of bonding and increase in anti-bonding character. This result is likely explained via the natural population analysis which shows that the nitrogen is becoming more negatively charged while the carbon becomes more positively charged. These results have been reported in Table 3.3. This favorable shift in charges most likely results in an attractive electrostatic force which leads to the observed bond contraction.

As noted by a referee, this contraction of the triple bond could also be attributed to changes in the dipole moment of each of the monomer units. Contraction of the CN bond in the acceptor along with elongation of the CH bond in the donor increases the dipole moment for each monomer unit. This in turn leads to an increase in the attractive electrostatic dipole-dipole forces during the formation of the dimer. A recent study by McDowell[124] shows results for related systems that would be consistent with this view.

3.3.2 Fundamental Frequencies

Dimer Frequencies

We report the theoretical vibrational frequencies in Table 3.4 along with frequencies reported from experimental studies for comparison.

VPT2 analysis occasionally experiences issues with Fermi resonance type terms based upon accidental near degeneracy between fundamentals and vibrational hotbands or strong interactions observed as large cubic force constants.[5] Our results show no Fermi resonances between the modes. This is determined using the default CFOUR[49] cutoffs of 50 cm^{-1} for the difference between cubic force constants and 80 cm^{-1} for cubic force constants themselves as indicators of resonances which may have adverse effects upon the vibrational analysis. Therefore, we are able to report clean results at our level of theory for every mode present in both the monomer and dimer.

Table 3.4: Harmonic and anharmonic vibrational frequencies (in cm^{-1}) obtained at the CCSD(T)/cc-pCVQZ level of theory with comparison to experiment.

		AE-CCSD(T)/cc-pCVQZ			Expt. Values
Mode	Description	ω	$\delta\nu$	ν	
$\nu_1(\sigma)$	Acc. C–H str	3440	−130	3310	3308.32[a],3308.07[b]
$\nu_2(\sigma)$	Don. C–H str	3363	−115	3248	3241.56[a],3237.57[b]
$\nu_3(\sigma)$	Acc. C–N str.	2147	−32	2114	2104.6[c],2112[d]
$\nu_4(\sigma)$	Don. C–N str.	2127	−27	2100	2094.7[c],2093[d]
$\nu_5(\sigma)$	H ⋯ N str	118	−6	112	101[e]
$\nu_6(\pi)$	Don. HCN bend	814	−41	773	796[f]
$\nu_7(\pi)$	Acc. HCN bend	735	−9	726	733[f]
$\nu_8(\pi)$	$(HCN)_2$ bend	136	−16	120	119.12[g]
$\nu_9(\pi)$	$(HCN)_2$ bend	46	−9	37	40.75[a]

a - Jucks and Miller[77,94] - Gas-phase IR *b* - Nauta and Miller[78] Superfluid He *c* - Dyke *et al.*[125] Raman
d - Pacansky *et al.*[86] Ar Matrix *e* - Legon *et al.*[123] Microwave
f - Satoshi *et al.*[126] Ar Matrix *g* - Mihrin *et al.*[60] THz Radiation

Several gas-phase vibrational frequencies have been reported for the dimer, which are most useful for comparison with our results. We also include frequencies obtained in liquid helium droplets[78] which show only minor differences from gas-phase values and argon matrix frequencies which show minor differences from the gas-phase values. Nevertheless, all these values represent high-level experimental work that has been done on this system, and are thus worthy of discussion.

The gas-phase frequencies reported within two 1988 studies performed by Jucks and Miller[77,94] are a reliable experimental source for comparison with our computed frequencies. It can be seen that the frequencies we report for both the acceptor (3310 cm^{-1}) and donor (3248 cm^{-1}) C–H stretching fundamentals, ν_1 and ν_2 respectively, show close agreement with the reported gas-phase values (3308.32 and 3241.56 cm^{-1} for ν_1 and ν_2 respectively). In particular, the value of the fundamental frequency for ν_1 shows remarkable agreement with the gas-phase experiment. It can be seen that ν_2 shows somewhat poorer agreement between our results and gas-phase experiment than its counterpart. The general difficulty of modeling the modes involving the hydrogen bond, which is evident throughout our results, will be discussed at the end of this section.

The same gas-phase studies[77,94] reported a value for the intermolecular bending mode as the difference between the combination band $\nu_1 + \nu_9$ and the hot band originating from a state in which one quantum of vibrational energy was already present in the ν_9 mode. By subtracting the band origins for both of these transitions, they estimate that the fundamental frequency for ν_9 is 40.75 cm^{-1} which is in satisfactory agreement with the value of 37 cm^{-1} that we report for this fundamental within our analysis.

For comparison to the C–N stretching modes (ν_3 and ν_4) of the dimer, we look to the experiments of Dyke *et al.* who observed frequencies for the dimer via coherent anti-Stokes Raman spectroscopy for ν_3

and infrared spectroscopy for ν_4.[125] They also obtained frequencies for the deuterated system which we will discuss later in this paper. The frequencies reported in their study show excellent agreement again with our computed frequencies although some variance is seen. As with the C–H stretching modes, we see that our computed fundamental for an external (C–H for the acceptor monomer and C–N for the donor monomer) vibrational motion (ν_4) shows better alignment with experiment than that for the the internal vibrational motion.

The intermonomer stretch, ν_5 was observed as a vibrational satellite in the rotational study of Legon and coworkers.[123] We do see a large percent error, roughly 10% (but only 11 cm^{-1}), between the experimental frequency and theory. Legon and coworkers do not directly observe the vibrational band but determine the value based upon a fit to their observed rotational spectrum. Their fit was based upon fixed monomer geometries which raises some concern given that the monomer units show some distortion upon formation of the dimer. We find no reason to doubt the efficacy of our theoretical methods based upon this discrepancy, though further investigation of this mode presents an interesting avenue for future study.

The only dimer bands that have not been assigned in the gas-phase are the analogs of the degenerate monomer unit bends ν_6 and ν_7. These bands have been identified via argon matrix isolation.[126] It can be seen that our values differ somewhat from those found in the matrix. Looking at the reported spectrum of Satoshi and coworkers, it can be seen that the peak at 796 cm^{-1} is very broad which is not surprising given that it is the bending modes associated with the proton donor monomer unit. The spectrum shows a significant tail feature which, if taken into account, would bring the results into much better agreement with our computed frequencies. The lower peak they report at 733 cm^{-1} is a much sharper and intense peak. We see a much smaller difference of 7 cm^{-1} ($< 1\%$ difference) associated with this mode. We conclude that with the proper considerations, our theoretical frequencies are in acceptable agreement with these experimental results.

The last mode to be discussed is the most recently observed. Mihrin and coworkers[60] very recently observed the ν_8 band via THz spectroscopy utilizing synchrotron radiation. Our value matches to within one wavenumber and represents an excellent comparison for our VPT2 results.

Mihrin and coworkers[60] also did a high-level theoretical workup of the vibrational spectrum of the HCN dimer species, though they did not go beyond the harmonic approximation. They report frequencies at the CCSD(T)-F12b explicity correlated level of theory while utilizing an augmented quadruple-ζ quality basis set (aug-cc-pVQZ). This represents a different, comparable theoretical approach which can lead to worthwhile discussion, even if restricted to the harmonic level. The augmented functions they use can help describe long range interactions such as the hydrogen bonding interaction which forms the dimer. Core basis functions, included in our research, are used with the intention of describing the densely populated multiple bonds

within the monomer units themselves. As it is, the theoretical harmonic frequencies reported in both studies show overall agreement, never differing by more than 10 cm^{-1}. This may mean that quadruple-ζ basis sets are large enough that they may be reaching the saturation point of basis functions where only very small effects will be observed by increasing basis set size.

Removal of Low-Frequency Modes

Modes that are difficult to treat at second order of perturbation theory may negatively influence the analysis for each of the other modes. Low-frequency modes can be problematic for VPT2. Bending modes, in particular ν_9, can be difficult to describe via vibrational perturbation theory. It is worthwhile to determine the effect of removing these more problematic modes. We have done this analysis for the lowest frequency modes ν_5 and ν_9. The analysis was done using the PYVPT2 program of Agarwal.[50] It is worth mentioning that the VPT2 equations and cutoffs for defining resonances used within this program are identical to those used in CFOUR. The only difference between these results and those in Table 3.4 is the removal of low-lying modes and their force constants from the VPT2 procedure. In Table 3.5, we present this analysis, completed for only the parent isotopologue. From the results in Table 3.5, it can be seen that removal of the lowest frequency modes has some marginal effect on the frequencies observed. The removal of only ν_9 appears to bring our results into the best agreement with the experimental results found in Table 3.4. Although the agreement for ν_1 gets slightly worse, most of the other modes show some sort of marginal improvement. The most improved mode appears to be ν_5, which sees a change of 5 cm^{-1} with respect to the initial analysis. This 5 cm^{-1} change brings the theoretical value closer to experiment by roughly half of the difference found in Table 3.4. The other π modes show very small changes, with ν_6 seeing slight improvement and ν_8 seeing slight detriment with respect to experiment.

Another mode where our results are less than perfectly matched with experiment was that of ν_5, which prompts us to consider it in this analysis. Removal of ν_5, the lowest frequency mode of σ symmetry, from our analysis yields less favorable results than that of ν_9. None of the σ modes changes by more than a wavenumber. The π modes show small corrections with the exception of ν_9 which shows a change of 4 cm^{-1}. This does bring the computed frequency into better agreement with the experimental frequency reported in Table 3.4. However, the fact that these two modes both show a strong effect on one another, coupled with the fact that they show the largest percent differences within our original results leads us to examine the effect of removing both modes from our analysis. The frequencies obtained in this way can be seen in Table 3.5. One can readily see that this has adverse effects upon ν_1 but shows mild improvement or has no effect upon the remaining σ modes.

Table 3.5: Comparison of fundamental frequencies obtained while removing the lowest frequency modes from the VPT2 analysis

				Modes Removed									
	No Modes Removed			ν_9		ν_5		ν_9,ν_5		ν_8		ν_9,ν_8,ν_5	
Mode	ω	$\delta\nu$	ν	$\delta\nu$	ν	$\delta\nu$	ν	$\delta\nu$	ν	$\delta\nu$	ν	$\delta\nu$	ν
1	3440	−130	3310	−135	3305	−130	3310	−136	3304	−132	3308	−136	3304
2	3363	−115	3247	−119	3244	−117	3246	−121	3242	−127	3236	−132	3231
3	2147	−34	2113	−35	2112	−34	2113	−33	2113	−39	2107	−29	2117
4	2127	−28	2099	−32	2094	−28	2099	−32	2094	−44	2083	−27	2100
5	118	−6	112	−11	107	0	118	0	118	−4	114	0	118
6	814	−40	773	−38	775	−39	775	−35	779	−31	782	−25	788
7	735	−9	726	−12	724	−9	726	−11	724	−10	726	−12	723
8	136	−16	120	−19	117	−15	121	−18	118	0	136	0	136
9	46	−11	35	0	46	−7	39	0	46	−21	26	0	46

Monomer Frequencies

The vibrational frequencies for the monomer have been known for much longer than the dimer. Observed in 1956 by Plyler and coworkers,[127] the frequencies have been reported in this paper. Their values of 3311.4 cm^{-1}, 2096.61 cm^{-1} and 711.90 cm^{-1} agree well with our results shown in Table 3.6. Much like what was found for the dimer, our results are in best agreement with the C–H stretching mode, $\nu_1(\sigma)$. We do very well with all of the monomer modes showing that our method very effectively treats the monomer. Because within the dimer we still see very monomer-like behavior, our success with the monomer lends additional weight to the validity of our dimer results.

We also include vibrational frequencies of three isotopologues in Table 3.6. The effects shown by isotopic substitution can be seen to be very similar to those in the dimer. The greatest effect can be seen with deuterium substitution, and though its largest effect can be seen, as expected in the C–D stretch, the C–N stretch and bending modes also show large shifts of 8% and 20% relative to the frequencies of the parent isotopologue. Substituting nitrogen-15 has a much smaller effect, which is in line with previous discussion. The relative change in mass by substitution of deuterium is much larger than the relative change in mass from nitrogen-15. This in turn has a much larger effect upon the reduced mass associated with each of the vibrational modes. The larger isotopic shift by deuteration is in contrast with smaller shift caused by addition of nitrogen-15 that we observe, as expected.

Isotopologues

Given the amount of research that has been produced for the isotopologues of the dimer system, we seek to provide a comprehensive theoretical set of predictions for comparison with existing experimental data and for prediction of properties of non-standard isotopologues which have not been studied before. Specifically,

Table 3.6: Anharmonic vibrational frequencies (in cm^{-1}) of the HCN monomer, parent and associated isotopologues, obtained at the CCSD(T)/cc-CVQZ level of theory. Experimental frequencies from Plyler *et al.*[127] are included for comparison with the with the parent isotopologue.

	$\nu_1(\sigma)$	$\nu_2(\sigma)$	$\nu_3(\pi)$
This work	3313	2102	715
Plyler *et al.*	3311.4	2096.61	711.90
DCN	2632	1930	571
$HC^{15}N$	3312	2070	715
$DC^{15}N$	2624	1905	570
$H^{13}CN$	3295	2069	710

we have chosen to study isotopologues for which rotational constant data exists, but no vibrational frequency data has been reported. For reference, the rotational results, along with our predicted rotational constants, can are reported in Table 3.1.

Table 3.7 contains the harmonic and fundamental vibrational frequencies for the parent isotopologue and each of the relevant non-standard isotopologues. The predictably large shifts in C–H frequencies upon deuteration provide the most readily apparent trend that can be seen in the results in Table 3.7. This is due to the combination of the fact that these are the largest frequency modes and the fact that deuteration has the largest impact on the reduced mass associated with these modes. The opposite argument can be used to rationalize the computed lack of shifts in the intermonomer hydrogen bond stretching mode.

By suggestion of a referee, we look to an interesting analysis utilized by Buckingham and Fan-Chen[128] which explores the difference in energy between hydrogen bonds and deuterium bonds. They're analysis, using the frequencies reported by King and Nixon[85] they predict DCN$\cdots$HCN would be energetically favored over HCN$\cdots$DCN by 5 cm^{-1}. Using our values for the modes computed here, we find that we agree qualitatively that the hydrogen-bonded dimer should be energetically favored but only by 3.5cm^{-1}. Despite the fact that this is a very small energetic difference, the difference between hydrogen and deuterium bonds represents an interesting area of thought and research.

Upon deuteration and addition of ^{15}N, these modes show very little shift. The low frequency of this mode and the relatively large reduced mass of these modes mean that the isotopic substitution has very little effect upon the frequencies. Thus there are no shifts of greater than 4 cm^{-1} for these modes.

One of the more interesting results that can be seen is the shifts in the C–N stretching modes due to deuteration of the monomer unit. The large isotopic shifts, 177 cm^{-1} for ν_3 and 186 cm^{-1} for ν_4, are partly due to the large frequencies. These shifts represent a shift of less than 10% of the modes of the standard isotopologue, compared to the 20% isotopic shifts that we see in the C–H stretching frequencies. Though they are smaller, they speak to the fact that hydrogen/deuterium is involved in the vibrational mode, despite it being labeled a C–N stretch. Looking at the displacements, the H/D–C moiety behaves as a single entity, leading to an isotopic shift when each monomer unit is deuterated.

Our results within Table 3.7 also include data for the carbon-13 substituted dimer systems. It can be seen that the heavier isotope does cause a shift in the C–H stretching modes. This effect is much less than that of deuteration but is observable with a difference of 17 cm^{-1} for the acceptor stretch with the acceptor carbon substituted and 18cm^{-1} for the donor C–H stretch with the donor carbon substituted with the heavier isotope. These shifts are roughly 0.5% with respect to the fundamentals of the parent isotope which is significantly smaller than the effect of deuteration.

The last observation of note regards the degree to which the individual monomer units maintain their own identity, despite the somewhat strong hydrogen bond between them. It is clear from the results in Table 3.7 that an isotopic change in one monomer unit has little to no effect on the vibrational frequencies computed for the other monomer. This is observed unanimously and may be rationalized by the fact that the electronic structures of the monomer units themselves are not changed much upon dimerization. The subtle charge transfer effects discussed in the NBO section of this paper, although they lead to an attractive interaction between the monomers, do not have a large effect on the monomer-like molecular orbitals. In the end, this means that the normal modes, with the exception of the intermonomer modes, which only exist upon dimerization, remain monomer-like, as they result from forces on the nuclei which are similar to the forces felt within the monomers.

3.3.3 Energetics

The results of the focal point analysis of the 2 HCN $\rightarrow$ $(HCN)_2$ association energy are presented in Table 3.8. It can be seen that the system shows excellent convergence both with regard to correlation and basis set size. Looking at the purely electronic results, we can use the highest level of correlation [(Q)] with the cc-pCVTZ basis set increment as a rough estimate in the error of our answer. This gives our electronic energy at this geometry a rough error estimate of 0.01 kcal mol^{-1}. Given the earlier discussion of the quality of our geometry, this electronic energy can definitely be considered trustworthy for comparison to other reported values. The largest correction to the electronic energy is, unsurprisingly, the anharmonic zero-point vibration energy (AZPVE). The AZPVE correction is positive, thus reducing the computed binding

Table 3.7: Harmonic and anharmonic frequencies (in cm^{-1}) obtained at the CCSD(T)/cc-pCVQZ level of theory for the parent istopologue and associated isotopologues of the HCN dimer. Refer to Table 3.4 for a description of each mode.

Istopologue	HCN···HCN			DCN···HCN		HCN···DCN		DCN···DCN		$H^{13}CN$···HCN		HCN···$H^{13}CN$		$HC^{15}N$···HCN		HCN···$HC^{15}N$		$HC^{15}N$···$HC^{15}N$		$HC^{15}N$···$DC^{15}N$		$DC^{15}N$···$HC^{15}N$		$DC^{15}N$···$DC^{15}N$	
Mode	ω	$\delta\nu$	ν	ω	ν	ω	ν	ω	ν	ω	ν	ω	ν	ω	ν	ω	ν	ω	ν	ω	ν	ω	ν	ω	ν
1	3440	-130	3309	2708	2635	3440	3310	2708	2635	3420	3292	3440	3310	3438	3308	3440	3310	3438	3308	3438	3308	2698	2625	2699	2625
2	3363	-115	3247	3363	3247	2662	2597	2662	2596	3363	3247	3343	3229	3363	3247	3361	3246	3361	3246	2652	2586	3361	3246	2652	2586
3	2147	-34	2113	1964	1937	2146	2115	1964	1937	2128	2101	2146	2114	2111	2081	2146	2114	2113	2082	2112	2082	2094	2068	1938	1912
4	2127	-28	2099	2127	2101	1936	1914	1935	1914	2111	2080	2093	2067	2128	2101	2094	2068	2093	2068	1911	1890	1938	1912	1910	1890
5	118	-6	112	117	109	117	110	116	109	117	110	117	110	117	109	117	110	116	109	115	108	115	107	114	107
6	814	-40	773	814	772	635	612	635	612	814	772	808	766	814	772	813	771	813	771	634	611	813	771	634	611
7	735	-9	726	586	579	735	726	586	579	729	719	735	725	734	724	735	725	734	724	734	725	585	578	585	578
8	136	-16	120	134	118	127	114	125	112	136	119	134	117	135	118	135	118	134	118	126	113	132	116	124	111
9	46	-11	35	43	39	45	41	42	39	46	41	46	41	46	41	46	41	45	40	44	40	42	38	41	38

Table 3.8: Focal point analysis for the enthalpy of formation of the HCN dimer from two monomer units.

	RHF	MP2	CCSD	CCSD(T)	CCSDT	CCSDT(Q)	ΔE_e
DZ	−4.72	−0.78	+0.42	−0.10	+0.02	−0.01	[−5.18]
TZ	−4.21	−0.75	+0.29	−0.10	+0.01	−0.01	[−4.77]
QZ	−4.14	−0.75	+0.27	−0.11	[+0.01]	[−0.01]	[−4.73]
5Z	−4.11	−0.76	+0.26	−0.12	[+0.01]	[−0.01]	[−4.71]
6Z	−4.10	−0.77	+0.26	−0.12	[+0.01]	[−0.01]	[−4.72]
CBS LIMIT	[−4.10]	[−0.79]	[+0.27]	[−0.12]	[+0.01]	[−0.01]	[−4.74]

$$\Delta H_0 \text{ (AE-CCSDT(Q)/CBS)} = \Delta E_e\text{[AE-CCSDT(Q)/CBS]} + \Delta E_{\text{AZPVE}}\text{[VPT2/AE-CCSD(T)/cc-pCVQZ]} + \Delta_{\text{rel}}\text{[DPT2/AE-CCSD(T)/cc-pCVTZ]} + \Delta_{\text{DBOC}}\text{[RHF/cc-pCVTZ]} = -4.74 + 0.80 + 0.01 + 0.00 = \mathbf{-3.93} \text{ kcal mol}^{-1}$$

energy. This positive correction is expected due to the fact that the dimer contains additional inter-monomer vibrational modes not present in each individual monomer unit. By appending this correction we report a value that is more accurately described as an enthalpy of formation rather than a purely electronic energy. The other two corrections we use to refine our computations are of a smaller magnitude with only the relativistic correction from DPT2 appreciably affecting our results.

If we compare our results to those previously obtained via theory and experiment, we expect that our value of −3.93 kcal mol^{-1} to be highly reliable. A smaller (in absolute energy) value of −3.4 kcal mol^{-1} was reported Kofranek et al.[68] The enthalpy was computed at the HF level of theory using a custom double-zeta quality basis set. The ZPVE correction used was based upon harmonic vibrational frequencies computed with a smaller custom basis set.

The energy of the hydrogen bond of the dimer has been studied by King and co-workers[129] at the MP2/6-31G* level of theory. Utilizing this method, they report a bond energy of 4.96 kcal mol^{-1}. If we apply our AZPVE correction of 0.8 kcal mol^{-1} to their reported bond energy we obtain an enthalpy of bond formation of 4.16 kcal mol^{-1} which aligns reasonably well with the results of our focal point analysis.

Experimentally, Buxton and co-workers fit the binding of the dimer to a Leonard-Jones potential using their observed force constant for the intermolecular stretching mode and equilibrium monomer separation. Using the depth of their computed potential well, they report a binding energy of 4.4 kcal mol^{-1} for the dimer.[83] This too, shows fair agreement with our theoretical results. The latest value from Mihrin and coworkers[60] for the energy of dimer formation is a so-called "semi-experimental" result which uses the CCSD(T)-F12b/aug-cc-pV5Z association energy corrected by the zero-point vibrational energy of experimental frequencies. They also approximate the zero-point energy contributed by ν_6 and ν_7, for which gas-phase data is unavailable. They obtain a value of 4.11 kcal mol^{-1}. This is in decent agreement with our values which include both higher order coupled-cluster corrections and a purely theoretical zero-point vibrational energy correction which is 0.69 kcal mol^{-1} larger than their semi-experimental value.

3.4 Conclusion

We present here a comprehensive theoretical treatment of the HCN monomer, dimer and several isotopologues, many of which allow for direct experimental comparison. This high-level treatment performed at the CCSD(T)/cc-pCVQZ level of theory should provide excellent results for the dimer geometry. This is supported through the comparison of experimental rotational constants in Table I. Further investigation of the dimer geometry was done through the use of NRT as part of NBO analysis. The NBO method reveals the presence of charge transfer effects from the nitrogen lone pair of the proton acceptor monomer to the antibonding orbital of the proton donor C–H antibonding orbital. The effects of the transfer lead to the changes in monomer-like geometries discussed within the geometry section of the paper.

Further, the anharmonic frequencies obtained through VPT2 analysis were compared to existing experimental vibrational frequencies and found to be in good agreement with the existing gas-phase results. For the two modes where gas-phase data have not been reported, we discuss the effects of solid-argon matrices upon molecular vibration frequencies. Theoretical comparison was made between our results and those computed recently by Mihrin and coworkers.[60] With only subtle differences between the results for the harmonic frequencies computed in the two studies, it was suggested that the basis sets, in both cases quadruple-ζ quality, are near basis set saturation. Increasing basis set size will have only marginal effects on the theoretical frequencies. This makes our treatment of the anharmonicity in the molecule even more valuable as it represents fundamental frequencies with a large basis set for the system.

The vibrational section of the paper finished with a discussion of the effects of isotopic substitution on the vibrational frequencies. Several observed isotopic shifts were rationalized based on the isotopic effect upon the reduced mass of normal modes. At the end of the analysis, it was determined that the normal modes remained primarily monomer-like upon formation of the dimer.

The final section of the paper presents the enthalpy of formation of the hydrogen bond determined using the FPA. The FPA yielded an energy at the AE-CCSDT(Q)/CBS level of theory of 4.74 kcal mol^{-1}. After appending diagonal Born–Oppenheimer, relativistic and anharmonic ZPVE corrections to our focal point result, we report a value of 3.93 kcal mol^{-1} for the enthalpy of formation. This was compared to previous theoretical and experimental results and found to be in fair agreement..

Overall, this study represents the most comprehensive theoretical study of the HCN dimer system and provides a discussion of many different relevant molecular effects.

3.5 Supplementary Information

The cubic and quartic forcefields used for the VPT2 analysis within this paper can be found within the supplementary information found along with the published paper at the following doi:10.1002/cphc.201800728.

CHAPTER 4

STUDY OF SUBSTITUTION EFFECTS UPON ALUMINYL ANIONS AS CARBENE ANALOGS*

* P. R. Hoobler, N. Villegas-Escobar, J. M. Turney, and H.F. Schaefer, *to be submitted*

4.1 Abstract

In this study, we elucidate substituent effects upon the electronic structure of carbene-like aluminyl anions. These carbenoid species have been of recent synthetic interest and have been proposed as a pathway to hydrogen energy storage. We provide high level *ab initio* geometries and energies for both the methylene-like aluminyl anion species and several substituted derivatives, including amino-, hydroxy-, fluoro-, cyano-, isocyano-, and nitro-containing species. The geometries of each species is reported at the CCSD(T)/aug-cc-pV(T+d)Z level of theory. Energetic analysis of the formation of each of the substituted anions is reported as the result of two schemes. The first scheme is isodesmic in nature and inspired by recent findings within the literature. The second scheme is hypohomodesmotic in nature. The energies are further refined through the use of the focal point approach utilizing coupled cluster methods up to perturbative quadruples and basis sets through five-zeta quality. The relative energies reported from these schemes are compared to one another and existing literature. The efficacy of these schemes for determining the relative energies of forming the aluminyl anion species is discussed. Further insight into the geometries and energies is gained through the use of natural bond orbital (NBO) anlaysis at the B3LYP/aug-cc-pVDZ level of theory. It is concluded that electrostatic effects have a large impact upon geometries. Likewise, the ability of substituents to donate electrons into the empty p-orbital of aluminum has a sizeable impact upon the energies obtained from each scheme.

4.2 Introduction

Aluminyl anion compounds are carbenoids in that they are divalent with six valence electrons. Often described as low-valent, aluminum (I),[130–139] compounds, this class of molecules has been an interest to the chemistry community for quite sometime. Carbenes have a long rich history in both theory and experiment(cite Schaefer and experiment) due to their unique electronic structure and resultant reactivity. Aluminum (I) compounds have been synthesized for some time[130,131] but the earliest compounds were tetrameric (Al_4X_4) and non-carbenoid. The carbenoid compounds of aluminum (I) were not realized until recently.[136] The first aluminyl carbenoid species was synthesized in 2000 by Roesky and co-workers. This synthesis of the monomeric carbenoid, $[HC(CMeNAr)_2Al]$[136] was achieved through the use of a very bulky bi-dentate ligand which formed two Al–N bonds.

The synthesis of nucleophilic aluminyl anion, coordinated with potassium ions has renewed the interest in this group of compounds. These systems are also known to be significant σ donors which have been theoretically predicted to have the ability to break H–H bonds and form hydrogenated species.[140–146] These hydrogenated species then may be utilized as a catalyst for further reaction,[147–149] or as a form of hydrogen

storage for use within energy production.[150,151] If realized, this form of hydrogen storage could have a significant impact upon the energy industry. In light of this, it behooves us to gain a greater understanding of these compounds.

A number of theoretical studies have been undertaken on the arduengo-type aluminyl carbenoids in light of periodic trends. A paper by Metzler-Nolte[152] does an analysis of the boryl and aluminyl analogs of the simplest arduengo-type carbene. This was added to later by Sundermann, Reiher, and Schoeller who additionally treated the gallium and indium species.[153] Within their study, geometries were obtained at the B3/6-31G++g(d,p) level of theory, utilizing relativistic effective core potentials for the larger elements within the series. Their study focused primarily on determining the electron affinity of each of the species, which they approximated as the difference between singlet/triplet carbene-like electron configurations and the lowest lying doublet. In general, the electron affinity increased going down the periodic table. They attribute this to the fact that larger elements within the group were able to donate the electron to the neighboring electronegative nitrogen atoms. This charge delocalization allows for energetic lowering of the group 13 anions, or an increase in the electron affinity of the neutral doublet. Another interesting finding within the study was the fact that the bonding between the group 13 metal and the neighboring nitrogens became significantly more ionic in character going from boron to aluminum. Another study in 2007 by Tuononen and coworkers[154] extended the same analysis to neutral group 14, cations of group 15 and dications of group 16 in addition to the group 13 carbene analogs. Their conclusions, obtained through natural bond orbital analysis, agree that the bonding between aluminum and the nitrogen ligand were primarily ionic in nature.

Although larger species resembling n-heterocyclic carbenes are now in synthetic use and have been of interest for some time, the amount of literature on simple carbenoids within the aluminyl anion family is lacking. With the recent spectroscopic observation of a simple aminocarbene within an argon matrix,[155] it is possible that more interest will be given to these simple systems which represent an outstanding opportunity for collaboration between theory and experiment. Quantum chemistry has the ability to look at electronic structure effects on geometries, vibrational frequencies, and energies of these simple carbenoid structures. There is a rich history of theory being used to study carbenes.[59] With proper analysis, species which are more energetically favored over others may also be predicted, giving guidance to experimentalists looking to observe these previously unstudied species spectroscopically.

When computing energies of chemical processes, often there is a large separation between the magnitude of the total energies (large and of no experimental interest) and the energy of processes (relatively small and of great interest). Modest errors in the total energies computed for a system can even have qualitative effects upon the interpretation of results. This makes obtaining reactions energies directly of large systems to chemical or even sub-chemical accuracy ($\leq$1 kcal mol^{-1}) possible only with the most expensive methods,

which are not viable for many systems of chemical interest. A way to reduce the effect of these errors on results is to devise a scheme in which errors within similar systems cancel out. One way to achieve this error cancellation is to ensure that the types of bonds on each side of a model reaction are as similar as possible. In theory then, all bonds of the same type should incur some systematic error due to the method used. When total energies are subtracted, these errors cancel out leaving less error in the result. The derivation of schemes is not all that straight forward, and thus several different schemes have been developed. For a quality review of different schemes, we recommend the papers by Wheeler and co-workers.[156,157] Within this study, we discuss the use of both the isodesmic and hypohomodesmotic schemes to model the energy of formation of each carbenoid, each with their own strengths. The goal is to determine with these small, fundamentally "simple" systems, the efficacy of these schemes in studying carbenoid structures.

Isodesmic reaction schemes[158,159] are those that preserve the number of each type of bond. In terms of hydrocarbons, for which these types of analyses were initially developed, an isodesmic reaction has the same number of C–H, C–C, C=C, and C≡C bonds within the reactants and products. This allows for some error cancellation between similar bonds. The more strictly defined hypohomodesmotic reaction takes the isodesmic methodology a step further. Not only does the number of each type of bond stay the same, but the hybridization of each central bonding atom must be the same as well. This recognizes that the bonding environment inside sp^3, sp^2, and other hybrid orbitals are inherently different. If these differences are not accounted for in an energetic scheme, desired cancellation of error does not occur as nicely and direct comparison of energies is not as easily accomplished. Wheeler and co-workers[156] developed a hierarchy even within the definition of homodesomotic that they used to analyze different reactions involving hydrocarbons. In light of these definitions, we propose to use two different schemes in order to compare the energetic effects of different aluminyl anion substituents as directly as possible.

The first scheme can be found in the study by Schreiner and Eckhardt,[155] they proposed an isodesmic scheme for comparison of heterocarbenes. Modeled after theirs, we intend to do the following:

$$\ddot{\mathrm{A}}\mathrm{lH}_2^- + [R_1 - \mathrm{AlH}_2 - R_2]^- \rightarrow \mathrm{AlH}_4^- + [R_1 - \ddot{\mathrm{A}}\mathrm{l} - R_2]^- \tag{4.1}$$

This scheme preserves the number of each bond-type all of which are single bonds between aluminum and hydrogen or aluminum and the two substituents (R_1 and R_2) one of which may also be a hydrogen. The shortcoming of this technique is that it does not preserve the orbital hybridization across the aluminum species. This is because the ground state of the carbene like structure is a singlet that is largely sp^2 hybridized while the aluminum that is tetravalent in each case is sp^3 hybridized. This changing of hybridization may itself affect the energy of Al-R_x bonds causing confusion when it comes to direct comparison as some substituents

may feel the effect of the change in hybridization more than others. The energetic difference then does not result purely as a result of the breaking and forming of bonds.

The second scheme seeks to complement the first by using only sp^2 hybridized aluminum atoms. Because aluminum is naturally trivalent, we can change our scheme to the following:

$$\ddot{\mathrm{A}}\mathrm{lH}_2^- + [R_1 - \mathrm{AlH} - R_2] \rightarrow \mathrm{AlH}_3 + [R_1 - \ddot{\mathrm{A}}\mathrm{l} - R_2]^- \tag{4.2}$$

In this way, we avoid the changing of hybridization on each of the central aluminums. The reaction energy should benefit from as much cancellation of error as possible. However, an astute chemist may also point out that we are now undergoing a shift in charge between an anion and a neutral species.

Although both schemes have potential shortcomings, they are both worthy of consideration. It may even be that they are both useful in different situations.

We will also compare these schemes to reactions in which we displace hydrogen or hydride with the neutral substituent(s) or anion substituent(s) respectively. We call these schemes the neutral replacement scheme and the anionic replacement scheme.

Results for direct comparison of the isodesmic results are available from the 2007 paper by Tuononen and coworkers. They predicted the hydrogenation energy of the methylene derivative to be exothermic by 11 kcal mol^{-1}. They also predicted, with an isodesmic scheme, that the hydrogenation of the arduengo type carbene analog is energetically unfavored by roughly 200 kcal mol^{-1} compared to the methylene analog.[154] They attributed this large energetic difference to the loss of π delocalization between the p-block atom and neighboring nitrogens as a result of hydrogenation.

The numbers obtained from these two schemes, although not meaningful in and of themselves, provide a chance to develop an appropriate scheme for the handling of these carbenoid species. Ideally, the best of these schemes may be applied to larger aluminyl anion species which are being developed synthetically.

4.3 Theoretical Methods

The geometry for each species was obtained at the coupled cluster level of theory including single, double, and perturbative triple excitations [CCSD(T)] using the augmented correlation-consistent triple-ζ quality basis set of Dunning[17] labeled CCSD(T)/aug-cc-pVTZ. The augmented functions were included to account for the fact that the majority of our species are anions which require diffuse functions to properly model the larger electron cloud. In addition to augmentation functions, specific functions were added to the basis sets used for aluminum to explicitly describe 3d-like contributions to the electronic structure of the species studied.[160] These functions, referred to as tight-d functions have been found to be necessary to allow for

Figure 4.1: Simple structures of the different species discussed. Species A is the simplest Arduengo-type carbene. Species B is the simplest carbenoid structure. Species C is the basic structure for the hypohomodesmotic energy scheme. Species D is the basic structure for the isodesmic energy scheme.

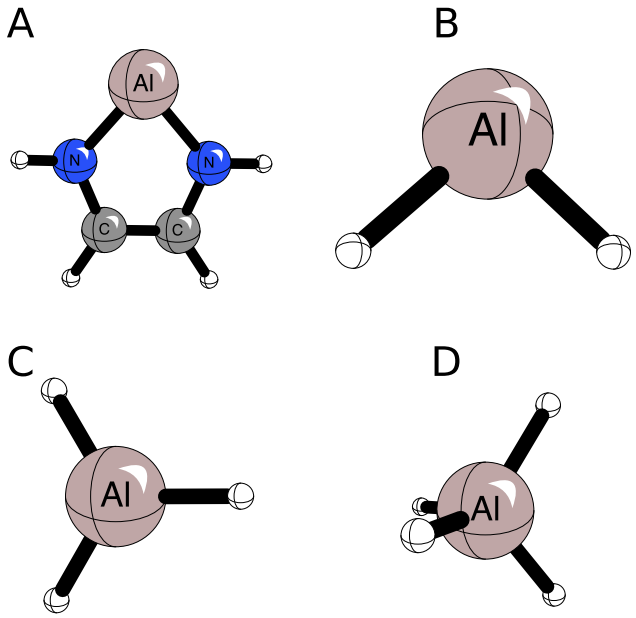

smooth convergence of relative energies, particularly when extrapolated to the complete basis set limit for species containing period 4 elements and beyond.[161] The geometries were tightly converged upon the minimum of the potential energy surface. The gradients were converged in each case to RMS $\leq 10^{-9}$. To confirm that each of these species is a true minimum on the potential energy surface, we performed harmonic vibrational frequency analysis to confirm that the frequencies are positive.

Focal point analysis[14–16,117] (FPA) was used to obtain energies that are highly converged with respect to both correlation and basis set. Single point energies were computed at the coupled cluster level including single, double, triple, and perturbative quadruple excitations [CCSDT(Q)]. The correlation-consistent basis sets of Dunning including augmented functions, up through five-ζ quality (aug-cc-pVXZ, X=D,T,Q,5), including tight-d functions for the aluminum, were used to approach the basis set limit. Extrapolations to the complete basis set were performed for Hartree–Fock energies using the three-point scheme of Feller[18]:

$$E_{\mathrm{HF}}(X) = E_{\mathrm{HF}}^{\infty} + ae^{-bX} \tag{4.3}$$

These extrapolations were performed with the results utilizing basis sets of TZ, QZ and 5Z quality. The extrapolations for each correlated method were performed using Helgaker's two-point extrapolation scheme [19]:

$$E_{corr}(X) = E_{corr}^{\infty} + aX^{-3} \tag{4.4}$$

These extrapolations were performed with the results utilizing basis sets of TZ and QZ quality. The electronic energy was further refined by an additive correction at the CCSDT(Q)/aug-cc-pVDZ level of theory. The computations through perturbative triples were run using the ECC module of CFOUR where the additive perturbative quadruples correction was run using the NCC coupled cluster module by Matthews. [162] The result in each case is then an electronic energy that is considered to be of coupled cluster through perturbative quadruple excitations at the complete basis set quality [CCSDT(Q)/CBS]. All energetic computations were computed within CFOUR.

Rationale for the observed geometries and energies was gained through the use of natural bond orbital theory (NBO) [113] including the use of natural resonance theory (NRT). [114–116] These computations were done with the NBO 5.0 program as interfaced with Q-Chem [163] at the B3LYP/aug-cc-pVDZ level of theory.

4.4 Results

4.4.1 Geometries

Aluminyl Anions

These species mimic the valence electronic structure of carbenes. We only consider the singlet state of each aluminyl anion species as the triplets are expected to be much higher in energy. The geometrical parameters that are relevant to each species are reported in Table 4.1. In order to study different bonding effects, the methylene derivative (R1 = R2 = H) is used as a baseline with deviations from those geometrical parameters, in particular the R1-Al-R2 bond angle, being of interest. What we can see is that we can divide our species into two particular groups, one of strong π donors (hydroxy, amino and fluoro aluminyl anions) and one of weakly π donating (cyano, isocyano, and nitro anions). For those substituents that are π donating, the bond order between the substituent and the aluminum increases and thus contracts. A good comparison to observe this trend is the difference in the bond angles for the amino species and the isocyano species.

The bond angle within the monoamino species is nearly the same as in the methylene derivative. According to the NBO results, both the hydrogen as well as the amino nitrogen carry negative charge. The resulting bond angle is the result of balancing out the repelling negative charges of the nitrogen and hydrogen while maximizing positive interaction with the positive charge on the aluminum. Within the diamino species, we

see an increase in the bonding angle, now between two nitrogens bound to the central aluminum. These nitrogens are more negatively charged than the nitrogen in the monoamino species, with natural charges of –1.518 and –1.486 respectively. This causes a greater interaction strength between the nitrogens and aluminum, but also causes repulsion between the two very negatively charged nitrogens within the diamino case.

Contrasting that case with the isocyano, it can be seen that the isocyano species have a smaller inter-substituent bond angle than methylene. The same forces at work in the amino case are at work here. The first thing to notice is the much longer Al–N bonds that are present in the isocyano case. This is due to the fact that there is much less significant donation from the isocyano compared to the amino group. This means that the bond is weaker and thus elongated. It is also worth noting that the magnitude of the natural charge on the nitrogen is smaller in magnitude in the isocyano species (–0.943 and –0.971 in the mono- and disubstituted species respectively. A repulsion argument can again be used. The bond angle becomes smaller as the attractive forces of bonding to the aluminum and repulsion of negative natural charges on the nitrogens even out. Ultimately these arguments are sufficient to explain the trends observed in most of the species.

Table 4.1: Geometries of simple singlet aluminyl anion species (R1–Al–R2) computed at the CCSD(T)/aug-cc-pV(T+d)Z level of theory (tight d-functions on aluminum). All bond lengths given in angstrom (Å) and all bond lengths in degrees.

R1	R2	∠R1–Al–R2	r(Al–R1)	r(Al–R2)
H	H	95.2	1.689	1.689
H	OH(syn)	97.1	1.728	1.799
H	OH(anti)	98.4	1.692	1.795
OH(in)	OH(in)	103.9	1.797	1.797
OH(in)	OH(out)	99.5	1.799	1.784
OH(out)	OH(out)	101.2	1.782	1782
H	NH_2	96.0	1.700	1.859
NH_2	NH_2	99.4	1.860	1.860
H	CN	92.1	1.673	2.093
CN	CN	92.0	2.074	2.074
H	NC	93.2	1.678	1.969
NC	NC	93.0	1.948	1.948
H	F	98.6	1.711	1.734
F	F	102.0	1.727	1.727

A look at the dihydroxy species will give some interesting insight into other effects present within these species. The in-in dyhydroxy species suffers from steric repulsion between the hydrogens which are pointed at one another in the plane. This steric repulsion causes the bond angle between the hydroxy substituents to widen, resulting in the largest bond angle reported in Table 4.1. The in-out dihydroxy species has a significantly smaller bond angle than the other two dihydroxy species. One of two things is causing this.

First, the oxygen-aluminum bond lengths are mismatched, meaning that the intersubstituent bond angle decreases further than the in-in conformer before repulsion effects between the negatively charged oxygens takes effect. The other effect that could be occurring would be an attractive force between the positively charged "in" hydrogen and the negatively charged "out" oxygen. This attractive force would pull the two substituents together, decreasing the bond angle between them. The out-out conformer undergoes the same type of forces as that of the amino species. Contracted bond lengths due to increase π interaction of the lone pairs of oxygen and the empty p-orbital of alumium strengthen and shorten the alumium oxygen bond and the bond angle between oxygen atoms then increases.

Trivalent aluminyl species

The species for the hypohomodesmotic energy scheme are derived from the neutral AlH_3 molecule. The reference molecule is of D_{3h} symmetry. As such the bond angles are seen as deviating from the "ideal" of 120°. The common geometrical parameters found in each of these species are listed in Table 4.2. In essence, one could look at these geometries as the addition of a proton (H^+) to each of the aluminyl anion species. This results in a structure where the lone pair of the aluminum atom serves to form an aluminum-hydrogen bond. Because the hybridization of the aluminum atom does not change, the geometries remain planar and markedly similar to the aluminyl anion species. The intersubstituent angles become much larger in these structures. The reason for this being that the lone pair that was previously on the aluminum has become a bonding pair with a the proton. The lone pair was in the HOMO of the anion species and was markedly diffuse. This diffuse negative charge forced the other bonding pairs closer together. The electrons now occupying a much less diffuse bonding orbital allow the intersubstituent angle to increase. Still some interesting effects are observed within these geometries that can be traced through NBO analysis. The structures for each of these species can be found in Figure 4.3.

A first observation is the ubiquitous contraction of the aluminum-containing bonds compared to the carbenoid species. These contractions are roughly 0.01 Åin every case which is very significant. In investigating the reason for this contraction, one will find that the AlH_3 molecule is known to be a "magic cluster" [164] whereby the ratio of aluminum to hydrogen has a particularly favorable impact on the electronic structure. Some work has been done on larger clusters of aluminum and hydrogen to develop rules for this "magic" effect [165] but their equations do not apply to such a small cluster. Typically, these magic clusters come about because of a closed subshell of orbitals, resulting in strong bonds and good separation between bonding orbitals and anti-bonding orbitals. In the case of the purely hydrogentated species in this paper, we find that the greatest HOMO-LUMO gap exists for the AlH_3 species. We report these results, along with the Al–H stretching frequencies for all three species in Table 4.3. It can be seen that the HOMO-LUMO gap of 12.1 eV

Table 4.2: Geometries for the hypohomodesmotic analysis of the type R1–AlH–R2 computed at the CCSD(T)/aug-cc-pV(T+d)Z (tight d-functions on Al) level of theory. All bond lengths given in angstrom (Å) and all bond lengths in degrees.

R1	R2	∠R1–Al–R2	r(Al–R1)	r(Al–R2)	r(Al–H)
H	H	120.0	1.582	1.582	1.582
H	OH	120.1	1.580	1.705	1.573
OH(in)	OH(in)	124.4	1.700	1.700	1.562
OH(in)	OH(out)	118.4	1.702	1.697	1.568
OH(out)	OH(out)	118.8	1.698	1.698	1.574
H	NH_2	117.8	1.580	1.776	1.580
NH_2	NH_2	119.9	1.778	1.778	1.577
H	CN	117.1	1.569	1.947	1.569
CN	CN	115.1	1.929	1.929	1.558
H	NC	116.7	1.568	1.818	1.568
NC	NC	115.2	1.798	1.798	1.554
H	F	117.2	1.572	1.655	1.572
F	F	117.7	1.645	1.645	1.556

Table 4.3: Comparison of the HOMO-LUMO gaps, the Al–H stretching frequencies and Al–H bond lengths in the different substituted carbenoids, alane derivatives and AlH_4^- derivatives.

	$\ddot{A}lH_2^-$			AlH_3			AlH_4^-		
Substituent	Al–H	ω_{Al-H}	$\Delta E_{HOMO-LUMO}$	Al–H	ω_{Al-H}	$\Delta E_{HOMO-LUMO}$	Al–H	ω_{Al-H}	$\Delta E_{HOMO-LUMO}$
H	1.689	1492	4.44	1.582	1937	12.14	1.645	1729	8.57
OH(syn)	1.728	1342	4.67	1.580	1939	12.34	1.637	1718	8.24
OH(anti)	1.692	1457	4.45	1.573	1969	12.34	-	-	-
NH_2	1.699	1437	4.33	1.580	1946	11.66	1.656	1706	7.79
CN	1.674	1552	5.38	1.569	1998	12.34	1.623	1783	9.39
NC	1.681	1526	5.21	1.568	2002	12.52	1.623	1787	9.16
F	1.709	1392	4.71	1.572	1980	12.59	1.640	1733	8.62

is much higher than the other two species and the accompanying Al–H stretching frequency is much larger. This is expected as it is known that aluminum prefers to form trivalent compounds. It is worth considering how this might affect the results of the hypohomodesmotic reaction scheme. It is informative to look at how substitution affects these values in light of the fact that they are very telling of electronic structure affects of substitution. Values for all singly-substituted species can be found in Table 4.3.

Within the dihydroxy family of structures we again see that the "in" structure has the largest ∠OAlO. This is again attributed to the steric repulsion of the hydrogen atoms pointed directly at one another. Likewise the same reason is to blame for the expansion of the ∠NAlN in the diamino molecule. The steric repulsion of the in plane hydrogens forces the two substituents apart.

Electrostatic repulsion plays a decisive role in the $\angle R_1AlR_2$ reported in Table 4.2. Substituents such as cyano and isocyano groups are able to form smaller bond angles than hydrogen because they form longer bonds with the central aluminum atom. These longer bonds allow smaller bond angles without repulsion

forces dominating. Also, these groups are not bulky like the amino groups meaning that steric repulsion further away from the central atom does not largely affect the intersubstituent bond angle.

Tetravalent aluminyl species

The species for the isodesmic energy scheme are derivative of alumanuide (AlH_4^-). This species is tetrahedral, like methane. The bond angles within alumanuide start at the tetrahedral angle ($\approx 109.57°$). The structures are inherently different within this group of molecules because the hybridization of the central aluminum atom has changed from sp^2 to sp^3. There is no longer an empty p-orbital on the central aluminum which means that the π donation energy lowering is no longer available. This has an effect of breaking the amino subsituents out of planarity. The amino species now have an sp_3 hybridized central nitrogen atom. The loss of π donation also has a significant effect on the energies of the amino species which will be discussed below.

As in the case of the hypohomodesmotic structuree, there is a contraction of Al–H bonds compared to the carbenoid derivative. Looking at the information in Table 4.3 you can see that these structures lie in the middle between the two sets of HOMO-LUMO gaps. If this lowering of the HOMO relative to the LUMO prevents as much population in anti-bonding orbitals, it is no surprise to see that bonds are contracting.

Because the hybridization has changed, we see that the planarity of the diamino and dihydroxy groups has been eliminated. This has distinct effects upon the electronic structure and resulting energies that we will discuss later. One other effect that this causes is that we now have to consider three separate structures for the diamino species. We have maintained the naming system that was used for the dihydroxy structures to avoid confusion. The structures considered here however, do have symmetry. When both amnio groups are pointed either in or out, the symmetry of the structure is C_2v whereas the in-out structure is of C_s symmetry. Of the three structures considered however, the out-out structure proves to not be a minimum on the potential energy surface. Analysis of the vibrational frequencies shows one imaginary mode, a symmetry breaking twisting mode. This mode arises from the fact that the two lone pairs of the amino groups are pointed directly at one another. The in-in and the in-out conformers do not suffer from this repulsion interaction and so they are found to be minima.

For similar reasons, the dihydroxy family within the tetravalent species are not minima in any of the symmetric conformations (in-in, in-out, out-out) that were minima within the hypohomodesmotic scheme. This is likely due repulsive forces that exist when the hydrogens point toward either each other or toward the other oxygen. The hybridization of the central aluminum atom forces the bond angles in these structures to be much tighter. This forces the O–H bonds out of planarity with each other and into a twisted structure possessing C_2 symmetry.

Table 4.4: Geomtries for the isodesmic analysis of the type R1–AlH_2–R2 computed at the CCSD(T)/aug-cc-pV(T+d)Z (tight d-functions on Al) level of theory. All bond lengths given in angstrom (Å) and all bond angles in degrees.

R1	R2	∠ R1–Al–R2	∠ H–Al–H	r(Al–R1)	r(Al–R2)	r(Al–H)
H	H	109.5	109.5	1.645	1.645	1.645
H	OH	106.9	107.9	1.637	1.794	1.650
OH(twist)	OH(twist)	111.5	113.5	1.789	1.789	1.639
H	NH_2	107.4	108.2	1.656	1.887	1.644
NH_2 (in)	NH_2 (in)	118.2	117.5	1.888	1.888	1.641
H	CN	106.5	112.3	1.623	2.043	1.623
CN	CN	105.5	115.6	2.019	2.019	1.605
H	NC	106.5	112.3	1.623	1.927	1.623
NC	NC	104.8	116.1	1.897	1.897	1.603
H	F	108.6	110.3	1.640	1.725	1.640
F	F	108.2	113.0	1.714	1.714	1.360

Empty p-orbital donation

As with aminocarbene[155], we see that all of the amino complexes adopt planar structures which permits the lone pairs to be in resonance with the empty p-orbital of the aluminum atom within the singlet structure. This is also supported by the NBO results obtained for these species. In both the divalent and trivalent aminoaluminyl species their is a large second-order energy within the NBO analysis. These are listed in Table 4.6. It can be seen that the hydroxyaluminyl anions also have a sizable donation energy into the empty p-orbital of the aluminum. However, by the smaller value obtained from the NBO analysis, it can be seen that this effect is much less pronounced than in the aminoaluminyl species. The comparison with fluroaluminyl anions shows that these compounds have less donation from the fluorine lone pair into the empty p-orbital of aluminum than the corresponding amino and hydroxy species. This is most likely due to the high electronegativity of fluorine which makes it much less likely to donate electrons to a neighboring atoms.

4.4.2 Energetics

Isodesmic Reaction Energies

In this section, we compare the results from modeling the isodesmic reaction scheme found in equation 4.1. These results can be found in Table 4.6. These results have the advantage that they all of the species within the scheme carry a negative charge. The effect of the natural diffuseness of the electron cloud in each of these ions should cancel out allowing us to examine the effect of breaking and forming bonds (or lone pairs) within a similarly charged electron environment.

The greatest energetically favored species in the case of the Isodesmic reaction scheme show general agreement with the results of Eckhardt and Schreiner[155], in that the amino and hydroxy groups have the lowest focal pointed reaction energy. The lowest focal pointed energy belonged to the twist conformation of the dihydroxy species with an isodesmic reaction energy of -15.83 kcal mol^{-1}. The diamino (in-in) is nearly isoenergetic within the scheme with an energy of -15.40 kcal mol^{-1}. Although these results agree qualitatively with those of the Schreiner study, the values we get for the energies of reaction are much smaller. For the diamino case, they report a stabilization enthalpy of -91.2 kcal mol^{-1}. The values obtained for the aluminyl anion case are approximately 5.5 times smaller than those for the carbene case. Although the levels of theory (B3LYP and FPA) for the two sets of results differ, a difference this large must be due to a chemical reason. One possible cause is that there is a large difference in the energy gaps between the carbene species ($\ddot{C}H_2$ and $\ddot{A}lH_2^-$ and the methane species (CH_4 and AlH_4^-). The energy of this transformation is what needs to be overcome by the substituted analogs in order for the reaction scheme to give a negative energy. If the AlH_4^- species has a lower relative energy compared to the carbene than methane does to methylene, our results would have energies much closer to zero.

There is a definite separation between the energies observed for those species with possible unhybridized p-orbitals and those without. The highest reaction energies were obtained for the cyano and isocyano species, who have no possibility of having an unhybridized p-orbital on the atom bound to the aluminum. Again a consideration needs to be made as to what is gained as the substituted reactant forms the substituted carbenoid product. Those with empty p-orbitals go from an sp^3 hybridized center to an sp^2 hybridized center allowing for an energy lowering interaction that was completely unavailable before. The mere sigma donating substituents do not gain from this energetic stabilization. This perhaps means that this scheme is biased toward species which have possibly unhybridized p-orbitals. It behooves us in this case to try to balance out this energetic effect using a scheme that maintains the hybridization of aluminum so that an entire category of energetic interactions does not appear on only one side of the model reaction.

Hypohomodesmotic Reaction Energies

In this section, we compare the results from modeling the aluminyl anion formation energy within the hypohomodesmotic reaction scheme found in equation 2. These results benefit from the fact that the hybridization of the central aluminum atoms remains constant throughout the entire reaction. The bonds broken and formed should be directly comparable as they are formed by the most similar of orbitals. The results can be found in Table 4.6. Looking at the convergence of the focal point tables within this scheme, it can be seen that the energies within our scheme are well converged. The incremented focal point tables show that most of the energies have corrections of less than chemical accuracy (1 kcal mol^{-1}) at CCSD(T)

and all are converged to that level at CCSDT. Upon observation of the energies obtained by the scheme, the results are surprising. Given nitrogen's propensity to donate to the π system of molecules, the planar mono- and diamino anions should show a significant energetic favorability. Also in question are the results for the mono-and dihydroxy, and the monofluoro anions. The mono-hydroxy carbenes are nearly isoenergetic within the scheme and the dihydroxy carbenes show a marked improvement but are favored energetically on a much lower scale than the cyano, isocyano and nitro anions. Our hypohomodesomotic rankings do not agree with the results of Schreiner's isodesmic scheme.[155] Where their results favor the amino and hydroxy carbenes, our hypohomodesmotic scheme shows these aluminyl anions to be the least energetically favored.

NBO analysis can be used to shed some light on this most interesting disagreement. Ultimately, it points to a potential pitfall of this scheme in that the strongest π donating species benefit from extra energetic lowering upon the addition of the proton. The proton, being more electronegative than the aluminum actually draws electrons away from the aluminum, making it increase in positive charge more than the charge of a single electron. This leaves the aluminum able to accept additional electron density. In the case where the neighboring atom contains at least one lone pair (N, O, and F), this causes a significant increase in the donation of electrons to the empty p-orbital of the aluminum. In the mono-substituted anions, one can see this increase in donation to the empty p-orbital through the NBO results.

The case of amino carbenes is so severe, that additional bonds are formed according to the NBO analysis. Within the NBO results for the monoamino anion, there is no donation into the empty p-orbital from the lone pair on the nitrogen. This is because formally, there is a double bond formed between these two centers. Although this formal double bond is formed in both the anion and once a proton is added, the energy of the double bond NBO's decreases significantly. This decrease in the energy of the bonding orbitals causes and energetic lowering of the reactant side of our scheme. This in turn causes the interesting results observed for the schemes within the energy. For the diamino case, the trivalent aluminum complex forms a 3-center, 4-electron "hyberbond" which is not present within the diamino anion. This "hyperbond" essentially shows the degree to which π delocalization occurs within this species. Again this energetic lowering of the products results in a positive energy within the hypohomodesmotic scheme. Although interesting, the near equal energies between the mono- and diamino energies appears to be merely coincidental.

In the evaluation of the hypohomodesmotic scheme for determining comparable energies for the system at hand, perhaps more work needs to be done. Although it is true that the scheme does not appear to treat the amino, hydroxy, and fluoro species consistently with the weakly π donating species, it may still be useful for determining relative stability of either strong or weak π donating species. It appears that the cyano, isocyano and nitro species are able to be compared directly as they all give energies that are somewhat similar. Particularly encouraging within the cyano results is that dicyano energy is roughly twice

Table 4.5: A comparison of the energies (in kcal mol^{-1}) obtained from the hypohomodesmotic, isodesmic, direct-anion, and direct-neutral energy schemes obtained through Focal Point Analysis. Complete focal point results can be found in Tables 4.7 – 4.50.

Species	Isodesmic	Hypohomodesmotic	Anion Replacement	Neutral Replacement
OH	−6.61	−0.70	−22.00	−47.38
$(OH)_2$	−15.83	−7.78	−48.95	−99.70
NH_2	−8.99	+3.68	−22.48	−22.66
$(NH_2)_2$	−15.40	+3.71	−45.03	−45.40
CN	−0.81	−20.38	+15.20	−56.40
$(CN)_2$	−2.31	−40.43	+33.99	−109.20
NC	−1.18	−18.34	+15.95	−55.64
$(NC)_2$	−4.60	−38.87	+32.58	−110.60
F	−3.16	−5.37	−17.85	−80.03
F_2	−10.92	−19.48	−43.71	−168.07

the magnitude of the monocyano species. In the case of weakly π donating species, it appears to treat different species consistently. However, it is not recommended to use this scheme where the species span a wide range of π donating ability, thereby limiting its scope. An area of further study would be to test this scheme upon a set of molecules containing only Arduengo type aluminyl anions. These species contain aromatic stabilization by inclusion of the empty p-orbital which is an extreme version of π donation. It is possible that this scheme is able to treat a collection of only these types of species with consistency.

Comparison to Replacement Energetic Analyses

In Table 4.5, we have reported the focal-point energies for the two energetic schemes studied in this paper with the computation of the energy of formation of each aluminyl anion species as replacements of hydrogen and hydride with the substituent species. One can see that the reaction energies vary considerably between schemes used. The individual performances by substituent groups can vary in the relative order as well. Take for example the dicyano species. In the anion replacement computations, the dicyano species shows the least favorable energy, with products predicted to be less stable than the reactants by nearly 34 kcal mol^{-1}. However, in the neutral replacement computations, we see that it is favored by over 100 kcal mol^{-1}. This apparent discrepancy points out the inherent bias that is present in these replacement schemes, related to the electron affinity of the bare substituents. In the cyano family of species, has a large electron affinity. The neutral radical species as it replaces the hydrogen atom, takes on a large amount of electron density. In the case of the anion replacing hydride, the cyano group is forced to donate electron density in order to form a bond to the aluminum. This can be seen in the natural charges on each atom in the neutral and anionic substituents with the natural populations in the cyanoaluminyl anion. The charge on the nitrogen, as the most electronegative atom, is quite telling in this case. The charge on the nitrogen is −0.423 in the neutral

Table 4.6: The E(2) energies from the natural bond orbital analysis donation into the lone pair and final CCSDT(Q)/CBS energies (in kcal mol^{-1}) from energy schemes

R1	R2	Carbene-Derivative	Hypohomodesmotic	Hypo en
H	OH(syn)	14.05	19.79	−0.14
H	OH(anti)	14.35	19.79	−0.70
OH(in)	OH(in)	11.37	17.42	−5.20
OH(in)	OH(out)	11.48,12.28	17.38,17.69	−7.21
OH(out)	OH(out)	12.33	17.61	−7.78
H	NH_2	–	–	+3.68
NH_2	NH_2	15.29	17.78	+3.71
H	F	10.62	15.41	−5.37
F	F	9.12	13.73	−19.48
H	CN	2.09	4.69	−20.38
CN	CN	2.06	4.88	−40.43
H	NC	3.30	7.50	−18.34
NC	NC	2.95	7.48	−38.87
H	NO_2	–	–	−32.63

substituent, −0.787 in the anionic subsitutent, and −0.543 in the cyanoaluminyl anion species. The shift is even more exaggerated in the dicyano case where the natural charge on each nitrogen is −0.502, which is almost the same as in the neutral. This shift in the electron density either toward the nitrogen (in the case of the neutral replacement) or away from the nitrogen (in the case of the anion replacement) explains the large shift in both the cyano and isocyano families.

The hydroxy-, amino- and fluoro-substituted species see the opposite effect occuring. These species are the most energetically lowered by formation of bonds between anionic versions and have the greatest negative energies for the anionic replacement calculations. This is again because of the electron density that is donated between these species and the empty p-orbital on the aluminum. This is why a stark contrast between these species and the cyano- and isocyanoaluminyl anions within the anion replacement energy scheme. Although these atoms are highly electronegative, they are able to take advantage of greater bonding within the carbenoid structures than the cyano and isocyano species.

4.5 Conclusion

We have shown that the geometries of all three types (carbenoid, AlH_3-like and AlH_4^--like can be explained through simple bonding concepts such as electrostatics, sterics and orbital occupations.

The isodesmic and hypohomodesmotic schemes used to determine the relative formation energies of the different carbenoid species were evaluated using focal point analysis. The isodesmic scheme largely favored the strongly π donating species. This is due to the fact that the tetravalent species could not possibly benefit from a delocalized π system because of hybridization. This large change in the bonding structure

Figure 4.2: Geometries of the carbenoid aluminyl anion species

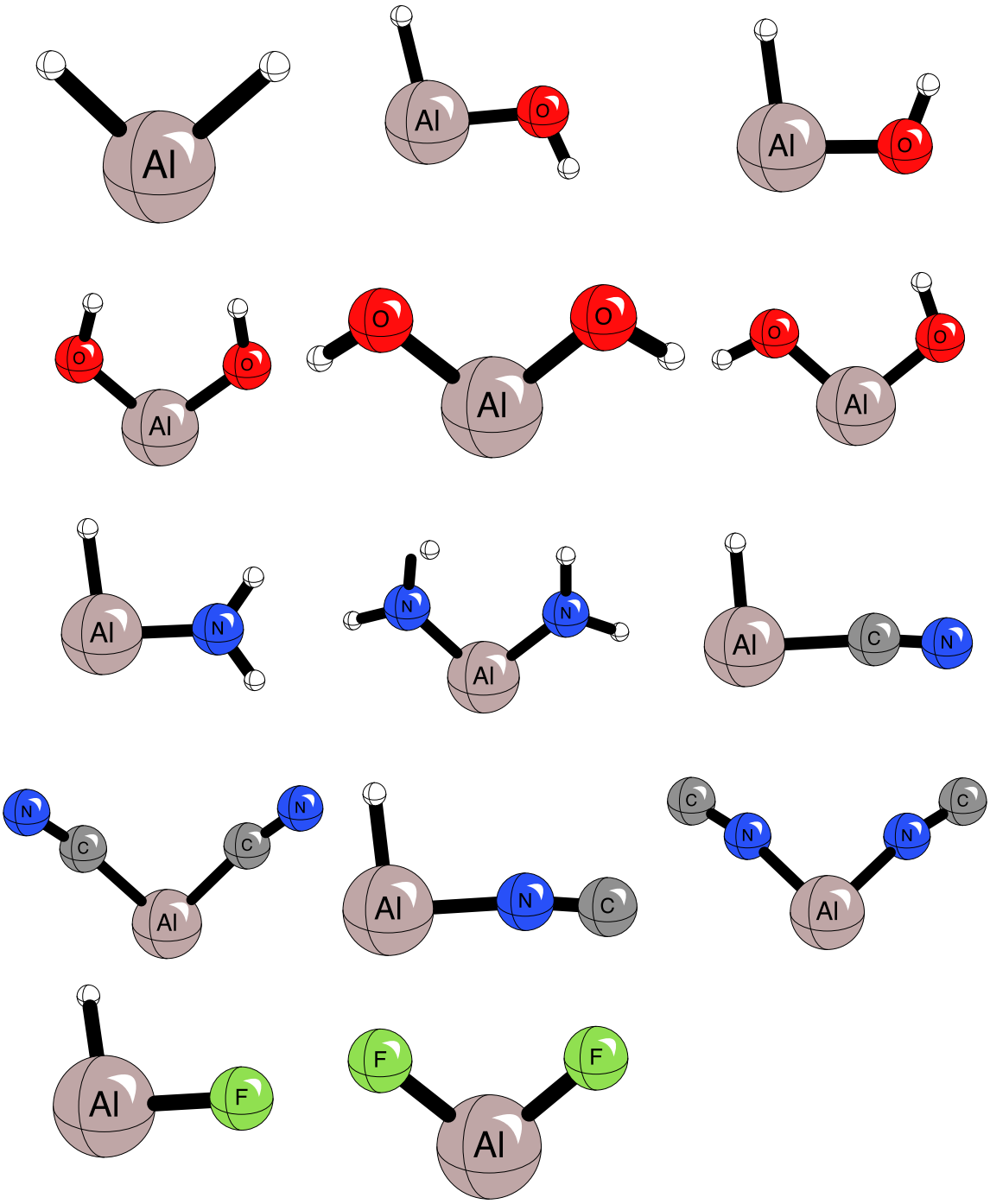

Figure 4.3: Geometries of the species used for hypohomodesmotic energy scheme

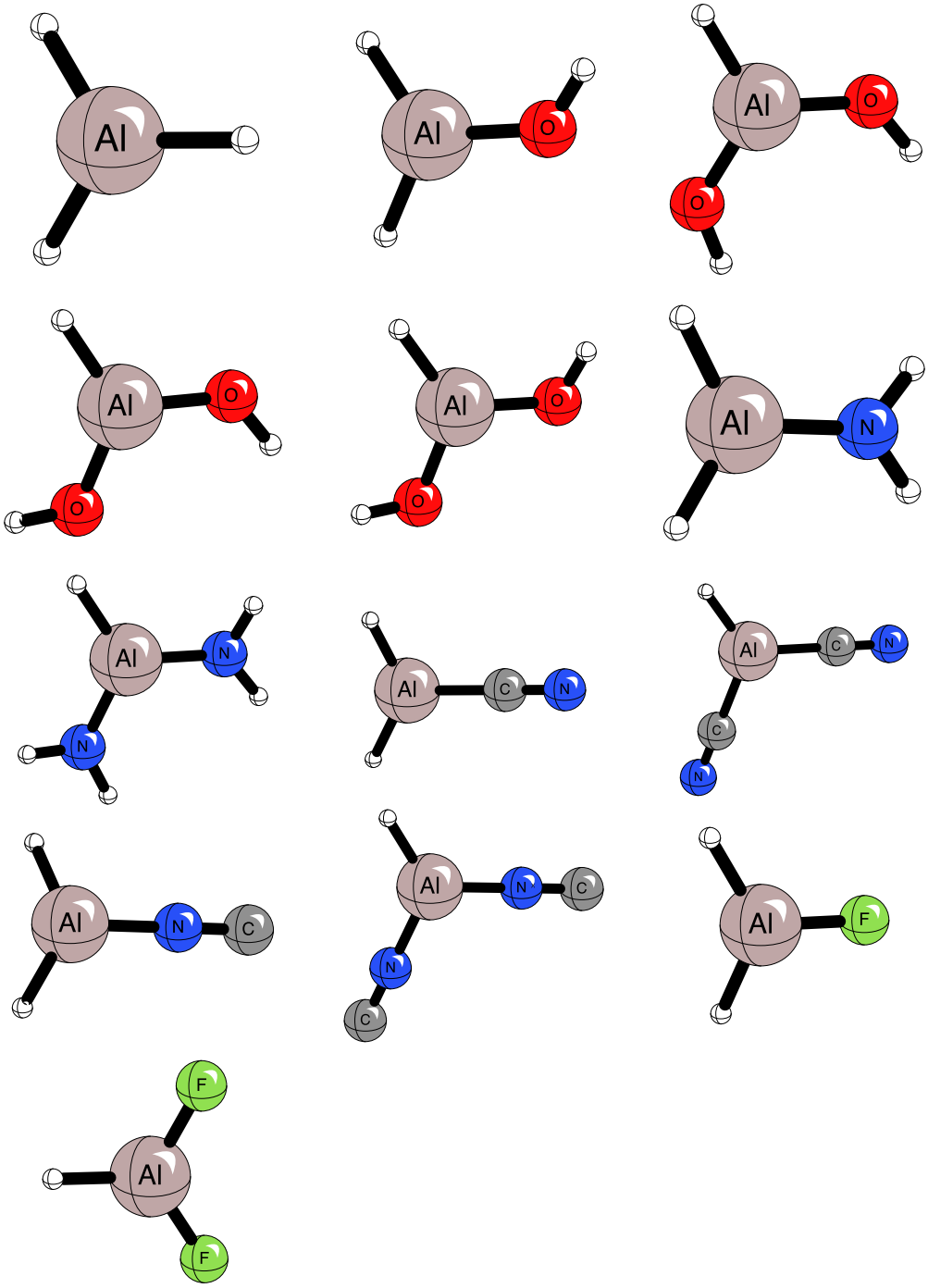

Figure 4.4: Geometries of the species used for isodesmic energy scheme.

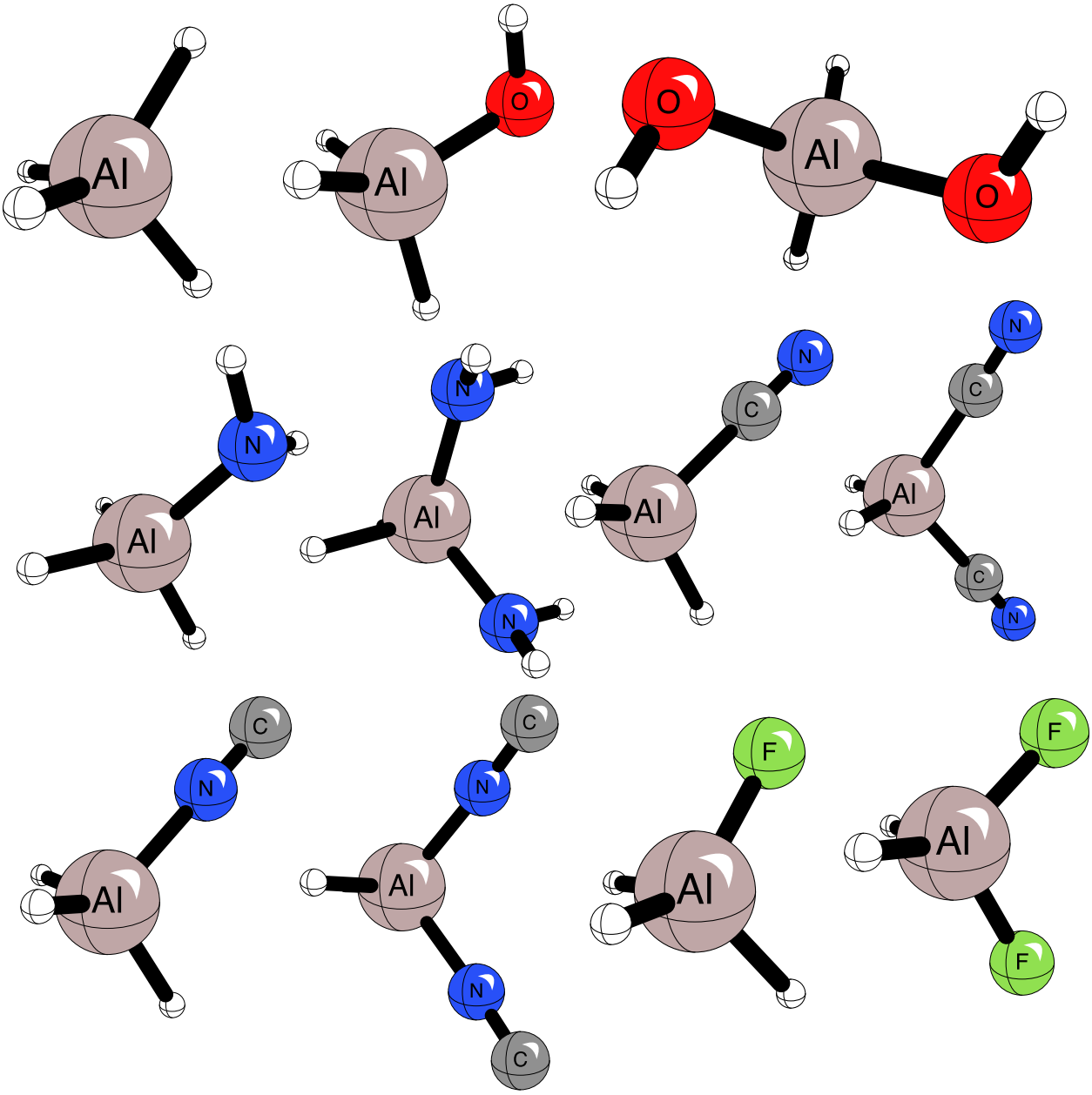

of molecules in turn leads to a bias within the energetic scheme that lowers the energy of the substituted product somewhat artificially compared to the substituted reactant.

The hypohomodesmotic scheme maintains the hybridization of the central aluminum atom however undergoes a change in charge between the substituted trivalent reactant and product carbenoid. The added proton within the reactant was shown to draw electron density away from the central aluminum, leading to an increase in the π delocalization within the neutral reactant species. This has the largest effect upon those species which are strongly π donating and thus the reaction energies were shown to increase. In the case of the amino group, both the mono- and diamino groups were shown to prefer the reactants including the non-substituted carbenoid species. This is an answer that defies logic and is shown to be a weakness of the scheme. The scheme may be useful however in cases where the π donating ability of all structures being studied is roughly equivalent.

The anion replacement energy scheme was shown to favor the same species that were favored in the isodesmic scheme. Just like in the isodesmic case, it can be concluded that the strength of the π interaction exhibited in the amino-, hydroxy- and fluoro species lowers the reaction energy to favor the products. The cyano and isocyano anions have a high electrophilicity which leads to a positive reaction energy in the anion replacement scheme. The neutral replacement scheme for these species shows a large preference for the products. This is because of the increase in electron density on the CN moiety as the neutral forms a bond with the anionic aluminum.

Given the widely varying results obtained by each energetic scheme, it is difficult to conclude that any of them is better than the others. It is a good suggestion to understand the bias that is present in the scheme chosen.

4.6 Focal Point Tables

Table 4.7: Incremented focal point talbe for the amino isodesmic reaction energy

Basis Set	RHF	+d MP2	+d CCSD	+d CCSD(T)	+d CCSDT	+d CCSDT(Q)	NET
aug-cc-pVDZ	−7.62	−1.95	+1.28	−0.48	+0.04	−0.08	[−8.81]
aug-cc-pVTZ	−7.91	−1.70	+1.26	−0.49	[+0.04]	[−0.08]	[−8.87]
aug-cc-pVQZ	−8.00	−1.69	+1.23	−0.49	[+0.04]	[−0.08]	[−8.98]
aug-cc-pV5Z	−8.00	[−1.69]	[+1.22]	[−0.49]	[+0.04]	[−0.08]	[−8.99]
CBS LIMIT	[−7.99]	[−1.68]	[+1.21]	[−0.49]	[+0.04]	[−0.08]	[−8.99]

Table 4.8: Incremented focal point talbe for the diamino (in−in) isodesmic reaction energy

Basis Set	RHF	+d MP2	+d CCSD	+d CCSD(T)	+d CCSDT	+d CCSDT(Q)	NET
aug-cc-pVDZ	−13.68	−2.65	+2.31	−0.67	+0.09	−0.11	[−14.73]
aug-cc-pVTZ	−14.22	−2.26	+2.22	−0.70	[+0.09]	[−0.11]	[−14.98]
aug-cc-pVQZ	−14.43	−2.29	+2.13	−0.70	[+0.09]	[−0.11]	[−15.31]
aug-cc-pV5Z	−14.44	[−2.30]	[+2.10]	[−0.70]	[+0.09]	[−0.11]	[−15.36]
CBS LIMIT	[−14.44]	[−2.31]	[+2.07]	[−0.70]	[+0.09]	[−0.11]	[−15.40]

Table 4.9: Incremented focal point talbe for the Hydroxy isodesmic reaction energy

Basis Set	RHF	+d MP2	+d CCSD	+d CCSD(T)	+d CCSDT	+d CCSDT(Q)	NET
aug-cc-pVDZ	−5.04	−2.29	+1.08	−0.54	+0.04	−0.07	[−6.82]
aug-cc-pVTZ	−4.93	−2.17	+1.13	−0.55	[+0.04]	[−0.07]	[−6.55]
aug-cc-pVQZ	−5.02	−2.14	+1.12	−0.56	[+0.04]	[−0.07]	[−6.63]
aug-cc-pV5Z	−5.03	[−2.13]	[+1.12]	[−0.56]	[+0.04]	[−0.07]	[−6.62]
CBS LIMIT	[−5.02]	[−2.12]	[+1.12]	[−0.57]	[+0.04]	[−0.07]	[−6.61]

Table 4.10: Incremented focal point talbe for the dihydroxy (twist) isodesmic reaction energy

Basis Set	RHF	+d MP2	+d CCSD	+d CCSD(T)	+d CCSDT	+d CCSDT(Q)	NET
aug-cc-pVDZ	−12.66	−4.70	+2.38	−1.05	+0.10	−0.14	[−16.08]
aug-cc-pVTZ	−12.46	−4.51	+2.46	−1.10	[+0.10]	[−0.14]	[−15.66]
aug-cc-pVQZ	−12.63	−4.45	+2.42	−1.13	[+0.10]	[−0.14]	[−15.83]
aug-cc-pV5Z	−12.63	[−4.43]	[+2.41]	[−1.13]	[+0.10]	[−0.14]	[−15.84]
CBS LIMIT	[−12.62]	[−4.41]	[+2.39]	[−1.14]	[+0.10]	[−0.14]	[−15.83]

Table 4.11: Incremented focal point talbe for the Cyano isodesmic reaction energy

Basis Set	RHF	+d MP2	+d CCSD	+d CCSD(T)	+d CCSDT	+d CCSDT(Q)	NET
aug-cc-pVDZ	+0.29	−1.57	+0.35	−0.33	+0.05	−0.07	[−1.27]
aug-cc-pVTZ	+0.45	−1.49	+0.48	−0.33	[+0.05]	[−0.07]	[−0.90]
aug-cc-pVQZ	+0.48	−1.43	+0.46	−0.33	[+0.05]	[−0.07]	[−0.84]
aug-cc-pV5Z	+0.48	[−1.41]	[+0.45]	[−0.33]	[+0.05]	[−0.07]	[−0.82]
CBS LIMIT	[+0.48]	[−1.39]	[+0.45]	[−0.33]	[+0.05]	[−0.07]	[−0.81]

Table 4.12: Incremented focal point talbe for the Dicyano isodesmic reaction energy

Basis Set	RHF	+d MP2	+d CCSD	+d CCSD(T)	+d CCSDT	+d CCSDT(Q)	NET
aug-cc-pVDZ	−0.40	−2.90	+0.84	−0.64	+0.11	−0.13	[−3.11]
aug-cc-pVTZ	−0.07	−2.81	+1.04	−0.64	[+0.11]	[−0.13]	[−2.50]
aug-cc-pVQZ	−0.06	−2.68	+1.02	−0.65	[+0.11]	[−0.13]	[−2.39]
aug-cc-pV5Z	−0.05	[−2.63]	[+1.01]	[−0.65]	[+0.11]	[−0.13]	[−2.35]
CBS LIMIT	[−0.04]	[−2.59]	[+1.00]	[−0.65]	[+0.11]	[−0.13]	[−2.31]

Table 4.13: Incremented focal point talbe for the Isocyano isodesmic reaction energy

Basis Set	RHF	+d MP2	+d CCSD	+d CCSD(T)	+d CCSDT	+d CCSDT(Q)	NET
aug-cc-pVDZ	−0.26	−1.54	+0.33	−0.33	+0.09	−0.06	[−1.78]
aug-cc-pVTZ	+0.14	−1.51	+0.43	−0.33	[+0.09]	[−0.06]	[−1.25]
aug-cc-pVQZ	+0.14	−1.46	+0.42	−0.33	[+0.09]	[−0.06]	[−1.21]
aug-cc-pV5Z	+0.14	[−1.44]	[+0.41]	[−0.33]	[+0.09]	[−0.06]	[−1.19]
CBS LIMIT	[+0.15]	[−1.42]	[+0.41]	[−0.33]	[+0.09]	[−0.06]	[−1.18]

Table 4.14: Incremented focal point talbe for the diisocyano isodesmic reaction energy

Basis Set	RHF	+d MP2	+d CCSD	+d CCSD(T)	+d CCSDT	+d CCSDT(Q)	NET
aug-cc-pVDZ	−3.13	−3.22	+0.99	−0.67	+0.18	−0.13	[−5.98]
aug-cc-pVTZ	−2.07	−3.23	+1.16	−0.67	[+0.18]	[−0.13]	[−4.77]
aug-cc-pVQZ	−2.09	−3.11	+1.14	−0.68	[+0.18]	[−0.13]	[−4.69]
aug-cc-pV5Z	−2.08	[−3.06]	[+1.13]	[−0.68]	[+0.18]	[−0.13]	[−4.65]
CBS LIMIT	[−2.08]	[−3.01]	[+1.12]	[−0.69]	[+0.18]	[−0.13]	[−4.60]

Table 4.15: Incremented focal point talbe for the luoro isodesmic reaction energy

Basis Set	RHF	+d MP2	+d CCSD	+d CCSD(T)	+d CCSDT	+d CCSDT(Q)	NET
aug-cc-pVDZ	−2.12	−1.36	+0.39	−0.26	+0.04	−0.02	[−3.32]
aug-cc-pVTZ	−1.98	−1.28	+0.44	−0.28	[+0.04]	[−0.02]	[−3.07]
aug-cc-pVQZ	−2.08	−1.25	+0.43	−0.29	[+0.04]	[−0.02]	[−3.17]
aug-cc-pV5Z	−2.08	[−1.24]	[+0.43]	[−0.29]	[+0.04]	[−0.02]	[−3.16]
CBS LIMIT	[−2.08]	[−1.23]	[+0.42]	[−0.30]	[+0.04]	[−0.02]	[−3.16]

Table 4.16: Incremented focal point table for the difluoro isodesmic reaction energy

Basis Set	RHF	+d MP2	+d CCSD	+d CCSD(T)	+d CCSDT	+d CCSDT(Q)	NET
aug-cc-pVDZ	−8.52	−3.46	+1.30	−0.61	+0.09	−0.04	[−11.23]
aug-cc-pVTZ	−8.08	−3.36	+1.41	−0.69	[+0.09]	[−0.04]	[−10.68]
aug-cc-pVQZ	−8.28	−3.33	+1.37	−0.72	[+0.09]	[−0.04]	[−10.92]
aug-cc-pV5Z	−8.28	[−3.31]	[+1.35]	[−0.73]	[+0.09]	[−0.04]	[−10.92]
CBS LIMIT	[−8.26]	[−3.30]	[+1.34]	[−0.74]	[+0.09]	[−0.04]	[−10.92]

Table 4.17: Incremented focal point table for the amino hypohomodesmotic reaction energy.

Basis Set	RHF	+δ MP2	+δ CCSD	+δ CCSD(T)	+δ CCSDT	+δ CCSDT(Q)	NET
aug-cc-pVDZ	+4.42	−2.63	+1.63	−0.56	+0.10	−0.07	[+2.90]
aug-cc-pVTZ	+4.91	−2.55	+1.62	−0.53	[+0.10]	[−0.07]	[+3.48]
aug-cc-pVQZ	+4.87	−2.42	+1.61	−0.52	[+0.10]	[−0.07]	[+3.57]
aug-cc-pV5Z	+4.89	[−2.38]	[+1.60]	[−0.52]	[+0.10]	[−0.07]	[+3.62]
CBS LIMIT	[+4.90]	[−2.34]	[+1.60]	[−0.51]	[+0.10]	[−0.07]	[+3.68]

Table 4.18: Incremented focal point table for the diamino hypohomodesmotic reaction energy.

Basis Set	RHF	+δ MP2	+δ CCSD	+δ CCSD(T)	+δ CCSDT	+δ CCSDT(Q)	NET
aug-cc-pVDZ	+5.93	−6.07	+3.10	−1.24	+0.17	−0.14	[+1.74]
aug-cc-pVTZ	+7.10	−5.80	+3.19	−1.22	[+0.17]	[−0.14]	[+3.29]
aug-cc-pVQZ	+7.01	−5.51	+3.15	−1.20	[+0.17]	[−0.14]	[+3.47]
aug-cc-pV5Z	+7.04	[−5.41]	[+3.14]	[−1.20]	[+0.17]	[−0.14]	[+3.59]
CBS LIMIT	[+7.06]	[−5.31]	[+3.13]	[−1.19]	[+0.17]	[−0.14]	[+3.71]

Table 4.19: Incremented focal point table for the hydroxy (syn) hypohomodesmotic reaction energy.

Basis Set	RHF	+δ MP2	+δ CCSD	+δ CCSD(T)	+δ CCSDT	+δ CCSDT(Q)	NET

Table 4.20: Incremented focal point table for the hydroxy (anti) hypohomodesmotic reaction energy.

Basis Set	RHF	+δ MP2	+δ CCSD	+δ CCSD(T)	+δ CCSDT	+δ CCSDT(Q)	NET
aug-cc-pVDZ	−0.06	−2.51	+1.32	−0.50	+0.10	−0.07	[−1.72]
aug-cc-pVTZ	+0.77	−2.48	+1.36	−0.49	[+0.10]	[−0.07]	[−0.81]
aug-cc-pVQZ	+0.74	−2.43	+1.37	−0.49	[+0.10]	[−0.07]	[−0.78]
aug-cc-pV5Z	+0.76	[−2.41]	[+1.37]	[−0.49]	[+0.10]	[−0.07]	[−0.74]
CBS LIMIT	[+0.77]	[−2.38]	[+1.37]	[−0.49]	[+0.10]	[−0.07]	[−0.70]

Table 4.21: Incremented focal point table for the dihydroxy (in−in) hypohomodesmotic reaction energy.

Basis Set	RHF	+δ MP2	+δ CCSD	+δ CCSD(T)	+δ CCSDT	+δ CCSDT(Q)	NET
aug-cc-pVDZ	−3.20	−5.90	+2.54	−1.06	+0.18	−0.12	[−7.57]
aug-cc-pVTZ	−1.26	−5.82	+2.64	−1.09	[+0.18]	[−0.12]	[−5.47]
aug-cc-pVQZ	−1.30	−5.65	+2.62	−1.10	[+0.18]	[−0.12]	[−5.38]
aug-cc-pV5Z	−1.25	[−5.59]	[+2.61]	[−1.10]	[+0.18]	[−0.12]	[−5.28]
CBS LIMIT	[−1.21]	[−5.53]	[+2.60]	[−1.11]	[+0.18]	[−0.12]	[−5.20]

Table 4.22: Incremented focal point table for the dihydroxy (in−out) hypohomodesmotic reaction energy.

Basis Set	RHF	+δ MP2	+δ CCSD	+δ CCSD(T)	+δ CCSDT	+δ CCSDT(Q)	NET
aug-cc-pVDZ	−5.44	−5.71	+2.63	−1.03	+0.18	−0.12	[−9.50]
aug-cc-pVTZ	−3.50	−5.67	+2.73	−1.06	[+0.18]	[−0.12]	[−7.45]
aug-cc-pVQZ	−3.53	−5.53	+2.71	−1.07	[+0.18]	[−0.12]	[−7.37]
aug-cc-pV5Z	−3.48	[−5.49]	[+2.71]	[−1.08]	[+0.18]	[−0.12]	[−7.28]
CBS LIMIT	[−3.45]	[−5.44]	[+2.70]	[−1.08]	[+0.18]	[−0.12]	[−7.21]

Table 4.23: Incremented focal point table for the dihydroxy (out−out) hypohomodesmotic reaction energy.

Basis Set	RHF	+δ MP2	+δ CCSD	+δ CCSD(T)	+δ CCSDT	+δ CCSDT(Q)	NET
aug-cc-pVDZ	−5.74	−5.85	+2.81	−1.12	+0.17	−0.14	[−9.87]
aug-cc-pVTZ	−4.04	−5.75	+2.91	−1.15	[+0.17]	[−0.14]	[−8.00]
aug-cc-pVQZ	−4.10	−5.61	+2.89	−1.16	[+0.17]	[−0.14]	[−7.94]
aug-cc-pV5Z	−4.06	[−5.56]	[+2.89]	[−1.16]	[+0.17]	[−0.14]	[−7.86]
CBS LIMIT	[−4.02]	[−5.51]	[+2.88]	[−1.16]	[+0.17]	[−0.14]	[−7.78]

Table 4.24: Incremented focal point table for the cyano hypohomodesmotic reaction energy.

Basis Set	RHF	+δ MP2	+δ CCSD	+δ CCSD(T)	+δ CCSDT	+δ CCSDT(Q)	NET
aug-cc-pVDZ	−21.43	+0.34	+0.18	−0.16	+0.07	+0.02	[−20.99]
aug-cc-pVTZ	−20.95	+0.27	+0.21	−0.08	[+0.07]	[+0.02]	[−20.45]
aug-cc-pVQZ	−20.93	+0.32	+0.18	−0.06	[+0.07]	[+0.02]	[−20.41]
aug-cc-pV5Z	−20.92	[+0.33]	[+0.16]	[−0.06]	[+0.07]	[+0.02]	[−20.39]
CBS LIMIT	[−20.91]	[+0.35]	[+0.15]	[−0.05]	[+0.07]	[+0.02]	[−20.38]

Table 4.25: Incremented focal point table for the dicyano hypohomodesmotic reaction energy.

Basis Set	RHF	+δ MP2	+δ CCSD	+δ CCSD(T)	+δ CCSDT	+δ CCSDT(Q)	NET
aug-cc-pVDZ	−42.75	+1.02	+0.36	−0.20	+0.12	+0.06	[−41.39]
aug-cc-pVTZ	−41.91	+0.82	+0.40	−0.05	[+0.12]	[+0.06]	[−40.56]
aug-cc-pVQZ	−41.91	+0.93	+0.32	−0.02	[+0.12]	[+0.06]	[−40.50]
aug-cc-pV5Z	−41.89	[+0.97]	[+0.29]	[−0.01]	[+0.12]	[+0.06]	[−40.46]
CBS LIMIT	[−41.87]	[+1.01]	[+0.26]	[−0.01]	[+0.12]	[+0.06]	[−40.43]

Table 4.26: Incremented focal point table for the isocyano hypohomodesmotic reaction energy.

Basis Set	RHF	+δ MP2	+δ CCSD	+δ CCSD(T)	+δ CCSDT	+δ CCSDT(Q)	NET
aug-cc-pVDZ	−16.35	−4.95	+1.96	−0.40	+0.21	−0.18	[−19.71]
aug-cc-pVTZ	−14.99	−5.22	+2.10	−0.42	[+0.21]	[−0.18]	[−18.50]
aug-cc-pVQZ	−14.99	−5.16	+2.13	−0.42	[+0.21]	[−0.18]	[−18.42]
aug-cc-pV5Z	−14.99	[−5.14]	[+2.14]	[−0.43]	[+0.21]	[−0.18]	[−18.38]
CBS LIMIT	[−14.98]	[−5.12]	[+2.15]	[−0.43]	[+0.21]	[−0.18]	[−18.34]

Table 4.27: Incremented focal point table for the diisocyano hypohomodesmotic reaction energy.

Basis Set	RHF	+δ MP2	+δ CCSD	+δ CCSD(T)	+δ CCSDT	+δ CCSDT(Q)	NET
aug-cc-pVDZ	−35.26	−9.96	+4.09	−0.78	+0.40	−0.34	[−41.85]
aug-cc-pVTZ	−32.33	−10.46	+4.37	−0.84	[+0.40]	[−0.34]	[−39.20]
aug-cc-pVQZ	−32.37	−10.30	+4.41	−0.86	[+0.40]	[−0.34]	[−39.06]
aug-cc-pV5Z	−32.34	[−10.25]	[+4.43]	[−0.86]	[+0.40]	[−0.34]	[−38.96]
CBS LIMIT	[−32.32]	[−10.19]	[+4.44]	[−0.86]	[+0.40]	[−0.34]	[−38.87]

Table 4.28: Incremented focal point table for the fluoro hypohomodesmotic reaction energy.

Basis Set	RHF	+δ MP2	+δ CCSD	+δ CCSD(T)	+δ CCSDT	+δ CCSDT(Q)	NET
aug-cc-pVDZ	−6.17	−0.60	+0.50	−0.08	+0.09	−0.00	[−6.27]
aug-cc-pVTZ	−5.24	−0.64	+0.51	−0.08	[+0.09]	[−0.00]	[−5.37]
aug-cc-pVQZ	−5.23	−0.66	+0.50	−0.09	[+0.09]	[−0.00]	[−5.38]
aug-cc-pV5Z	−5.21	[−0.66]	[+0.50]	[−0.09]	[+0.09]	[−0.00]	[−5.37]
CBS LIMIT	[−5.21]	[−0.67]	[+0.50]	[−0.09]	[+0.09]	[−0.00]	[−5.37]

Table 4.29: Incremented focal point table for the difluoro hypohomodesmotic reaction energy.

Basis Set	RHF	+δ MP2	+δ CCSD	+δ CCSD(T)	+δ CCSDT	+δ CCSDT(Q)	NET
aug-cc-pVDZ	−20.29	−2.33	+1.45	−0.35	+0.17	−0.02	[−21.36]
aug-cc-pVTZ	−18.12	−2.48	+1.47	−0.42	[+0.17]	[−0.02]	[−19.39]
aug-cc-pVQZ	−18.08	−2.53	+1.44	−0.44	[+0.17]	[−0.02]	[−19.45]
aug-cc-pV5Z	−18.05	[−2.55]	[+1.43]	[−0.45]	[+0.17]	[−0.02]	[−19.46]
CBS LIMIT	[−18.03]	[−2.57]	[+1.42]	[−0.46]	[+0.17]	[−0.02]	[−19.48]

Table 4.30: Incremented focal point table for the nitro hypohomodesmotic reaction energy.

Basis Set	RHF	+δ MP2	+δ CCSD	+δ CCSD(T)	+δ CCSDT	+δ CCSDT(Q)	NET
aug-cc-pVDZ	−36.10	+3.08	−1.14	+0.43	+0.08	+0.12	[−33.53]
aug-cc-pVTZ	−35.22	+3.01	−1.05	+0.54	[+0.08]	[+0.12]	[−32.53]
aug-cc-pVQZ	−35.22	+2.99	−1.11	+0.56	[+0.08]	[+0.12]	[−32.58]
aug−aug-cc-pV5Z	−35.22	[+2.98]	[−1.13]	[+0.57]	[+0.08]	[+0.12]	[−32.61]
CBS LIMIT	[−35.22]	[+2.97]	[−1.15]	[+0.58]	[+0.08]	[+0.12]	[−32.63]

Table 4.31: Incremented focal point table for the direct formation of the hydroxy aluminyl anion from hydroxide.

	RHF	+δ MP2	+δ CCSD	+δ CCSD(T)	+δ CCSDT	+δ CCSDT(Q)	NET
aug-cc-pVDZ	−25.27	+7.84	−4.00	+0.76	+0.23	+0.12	[−20.32]
aug-cc-pVTZ	−27.48	+8.65	−4.21	+1.15	[+0.23]	[+0.12]	[−21.55]
aug-cc-pVQZ	−27.94	+8.83	−4.47	+1.26	[+0.23]	[+0.12]	[−21.97]
aug-cc-pV5Z	−27.99	[+8.89]	[−4.56]	[+1.29]	[+0.23]	[+0.12]	[−22.02]
CBS LIMIT	[−27.99]	[+8.96]	[−4.66]	[+1.33]	[+0.23]	[+0.12]	[−22.00]

Table 4.32: Incremented focal point table for the direct formation of the dihydroxy aluminyl anion from hydroxide.

	RHF	+δ MP2	+δ CCSD	+δ CCSD(T)	+δ CCSDT	+δ CCSDT(Q)	NET
aug-cc-pVDZ	−55.02	+15.67	−8.03	+1.53	+0.43	+0.25	[−45.16]
aug-cc-pVTZ	−59.66	+17.22	−8.56	+2.30	[+0.43]	[+0.25]	[−48.02]
aug-cc-pVQZ	−60.50	+17.57	−9.09	+2.50	[+0.43]	[+0.25]	[−48.84]
aug-cc-pV5Z	−60.62	[+17.70]	[−9.28]	[+2.57]	[+0.43]	[+0.25]	[−48.95]
CBS LIMIT	[−60.63]	[+17.83]	[−9.48]	[+2.65]	[+0.43]	[+0.25]	[−48.95]

Table 4.33: Incremented focal point table for the direct formation of the amino aluminyl anion from amide.

	RHF	+δ MP2	+δ CCSD	+δ CCSD(T)	+δ CCSDT	+δ CCSDT(Q)	NET
aug-cc-pVDZ	−24.96	+6.09	−2.97	+0.76	+0.18	+0.08	[−20.81]
aug-cc-pVTZ	−27.30	+7.11	−3.38	+1.05	[+0.18]	[+0.08]	[−22.25]
aug-cc-pVQZ	−27.40	+7.21	−3.65	+1.13	[+0.18]	[+0.08]	[−22.44]
aug-cc-pV5Z	−27.39	[+7.25]	[−3.75]	[+1.16]	[+0.18]	[+0.08]	[−22.46]
CBS LIMIT	[−27.38]	[+7.29]	[−3.86]	[+1.20]	[+0.18]	[+0.08]	[−22.48]

Table 4.34: Incremented focal point table for the direct formation of the diamino aluminyl anion from amide.

	RHF	+δ MP2	+δ CCSD	+δ CCSD(T)	+δ CCSDT	+δ CCSDT(Q)	NET
aug-cc-pVDZ	−50.26	+12.54	−6.16	+1.62	+0.35	+0.20	[−41.71]
aug-cc-pVTZ	−54.67	+14.46	−7.03	+2.17	[+0.35]	[+0.20]	[−44.53]
aug-cc-pVQZ	−54.86	+14.65	−7.60	+2.34	[+0.35]	[+0.20]	[−44.92]
aug-cc-pV5Z	−54.85	[+14.72]	[−7.80]	[+2.40]	[+0.35]	[+0.20]	[−44.98]
CBS LIMIT	[−54.83]	[+14.80]	[−8.01]	[+2.47]	[+0.35]	[+0.20]	[−45.03]

Table 4.35: Incremented focal point table for the direct formation of the cyano aluminyl anion from cyanide.

	RHF	+δ MP2	+δ CCSD	+δ CCSD(T)	+δ CCSDT	+δ CCSDT(Q)	NET
aug-cc-pVDZ	+18.93	−2.20	−1.29	−0.01	+0.20	−0.12	[+15.51]
aug-cc-pVTZ	+17.57	−1.52	−1.21	+0.08	[+0.20]	[−0.12]	[+15.01]
aug-cc-pVQZ	+17.71	−1.41	−1.26	+0.09	[+0.20]	[−0.12]	[+15.21]
aug-cc-pV5Z	+17.67	[−1.38]	[−1.27]	[+0.09]	[+0.20]	[−0.12]	[+15.20]
CBS LIMIT	[+17.65]	[−1.34]	[−1.29]	[+0.09]	[+0.20]	[−0.12]	[+15.20]

Table 4.36: Incremented focal point table for the direct formation of the dicyano aluminyl anion from cyanide.

	RHF	+δ MP2	+δ CCSD	+δ CCSD(T)	+δ CCSDT	+δ CCSDT(Q)	NET
aug-cc-pVDZ	+41.85	−5.15	−2.29	−0.04	+0.39	−0.25	[+34.51]
aug-cc-pVTZ	+39.17	−3.74	−2.18	+0.12	[+0.39]	[−0.25]	[+33.51]
aug-cc-pVQZ	+39.42	−3.48	−2.25	+0.13	[+0.39]	[−0.25]	[+33.97]
aug-cc-pV5Z	+39.36	[−3.38]	[−2.28]	[+0.13]	[+0.39]	[−0.25]	[+33.97]
CBS LIMIT	[+39.30]	[−3.29]	[−2.30]	[+0.14]	[+0.39]	[−0.25]	[+33.99]

Table 4.37: Incremented focal point table for the direct formation of the isocyano aluminyl anion from cyanide.

	RHF	+δ MP2	+δ CCSD	+δ CCSD(T)	+δ CCSDT	+δ CCSDT(Q)	NET
aug-cc-pVDZ	+16.79	+2.12	−2.77	+0.26	+0.18	+0.07	[+16.64]
aug-cc-pVTZ	+14.72	+3.14	−2.72	+0.42	[+0.18]	[+0.07]	[+15.82]
aug-cc-pVQZ	+14.77	+3.30	−2.83	+0.46	[+0.18]	[+0.07]	[+15.94]
aug-cc-pV5Z	+14.74	[+3.36]	[−2.87]	[+0.47]	[+0.18]	[+0.07]	[+15.94]
CBS LIMIT	[+14.72]	[+3.41]	[−2.91]	[+0.48]	[+0.18]	[+0.07]	[+15.95]

Table 4.38: Incremented focal point table for the direct formation of the diisocyano aluminyl anion from cyanide.

	RHF	+δ MP2	+δ CCSD	+δ CCSD(T)	+δ CCSDT	+δ CCSDT(Q)	NET
aug-cc-pVDZ	+33.49	+5.20	−5.76	+0.57	+0.29	+0.19	[+33.97]
aug-cc-pVTZ	+29.32	+7.33	−5.76	+0.91	[+0.29]	[+0.19]	[+32.29]
aug-cc-pVQZ	+29.42	+7.67	−5.99	+0.97	[+0.29]	[+0.19]	[+32.56]
aug-cc-pV5Z	+29.36	[+7.79]	[−6.07]	[+1.00]	[+0.29]	[+0.19]	[+32.56]
CBS LIMIT	[+29.32]	[+7.92]	[−6.15]	[+1.02]	[+0.29]	[+0.19]	[+32.58]

Table 4.39: Incremented focal point table for the direct formation of the fluoro aluminyl anion from fluoride.

	RHF	+δ MP2	+δ CCSD	+δ CCSD(T)	+δ CCSDT	+δ CCSDT(Q)	NET
aug-cc-pVDZ	−20.51	+7.34	−4.17	+0.75	+0.27	+0.09	[−16.22]
aug-cc-pVTZ	−22.58	+8.02	−4.19	+1.17	[+0.27]	[+0.09]	[−17.22]
aug-cc-pVQZ	−23.50	+8.30	−4.41	+1.29	[+0.27]	[+0.09]	[−17.95]
aug-cc-pV5Z	−23.57	[+8.40]	[−4.49]	[+1.34]	[+0.27]	[+0.09]	[−17.96]
CBS LIMIT	[−23.53]	[+8.50]	[−4.57]	[+1.39]	[+0.27]	[+0.09]	[−17.85]

Table 4.40: Incremented focal point table for the direct formation of the difluoro aluminyl anion from fluoride.

	RHF	+δ MP2	+δ CCSD	+δ CCSD(T)	+δ CCSDT	+δ CCSDT(Q)	NET
aug-cc-pVDZ	−47.95	+13.64	−8.06	+1.34	+0.52	+0.16	[−40.35]
aug-cc-pVTZ	−52.10	+15.02	−8.14	+2.15	[+0.52]	[+0.16]	[−42.40]
aug-cc-pVQZ	−53.94	+15.57	−8.60	+2.39	[+0.52]	[+0.16]	[−43.91]
aug-cc-pV5Z	−54.08	[+15.77]	[−8.77]	[+2.48]	[+0.52]	[+0.16]	[−43.93]
CBS LIMIT	[−53.99]	[+15.98]	[−8.94]	[+2.57]	[+0.52]	[+0.16]	[−43.71]

Table 4.41: Incremented focal point table for the direct formation of the hydroxy aluminyl anion from hydroxyl radical.

	RHF	$+\delta$ MP2	$+\delta$ CCSD	$+\delta$ CCSD(T)	$+\delta$ CCSDT	$+\delta$ CCSDT(Q)	NET
aug-cc-pVDZ	−28.25	−26.07	+13.79	−2.17	+0.27	−0.30	[−42.74]
aug-cc-pVTZ	−29.17	−27.24	+14.16	−2.93	[+0.27]	[−0.30]	[−45.21]
aug-cc-pVQZ	−29.46	−28.06	+14.02	−3.07	[+0.27]	[−0.30]	[−46.61]
aug-cc-pV5Z	−29.46	[−28.35]	[+13.97]	[−3.12]	[+0.27]	[−0.30]	[−46.99]
CBS LIMIT	[−29.43]	[−28.65]	[+13.92]	[−3.17]	[+0.27]	[−0.30]	[−47.38]

Table 4.42: Incremented focal point table for the direct formation of the dihydroxy aluminyl anion from hydroxyl radical.

	RHF	$+\delta$ MP2	$+\delta$ CCSD	$+\delta$ CCSD(T)	$+\delta$ CCSDT	$+\delta$ CCSDT(Q)	NET
aug-cc-pVDZ	−60.99	−52.14	+27.55	−4.33	+0.50	−0.58	[−90.00]
aug-cc-pVTZ	−63.03	−54.55	+28.20	−5.87	[+0.50]	[−0.58]	[−95.34]
aug-cc-pVQZ	−63.56	−56.20	+27.89	−6.16	[+0.50]	[−0.58]	[−98.11]
aug-cc-pV5Z	−63.56	[−56.78]	[+27.78]	[−6.26]	[+0.50]	[−0.58]	[−98.91]
CBS LIMIT	[−63.51]	[−57.40]	[+27.66]	[−6.37]	[+0.50]	[−0.58]	[−99.70]

Table 4.43: Incremented focal point table for the direct formation of the amino aluminyl anion from aminyl radical.

	RHF	$+\delta$ MP2	$+\delta$ CCSD	$+\delta$ CCSD(T)	$+\delta$ CCSDT	$+\delta$ CCSDT(Q)	NET
aug-cc-pVDZ	−8.71	−19.93	+12.32	−2.17	+0.28	−0.26	[−18.46]
aug-cc-pVTZ	−10.20	−20.61	+12.34	−2.72	[+0.28]	[−0.26]	[−21.18]
aug-cc-pVQZ	−10.23	−21.24	+12.21	−2.83	[+0.28]	[−0.26]	[−22.06]
aug-cc-pV5Z	−10.21	[−21.46]	[+12.17]	[−2.86]	[+0.28]	[−0.26]	[−22.35]
CBS LIMIT	[−10.20]	[−21.69]	[+12.12]	[−2.90]	[+0.28]	[−0.26]	[−22.66]

Table 4.44: Incremented focal point table for the direct formation of the diamino aluminyl anion from aminyl radical.

	RHF	$+\delta$ MP2	$+\delta$ CCSD	$+\delta$ CCSD(T)	$+\delta$ CCSDT	$+\delta$ CCSDT(Q)	NET
aug-cc-pVDZ	−16.91	−39.50	+24.43	−4.25	+0.54	−0.49	[−36.18]
aug-cc-pVTZ	−20.25	−40.99	+24.40	−5.37	[+0.54]	[−0.49]	[−42.16]
aug-cc-pVQZ	−20.45	−42.25	+24.13	−5.58	[+0.54]	[−0.49]	[−44.09]
aug-cc-pV5Z	−20.49	[−42.69]	[+24.04]	[−5.65]	[+0.54]	[−0.49]	[−44.74]
CBS LIMIT	[−20.49]	[−43.17]	[+23.94]	[−5.73]	[+0.54]	[−0.49]	[−45.40]

Table 4.45: Incremented focal point table for the direct formation of the cyano aluminyl anion from cyano radical.

	RHF	$+\delta$ MP2	$+\delta$ CCSD	$+\delta$ CCSD(T)	$+\delta$ CCSDT	$+\delta$ CCSDT(Q)	NET
aug-cc-pVDZ	−55.69	−27.68	+28.77	−0.79	+1.75	+0.23	[−53.41]
aug-cc-pVTZ	−56.23	−30.06	+29.46	−0.69	[+1.75]	[+0.23]	[−55.54]
aug-cc-pVQZ	−55.86	−31.17	+29.81	−0.66	[+1.75]	[+0.23]	[−55.89]
aug-cc-pV5Z	−55.83	[−31.57]	[+29.94]	[−0.64]	[+1.75]	[+0.23]	[−56.12]
CBS LIMIT	[−55.84]	[−31.99]	[+30.07]	[−0.63]	[+1.75]	[+0.23]	[−56.40]

Table 4.46: Incremented focal point table for the direct formation of the dicyano aluminyl anion from cyano radical.

	RHF	+δ MP2	+δ CCSD	+δ CCSD(T)	+δ CCSDT	+δ CCSDT(Q)	NET
aug-cc-pVDZ	−107.39	−56.10	+57.83	−1.61	+3.50	+0.45	[−103.33]
aug-cc-pVTZ	−108.44	−60.82	+59.15	−1.42	[+3.50]	[+0.45]	[−107.57]
aug-cc-pVQZ	−107.71	−63.00	+59.88	−1.35	[+3.50]	[+0.45]	[−108.23]
aug-cc-pV5Z	−107.65	[−63.77]	[+60.14]	[−1.33]	[+3.50]	[+0.45]	[−108.67]
CBS LIMIT	[−107.66]	[−64.59]	[+60.41]	[−1.31]	[+3.50]	[+0.45]	[−109.20]

Table 4.47: Incremented focal point table for the direct formation of the isocyano aluminyl anion from cyano radical.

	RHF	+δ MP2	+δ CCSD	+δ CCSD(T)	+δ CCSDT	+δ CCSDT(Q)	NET
aug-cc-pVDZ	−57.84	−23.36	+27.29	−0.52	+1.73	+0.42	[−52.28]
aug-cc-pVTZ	−59.08	−25.40	+27.95	−0.34	[+1.73]	[+0.42]	[−54.72]
aug-cc-pVQZ	−58.80	−26.46	+28.24	−0.29	[+1.73]	[+0.42]	[−55.16]
aug-cc-pV5Z	−58.76	[−26.84]	[+28.34]	[−0.26]	[+1.73]	[+0.42]	[−55.38]
CBS LIMIT	[−58.76]	[−27.24]	[+28.45]	[−0.24]	[+1.73]	[+0.42]	[−55.64]

Table 4.48: Incremented focal point table for the direct formation of the diisocyano aluminyl anion from cyano radical.

	RHF	+δ MP2	+δ CCSD	+δ CCSD(T)	+δ CCSDT	+δ CCSDT(Q)	NET
aug-cc-pVDZ	−115.76	−45.75	+54.36	−1.00	+3.39	+0.89	[−103.87]
aug-cc-pVTZ	−118.29	−49.75	+55.57	−0.62	[+3.39]	[+0.89]	[−108.80]
aug-cc-pVQZ	−117.71	−51.85	+56.14	−0.51	[+3.39]	[+0.89]	[−109.64]
aug-cc-pV5Z	−117.65	[−52.60]	[+56.35]	[−0.47]	[+3.39]	[+0.89]	[−110.08]
CBS LIMIT	[−117.64]	[−53.38]	[+56.56]	[−0.43]	[+3.39]	[+0.89]	[−110.60]

Table 4.49: Incremented focal point table for the direct formation of the fluoro aluminyl anion from fluorine.

	RHF	+δ MP2	+δ CCSD	+δ CCSD(T)	+δ CCSDT	+δ CCSDT(Q)	NET
aug-cc-pVDZ	−58.00	−28.98	+13.01	−1.52	+0.20	−0.20	[−75.49]
aug-cc-pVTZ	−57.79	−30.61	+13.74	−2.51	[+0.20]	[−0.20]	[−77.18]
aug-cc-pVQZ	−58.33	−31.71	+13.56	−2.68	[+0.20]	[−0.20]	[−79.17]
aug-cc-pV5Z	−58.26	[−32.11]	[+13.50]	[−2.74]	[+0.20]	[−0.20]	[−79.60]
CBS LIMIT	[−58.14]	[−32.52]	[+13.43]	[−2.80]	[+0.20]	[−0.20]	[−80.03]

Table 4.50: Incremented focal point table for the direct formation of the difluoro aluminyl anion from fluorine.

	RHF	+δ MP2	+δ CCSD	+δ CCSD(T)	+δ CCSDT	+δ CCSDT(Q)	NET
aug-cc-pVDZ	−122.94	−59.00	+26.31	−3.21	+0.37	−0.42	[−158.89]
aug-cc-pVTZ	−122.51	−62.26	+27.72	−5.21	[+0.37]	[−0.42]	[−162.31]
aug-cc-pVQZ	−123.62	−64.46	+27.34	−5.55	[+0.37]	[−0.42]	[−166.34]
aug-cc-pV5Z	−123.46	[−65.24]	[+27.20]	[−5.67]	[+0.37]	[−0.42]	[−167.22]
CBS LIMIT	[−123.22]	[−66.06]	[+27.06]	[−5.80]	[+0.37]	[−0.42]	[−168.07]

4.7 Harmonic Frequencies

See Fig. 4.2-4.4 for the structures of the molecules. All frequencies reported were computed at the CCSD(T)/aug-cc-pV(T+d)Z level of theory.

4.7.1 ÄlH$_2^-$ Derivatives

Table 4.51: ÄlH$_2^-$

Harmonic Frequencies	
Mode	ω
1	1492
2	1481
3	802

Table 4.52: Hydroxy (anti)

Harmonic Frequencies	
Mode	ω
1	3862
2	1457
3	783
4	650
5	597
6	482

Table 4.53: Hydroxy (syn)

Harmonic Frequencies	
Mode	ω
1	3850
2	1342
3	786
4	644
5	548
6	482

Table 4.54: Dihydroxy(in-in)

HARMONIC FREQUENCIES	
Mode	ω
1	3789
2	3787
3	737
4	650
5	611
6	568
7	351
8	253
9	160

Table 4.55: Dihydroxy(in-out)

Harmonic Frequencies	
Mode	ω
1	3853
2	3794
3	737
4	698
5	661
6	626
7	403
8	328
9	229

Table 4.56: Dihydroxy (out-out)

Harmonic Frequencies	
Mode	ω
1	3855
2	3851
3	738
4	709
5	660
6	638
7	361
8	315
9	237

Table 4.57: Amino

Harmonic Frequencies	
Mode	ω
1	3613
2	3510
3	1552
4	1437
5	737
6	647
7	558
8	498
9	307

Table 4.58: Diamino

Harmonic Frequencies	
Mode	ω
1	3608
2	3608
3	3481
4	3475
5	1557
6	1539
7	656
8	651
9	614
10	527
11	418
12	253
13	214
14	190
15	57

Table 4.59: Cyano

Harmonic Frequencies	
Mode	ω
1	2124
2	1552
3	666
4	383
5	238
6	205

Table 4.60: Dicyano

Harmonic Frequencies	
Mode	ω
1	2139
2	2138
3	452
4	412
5	335
6	242
7	205
8	194
9	91

Table 4.61: Isocyano

Harmonic Frequencies	
Mode	ω
1	2078
2	1526
3	677
4	419
5	199
6	162

Table 4.62: Diisocyano

Harmonic Frequencies	
Mode	ω
1	2086
2	2081
3	470
4	442
5	302
6	188
7	156
8	146
9	96

Table 4.63: Fluoro

Harmonic Frequencies	
Mode	ω
1	1392
2	651
3	640

Table 4.64: Difluoro

Harmonic Frequencies	
Mode	ω
1	669
2	637
3	250

4.7.2 AlH_3 Derivatives

Table 4.65: AlH_3

Harmonic Frequencies	
Mode	ω
1	1936
2	1936
3	1933
4	794
5	794
6	712

Table 4.66: Hydroxy

Harmonic Frequencies	
Mode	ω
1	3926
2	1968
3	1938
4	859
5	771
6	668
7	628
8	493
9	435

Table 4.67: Dihydroxy (in-in)

Harmonic Frequencies	
Mode	ω
1	3943
2	3941
3	2011
4	909
5	804
6	675
7	607
8	543
9	522
10	356
11	310
12	246

Table 4.68: Dihydroxy (in-out

Harmonic Frequencies	
Mode	ω
1	3937
2	3929
3	1988
4	923
5	795
6	688
7	625
8	571
9	516
10	376
11	343
12	235

Table 4.69: Dihydroxy (out-out)

Harmonic Frequencies	
Mode	ω
1	3940
2	3939
3	1961
4	938
5	780
6	693
7	628
8	535
9	511
10	364
11	308
12	245

Table 4.70: Amino

Harmonic Frequencies	
Mode	ω
1	3663
2	3573
3	1945
4	1941
5	1582
6	829
7	753
8	728
9	616
10	495
11	442
12	423

Table 4.71: Diamino

Harmonic Frequencies	
Mode	ω
1	3668
2	3667
3	3580
4	3580
5	1955
6	1586
7	1577
8	876
9	770
10	713
11	671
12	543
13	513
14	381
15	356
16	354
17	272
18	199

Table 4.72: Cyano

Harmonic Frequencies	
Mode	ω
1	2193
2	1998
3	1984
4	774
5	618
6	546
7	541
8	205
9	198

Table 4.73: Dicyano

Harmonic Frequencies	
Mode	ω
1	2199
2	2198
3	2037
4	673
5	592
6	522
7	492
8	337
9	213
10	199
11	186
12	86

Table 4.74: Isocyano

Harmonic Frequencies	
Mode	ω
1	2093
2	2002
3	1986
4	779
5	625
6	618
7	552
8	151
9	137

Table 4.75: Diisocyano

Harmonic Frequencies	
Mode	ω
1	2098
2	2085
3	2052
4	720
5	639
6	597
7	495
8	282
9	148
10	133
11	127
12	81

Table 4.76: Fluoro

Harmonic Frequencies	
Mode	ω
1	1980
2	1971
3	845
4	769
5	636
6	553

Table 4.77: Difluoro

Harmonic Frequencies	
Mode	ω
1	2036
2	926
3	781
4	656
5	503
6	264

4.7.3 AlH_4^- Derivatives

Table 4.78: AlH_4^-

Harmonic Frequencies	
Mode	ω
1	1729
2	1639
3	1639
4	1639
5	778
6	778
7	778
8	758
9	758

Table 4.79: Hydroxy

Harmonic Frequencies	
Mode	ω
1	3885
2	1718
3	1643
4	1608
5	816
6	798
7	772
8	724
9	660
10	568
11	527
12	70

Table 4.80: Dihydroxy (twist)

Harmonic Frequencies	
Mode	ω
1	3879
2	3879
3	1712
4	1656
5	790
6	770
7	759
8	714
9	682
10	641
11	587
12	481
13	299
14	181
15	134

Table 4.81: Amino

Harmonic Frequencies	
Mode	ω
1	3563
2	3480
3	1706
4	1645
5	1597
6	1562
7	807
8	799
9	758
10	743
11	627
12	573
13	489
14	388
15	117

Table 4.82: Diamino

Harmonic Frequencies	
Mode	ω
1	3549
2	3549
3	3469
4	3468
5	1699
6	1661
7	1562
8	1561
9	780
10	755
11	738
12	734
13	646
14	597
15	574
16	481
17	413
18	387
19	234
20	202
21	95

Table 4.83: Cyano

Harmonic Frequencies	
Mode	ω
1	2163
2	1784
3	1731
4	1731
5	779
6	773
7	773
8	552
9	552
10	438
11	234
12	234

Table 4.84: Dicyano

Harmonic Frequencies	
Mode	ω
1	2175
2	2175
3	1837
4	1811
5	772
6	715
7	570
8	527
9	482
10	460
11	336
12	241
13	237
14	220
15	90

Table 4.85: Isocyano

Harmonic Frequencies	
Mode	ω
1	2114
2	1787
3	1731
4	1731
5	791
6	780
7	780
8	560
9	560
10	479
11	187
12	187

Table 4.86: Diisocyano

Harmonic Frequencies	
Mode	ω
1	2120
2	2114
3	1846
4	1817
5	783
6	737
7	568
8	548
9	529
10	505
11	279
12	182
13	180
14	175
15	92

Table 4.87: Fluoro

Harmonic Frequencies	
Mode	ω
1	1733
2	1652
3	1652
4	818
5	783
6	783
7	671
8	569
9	569

Table 4.88: Diflouro

Harmonic Frequencies	
Mode	ω
1	1748
2	1686
3	799
4	789
5	699
6	665
7	571
8	568
9	250

CHAPTER 5

CONCLUSION

The dissertation presented here began with a review of methods and analyses used within computational quantum chemistry, with an emphasis on those used to obtain results in the studies presented. The following chapters presented the results for three studies that show the capabilities of methods to elucidate properties of chemical systems.

In Chapter 2, the results for the computation of relative energies of the rotamers of the *n*-propylperoxy radical were reported. Although these results had been obtained by lower-level method, we were able to refine the literature upon these relative energies. Energies were reported at the CCSDT(Q)/CBS level of theory Our results agreed with previous literature that the *gauche-gauce* conformer was the lowest in energy. The nearly isoenergetic *gauche-trans* was found to be only 0.12 kcal mol^{-1} higher in energy than the lowest energy conformer. The highest energy rotamer, the *trans-trans* rotamer, was reported to have a relative energy of only 0.57 kcal mol^{-1} at the CCSDT(Q)/CBS level with corrections added. It was discussed how the anharmonic zero-point vibrational energy served to separate the rotamers by the greatest amount of any of the corrections that were added during the focal point analysis. It was discussed how the rotamers would be very hard to distinguish spectroscopically due to their very similar vibrational frequencies. It was posited that the best way to differentiate the rotamers via vibration was to use the frequencies of the C–C stretching vibrations in conjunction with the accompanying harmonic intensities in order to accomplish rotamer specific detection.

In addition to vibrational frequencies, VPT2 methods were utilized to obtain the vibrationally averaged structures of the rotamers. Although all bonds showed a lengthening due to vibrations, it was found that the C–H bonds showed the largest increase in length. This was attributed to the fact that the hydrogen atoms are much lighter than the other atoms in the system and undergo larger amplitude motions. The larger amplitude motions are more affected by the anharmonicity of the associated potential energy surface causing the vibrational averaging to have the largest effect upon these bond lengths.

In Chapter 3, the linear, hydrogen-bonding hydrogen cyanide (HCN) dimer was investigated. The geometry for the dimer and monomer were computed at the CCSD(T)/cc-pCVQZ level of theory. These geometries were analyzed using Natural Bond Orbital (NBO) analysis. The monomer units within the dimer showed modest distortion. The largest difference was the C–H bond of the proton donor monomer extending from 1.0655 Å to 1.0718 Å. NBO analysis showed an increase in the population of the σ^* anti-bonding orbital of the monomer C–H. Other changes in bond lengths were attributed to electrostatics and smaller electron donation effects.

Another set of results reported within this study is the set of anharmonic frequencies for the parent isotopologue. The parent has been well studied and it was found that the fundamental frequencies reported agreed well with literature. The agreement between the C–H stretches computed an the literature values was particularly good although, better than can be typically attributed to the method used. The worst agreement with experiment was reported for the inter-monomer stretch which for which theory overestimated the fundamental frequency by roughly 10%. Our results were compared to recent harmonic theoretical results and found to be comparable though distinct due to the fact that our frequencies were corrected for anharmonicity. The effect of removing certain modes from the VPT2 analysis was observed to see if it would yield improvement in the fundamental frequencies compared to experiment. In particular, it was shown that removing ν_5 and ν_9 individually from the VPT2 anlaysis led to improvement of the other compared to experiment, but had deleterious effects upon the other modes.

Fundamental frequencies for substituted isotopologues were reported in Table 3.7. The frequencies were all computed using VPT2 at the CCSD(T)/cc-pCVQZ level of theory. The isotopic effects upon the computed frequncies was explained to be the result of changes in the reduced mass of vibrational modes. The largest changes in frequencies occured upon deuteration because this substitution led to the greatest change in reduced mass of modes.

Finally, the energy of the formation of the dimer was reported to be –3.93 kcal mol^{-1}. The pure electronic energy was well converged at the CBS/CCSDT(Q) using FPA. The resulting energy was shown to be in good agreement with recent calculations[60] as well as experiments.

Chapter 4 dealt with the carbenoid system known as the aluminyl anion. Related systems have been reported to have the ability to activate strong sigma bonds such as H–H bonds.[140–146] Within this dissertation, simpler forms of the carbenoid were studied in order to better understand the electronic effect of different substituents to the aluminyl anion. The geometries of all systems included in the chapter were computed at the aug-cc-pV(T+d)Z level of theory. The augmented functions were necessitated by the diffuse electronic cloud characteristic of anionic species. The geometries were further interrogated through the use of NBO anlaysis. The relatively non-electronegative aluminum nucleus within each species is shown to have a positive

natural charge due to the fact that each substituent studied here is more electronegative. The electrostatic attraction between the aluminum and the neighboring atoms had a distinct impact on the observed bond lengths and angles between substitutents. These geometries are reported in Tables 4.1, 4.2, and 4.4.

Another large section of the chapter was spent discussing two schemes for determining the relative energies of formations of substituted aluminyl anions. The first scheme was isodesmic in nature and yielded similar results as a similar scheme from the recent literature.[155] The other scheme, hypohomodesmotic in nature, showed vastly different results for the energies of formation for substituted aluminyl anions. The reasons for this discrepency were discussed within the paper and attributed mostly to the treatment of π delocalization effects.

BIBLIOGRAPHY

[1] Szabo, A.; Ostlund, N. S. *Modern Quantum Chemistry: Introduction to Advanced Electronic Structure Theory*; Dover Publications, Inc., 1996.

[2] Murphy, K. V.; Turney, J. M.; Schaefer, H. F. *J. Chem. Ed.* **2018**, *95*, 1572–1578.

[3] Čížek, J. *J. Chem. Phys.* **1966**, *45*, 4256–4266.

[4] Crawford, T. D.; Schaefer, H. F. *Reviews in Computational Chemistry*; 2007; pp 33–136.

[5] Allen, W. D.; Yamaguchi, Y.; Császár, A. G.; Clabo Jr., D. A.; Remington, R. B.; Schaefer, H. F. *Chem. Phys.* **1990**, *145*, 427–466.

[6] Clabo, D.; Allen, W. D.; Remington, R. B.; Yamaguchi, Y.; Schaefer, H. F. *Chem. Phys.* **1988**, *123*, 187–239.

[7] Weinhold, F.; Landis, C. *Valency and Bonding: A Natural Bond Orbital Donor-Acceptor Perspective*; Cambridge University Press.

[8] Weinhold, F. *NBO 5.0 Program Manual*; 2001.

[9] Reed, A. E.; Curtiss, L. A.; Weinhold, F. *CR* **1988**, *88*, 899–926.

[10] Foster, J. P.; Weinhold, F. *J. Am. Chem. Soc.* **1980**, *102*, 7211–7218.

[11] Ye, S.-Y.; Zhan, C.-G.; Wan, J.; Zhang, C.-J. *J. Mol. Struct.: THEOCHEM* **1994**, *313*, 231–236.

[12] Weinhold, F.; Landis, C. R. *Disocvering Chemistry with Natural Bond Orbitals*; John Wiley & Sons, Inc., 2012.

[13] Pyykko, P.; Desclaux, J. P. *Acc. Chem. Res.* **1979**, *12*, 276–281.

[14] Schuurman, M. S.; Muir, S. R.; Allen, W. D.; Schaefer, H. F. *J. Chem. Phys.* **2004**, *120*, 11586–99.

[15] Csaszar, A. G.; Allen, W. D.; Schaefer, H. F. *J. Chem. Phys.* **1998**, *108*, 9751.

[16] Allen, W. D.; East, A. L. L.; Császár, A. G. In *Structures and Conformations of Non-Rigid Molecules*; Laane, J., Dakkouri, M., Veken, B., Oberhammer, H., Eds.; Kluwer Adademic Pubishers, 1993; Chapter 10, pp 343–373.

[17] Dunning, T. H. *J. Chem. Phys.* **1989**, *90*, 1007–1023.

[18] Feller, D. *J. Chem. Phys.* **1993**, *98*, 7059.

[19] Helgaker, T.; Klopper, W.; Koch, H.; Noga, J. *J. Chem. Phys.* **1997**, *106*, 9639.

[20] DeSain, J. D.; Klippenstein, S. J.; Miller, J. A.; Taatjes, C. A. *J. Phys. Chem. A* **2003**, *107*, 4415–4427.

[21] Welz, O.; Burke, M. P.; Antonov, I. O.; Goldsmith, C. F.; Savee, J. D.; Osborn, D. L.; Taatjes, C. A.; Klippenstein, S. J.; Sheps, L. *J. Phys. Chem. A* **2015**, *119*, 7116–7129.

[22] Wilke, J. J.; Allen, W. D.; Schaefer, H. F. *J. Chem. Phys.* **2008**, *128*, 074308.

[23] Zádor, J.; Taatjes, C. A.; Fernandes, R. X. *Prog. Energy Combust. Sci.* **2011**, *37*, 371–421.

[24] Cord, M.; Husson, B.; Lizardo Huerta, J. C.; Herbinet, O.; Glaude, P.-A.; Fournet, R.; Sirjean, B.; Battin-Leclerc, F.; Ruiz-Lopez, M.; Wang, Z.; Xie, M.; Cheng, Z.; Qi, F. *J. Phys. Chem. A* **2012**, *116*, 12214–28.

[25] Merchant, S. S.; Goldsmith, C. F.; Vandeputte, A. G.; Burke, M. P.; Klippenstein, S. J.; Green, W. H. *Combust. Flame* **2015**, *162*, 3658–3673.

[26] Zhang, P.; Ji, W.; He, T.; He, X.; Wang, Z.; Yang, B.; Law, C. K. *Combust. Flame* **2016**, *167*, 14–23.

[27] Gallagher, S. M.; Curran, H. J.; Metcalfe, W. K.; Healy, D.; Simmie, J. M.; Bourque, G. *Combust. Flame* **2008**, *153*, 316–333.

[28] Ruiz, R. P.; Bayes, K. D. *J. Phys. Chem.* **1984**, *88*, 2592–2595.

[29] DeSain, J. D.; Taatjes, C. A.; Miller, J. A.; Klippenstein, S. J.; Hahn, D. K. *Faraday Discuss.* **2001**, *119*, 101–120.

[30] DeSain, J. D.; Clifford, E. P.; Taatjes, C. A. *J. Phys. Chem. A* **2001**, *105*, 3205–3213.

[31] Estupiñán, E. G.; Klippenstein, S. J.; Taatjes, C. A. *J. Phys. Chem. B* **2005**, *109*, 8374–87.

[32] Goldsmith, C. F.; Green, W. H.; Klippenstein, S. J. *J. Phys. Chem. A* **2012**, *116*, 3325–46.

[33] Taatjes, C. A. *J. Phys. Chem. A* **2006**, *110*, 4299–312.

[34] Savee, J. D.; Papajak, E.; Rotavera, B.; Huang, H.; Eskola, A. J.; Welz, O.; Sheps, L.; Taatjes, C. A.; Zádor, J.; Osborn, D. L. *Science* **2015**, *347*, 643–6.

[35] Zádor, J.; Huang, H.; Welz, O.; Zetterberg, J.; Osborn, D. L.; Taatjes, C. A. *Phys. Chem. Chem. Phys.* **2013**, *15*, 10753–60.

[36] Merle, J. K.; Hayes, C. J.; Zalyubovsky, S. J.; Glover, B. G.; Miller, T. A.; Hadad, C. M. *J. Phys. Chem. A* **2005**, *109*, 3637–46.

[37] Sharma, S.; Raman, S.; Green, W. H. *J. Phys. Chem. A* **2010**, *114*, 5689–701.

[38] Tarczay, G.; Zalyubovsky, S. J.; Miller, T. A. *Chem. Phys. Lett.* **2005**, *406*, 81–89.

[39] Zalyubovsky, S. J.; Glover, B. G.; Miller, T. A.; Hayes, C.; Merle, J. K.; Hadad, C. M. *J. Phys. Chem. A* **2005**, *109*, 1308–15.

[40] Adachi, H.; Basco, N. *Int. J. Chem. Kin.* **1982**, *14*, 1125–1138.

[41] Just, G. M. P.; Rupper, P.; Miller, T. A.; Meerts, W. L. *Phys. Chem. Chem. Phys.* **2010**, *12*, 4773–82.

[42] Agarwal, J.; Simmonett, A. C.; Schaefer, H. F. *Mol. Phys.* **2012**, *110*, 2419–2427.

[43] Copan, A. V.; Schaefer, H. F.; Agarwal, J. *Mol. Phys.* **2015**, *113*, 1–7.

[44] Li, C.; Agarwal, J.; Wu, C.-H.; Allen, W. D.; Schaefer, H. F. *J. Phys. Chem. B* **2015**, *119*, 728–735.

[45] Elliott, S. N.; Turney, J. M.; Schaefer, H. F. *RSC Adv.* **2015**, *5*, 107254–107265.

[46] Almlöf, J.; Taylor, P. R. *J. Chem. Phys.* **1987**, *86*, 4070.

[47] Pople, J. A.; Nesbet, R. K. *J. Chem. Phys.* **1954**, *22*, 571.

[48] Kjaergaard, H. G.; Garden, A. L.; Chaban, G. M.; Gerber, R. B.; Matthews, D. A.; Stanton, J. F. *J. Phys. Chem. A* **2008**, *112*, 4324–35.

[49] Stanton, J. F.; Gauss, J.; Harding, M. E.; Szalay, P. G. CFOUR, Coupled-Cluster Techniques for Computational Chemistry, a Quantum-Chemical Program Package Written by J.F. Stanton, J. Gauss, M.E. Harding, P.G. Szalay with contributions from A.A. Auer, R.J. Bartlett, U. Benedikt, C. Berger, D.E. Bernholdt, Y.J. Bomble, L. Cheng, O. Christiansen, M. Heckert, O. Heun, C. Huber, T.-C. Jagau, D. Jonsson, J. Juslius, K. Klein, W.J. Lauderdale, F. Lipparini, D.A. Matthews, T. Metzroth, L.A. Mück, D.P. O'Neill, D.R. Price, E. Prochnow, C. Puzzarini, K. Ruud, F. Schiffmann, W. Schwalbach, C. Simmons, S. Stopkowicz, A. Tajti, J. Vázquez, F. Wang, J.D. Watts and the integral packages MOLECULE (J. Almlöf and P.R. Taylor), PROPS (P.R. Taylor), ABACUS (T. Helgaker, H.J. Aa. Jensen, P. Jørgensen, and J. Olsen), and ECP routines by A. V. Mitin and C. van Wüllen. For the current version, see http://www.cfour.de.

[50] Agarwal, J. PyVPT2 is a vibrational anharmonicity program written in Python by J. Agarwal. Center for Computational Quantum Chemistry, University of Georgia, Athens, GA.

[51] Gonzales, J. M.; Pak, C.; Cox, R. S.; Allen, W. D.; Schaefer, H. F.; Császár, A. G.; Tarczay, G. *Chem. Eur. J.* **2003**, *9*, 2173–92.

[52] Dunning, T. H. *J. Chem. Phys.* **1989**, *90*, 1007.

[53] Kállay, M.; Gauss, J. *J. Chem. Phys.* **2005**, *123*, 214105.

[54] Kállay, M.; Gauss, J. *J. Chem. Phys.* **2008**, *129*, 144101.

[55] Handy, N. C.; Yamaguchi, Y.; Schaefer, H. F. *J. Chem. Phys.* **1986**, *84*, 4481.

[56] Sellers, H.; Pulay, P. *Chem. Phys. Lett.* **1984**, *103*, 463–465.

[57] Perera, S. A.; Bartlett, R. J. *Chem. Phys. Lett.* **1993**, *216*, 606–612.

[58] Cowan, R. D.; Griffin, D. C. *J. Opt. Soc. Am.* **1976**, *66*, 1010.

[59] Bender, C. F.; Schaefer, H. F. *J. Am. Chem. Soc.* **1970**, *92*, 4984–4985.

[60] Mihrin, D.; Jakobsen, P. W.; Voute, A.; Manceron, L.; Wugt Larsen, R. *Phys. Chem. Chem. Phys.* **2018**, *20*, 8241–8246.

[61] Bläsing, K.; Bresien, J.; Labbow, R.; Schulz, A.; Villinger, A. *Angew. Chem. Int. Ed.* **2018**, *57*, 9170–9175.

[62] Oró, J.; Kamat, S. S. *Nature* **1961**, *190*, 442–443.

[63] Loew, G. H. *Journal of Theoretical Biology* **1971**, *33*, 121–130.

[64] Moffat, J. B.; Tang, K. F. *Journal of Theoretical Biology* **1976**, *58*, 83–95.

[65] Ferris, J. P.; Hagan, W. J. *Tetrahedron* **1984**, *40*, 1093–1120.

[66] Nandi, S.; Bhattacharyya, D.; Anoop, A. *Chem. Eur. J.* **2018**, *24*, 4885–4894.

[67] Karpfen, A. *Chem. Phys.* **1983**, *79*, 211–218.

[68] Kofranek, M.; Lischka, H.; Karpfen, A. *Mol. Phys.* **1987**, *61*, 1519–1539.

[69] Chen, C.; Liu, M.-H.; Wu, L.-S. *J. Mol. Struct.* **2003**, *630*, 187–204.

[70] Adrian-Scotto, M.; Vasilescu, D. *J. Mol. Struct.* **2007**, *803*, 45–60.

[71] De Oliveira, B. G.; De Araújo, R. D. C. M. U.; Soares, V. M.; Ramos, M. N. *Journal of Theoretical and Computational Chemistry* **2008**, *07*, 247–256.

[72] McDowell, S. A. C.; Buckingham, A. D. *J. Chem. Phys.* **2010**, *132*, 064303.

[73] Brandão, I.; Rivelino, R.; Fonseca, T. L.; Castro, M. A. *Chem. Phys. Lett.* **2013**, *580*, 9–13.

[74] Roztoczyńska, A.; Kozłowska, J.; Lipkowski, P.; Bartkowiak, W. *Chem. Phys. Lett.* **2014**, *608*, 264–268.

[75] Cole, R. H. *J. Am. Chem. Soc.* **1955**, *77*, 2012–2013.

[76] Uyemura, M.; Maeda, S. *Bulletin of the Chemical Society of Japan* **1972**, *45*, 1081–1086.

[77] Jucks, K. W.; Miller, R. E. *J. Chem. Phys.* **1988**, *88*, 6059.

[78] Nauta, K.; Miller, R. E. *J. Chem. Phys.* **1999**, *111*, 3426.

[79] Dulmage, W. J.; Lipscomb, W. N. *Acta Cryst.* **1951**, *4*, 330–334.

[80] Kertész, M.; Koller, J.; Ažman, A. *Chem. Phys. Lett.* **1976**, *41*, 146–148.

[81] Legon, A. C.; Millen, D. J.; Mjöberg, P. J. *Chem. Phys. Lett.* **1977**, *47*, 589–591.

[82] Brown, R. D.; Godfrey, P. D.; Winkler, D. A. *J. Mol. Spec.* **1981**, *89*, 352–355.

[83] Buxton, L. W.; Campbell, E. J.; Flygare, W. H. *Chem. Phys.* **1981**, *56*, 399–406.

[84] Fillery-Travis, A. J.; Legon, A. C.; Willoughby, L. C.; Buckingham, A. D. *Chem. Phys. Lett.* **1983**, *102*, 126–131.

[85] King, C. M. *J. Chem. Phys.* **1968**, *48*, 1685.

[86] Pacansky, J. *J. Phys. Chem.* **1977**, *81*, 2240–2243.

[87] Barnes, A. J.; Orville-Thomas, W. J.; Szczepaniak, K. *J. Mol. Struct.* **1978**, *45*, 75–87.

[88] Walsh, B.; Barnes, A. J.; Suzuki, S.; Orville-Thomas, W. J. *J. Mol. Spec.* **1978**, *72*, 44–56.

[89] Knözinger, E.; Wittenbeck, R. *Infrared Physics* **1984**, *24*, 135–142.

[90] Knözinger, E. *J. Chem. Phys.* **1986**, *85*, 4881.

[91] Beichert, P.; Pfeiler, D.; Knözinger, E. *Berichte der Bunsengesellschaft für physikalische Chemie* **1995**, *99*, 1469–1478.

[92] Jones, W. J.; Seel, R. M.; Sheppard, N. *Spectrochimica Acta Part A: Molecular Spectroscopy* **1969**, *25*, 385–391.

[93] Wofford, B. A.; Bevan, J. W.; Olson, W. B.; Lafferty, W. J. *J. Chem. Phys.* **1986**, *85*, 105.

[94] Jucks, K. W.; Miller, R. E. *Chem. Phys. Lett.* **1988**, *147*, 137–141.

[95] Meyer, H.; Kerstel, E. R. T.; Zhuang, D.; Scoles, G. *J. Chem. Phys.* **1989**, *90*, 4623.

[96] Kerstel, E. R. T.; Lehmann, K. K.; Gambogi, J. E.; Yang, X.; Scoles, G. *J. Chem. Phys.* **1993**, *99*, 8559.

[97] Grushow, A.; Burns, W. A.; Leopold, K. R. *J. Mol. Spec.* **1995**, *170*, 335–345.

[98] Jameson, C. J.; Yang, W. *Journal of Theoretical Biology* **1972**, *35*, 247–257.

[99] Johansson, A.; Kollman, P.; Rothenberg, S. *Theor. Chem. Acc.* **1972**, *26*, 97–100.

[100] Kollman, P.; McKelvey, J.; Johansson, A.; Rothenberg, S. *J. Am. Chem. Soc.* **1975**, *97*, 955–965.

[101] Murrell, J. N.; Carter, S.; Halonen, L. O. *J. Mol. Spec.* **1982**, *93*, 307–316.

[102] Kofranek, M.; Karpfen, A.; Lischka, H. *Chem. Phys.* **1987**, *113*, 53–64.

[103] Tostes, J. G. R.; Taft, C. A.; Ramos, M. N. *J. Phys. Chem.* **1987**, *91*, 3157–3160.

[104] De Almeida, W. B.; Hinchliffe, A. *J. Mol. Struct.* **1989**, *198*, 17–30.

[105] Morgon, N. H.; Custodio, R.; Tostes, J. G. R.; Taft, C. A. *J. Mol. Struct.* **1995**, *335*, 11–23.

[106] King, B. F.; Farrar, T. C.; Weinhold, F. *J. Chem. Phys.* **1995**, *103*, 348.

[107] Alfredsson, M.; Ojamae, L.; Hermansson, K. G. *Int. J. Quant. Chem.* **1996**, *60*, 767–778.

[108] Rivelino, R.; Chaudhuri, P.; Canuto, S. *J. Chem. Phys.* **2003**, *118*, 10593.

[109] Wang, B. Q.; Li, Z. R.; Wu, D.; Hao, X. Y.; Li, R. J.; Sun, C. C. *J. Phys. Chem. A* **2004**, *108*, 2464–2468.

[110] Balle, T. J.; Flygare, W. H. *Rev. Sci. Instr.* **1981**, *52*, 33–45.

[111] Simmonett, A. C.; Schaefer, H. F.; Allen, W. D. *J. Chem. Phys.* **2009**, *130*, 044301.

[112] Chang, C.-H.; Agarwal, J.; Allen, W. D.; Nesbitt, D. J. *J. Chem. Phys.* **2016**, *144*, 074301.

[113] Glendening, E. D.; Badenhoop, J. K.; Reed, A. E.; Carpenter, J. E.; Bohmann, J. A.; Morales, C. M.; Weinhold, F. NBO 5.0. 2001.

[114] Glendening, E. D.; Weinhold, F. *J. Comp. Chem.* **1998**, *19*, 593–609.

[115] Glendening, E. D.; Weinhold, F. *J. Comp. Chem.* **1998**, *19*, 610–627.

[116] Glendening, E. D.; Badenhoop, J. K.; Weinhold, F. *J. Comp. Chem.* **1998**, *19*, 628–646.

[117] East, A. L. L.; Allen, W. D. *J. Chem. Phys.* **1993**, *99*, 4638–4650.

[118] Kutzelnigg, W. *Z. Phys. D* **1989**, *11*, 15–28.

[119] Kutzelnigg, W. *Z. Phys. D* **1990**, *15*, 27–50.

[120] Franke, R.; Kutzelnigg, W. *Chem. Phys. Lett.* **1992**, *199*, 561–566.

[121] Klopper, W. *J. Comp. Chem.* **1997**, *18*, 20–27.

[122] Tarczay, G.; Császár, A. G.; Klopper, W.; Quiney, H. M. *Mol. Phys.* **2001**, *99*, 1769–1794.

[123] Georgiou, K.; Legon, A. C.; Millen, D. J.; Mjoberg, P. J. *Proceedings of the Royal Society A: Mathematical, Physical and Engineering Sciences* **1985**, *399*, 377–390.

[124] McDowell, S. A. *Chem. Phys. Lett.* **2018**, *696*, 61–66.

[125] Maroncelli, M.; Hopkins, G. A.; Nibler, J. W.; Dyke, T. R. *J. Chem. Phys.* **1985**, *83*, 2129.

[126] Satoshi, K.; Takayanagi, M.; Nakata, M. *J. Mol. Spec.* **1997**, *413-414*, 365–369.

[127] Allen, H. C.; Tidwell, E. D.; Plyler, E. K. *J. Chem. Phys.* **1956**, *25*, 302–307.

[128] Buckingham, A. D.; Fan-Chen, L. *Int. Rev. Phys. Chem.* **1981**, *1*, 253–269.

[129] King, B. F.; Weinhold, F. *J. Chem. Phys.* **1995**, *103*, 333.

[130] Tacke, M.; Schnoeckel, H. *Inorg. Chem.* **1989**, *28*, 2895–2896.

[131] Dohmeier, C.; Robl, C.; Tacke, M.; Schnöckel, H. *Angew. Chem. Int. Ed.* **1991**, *30*, 564–565.

[132] Gauss, J.; Schneider, U.; Ahlrichs, R.; Dohmeier, C.; Schnoeckel, H. *J. Am. Chem. Soc.* **1993**, *115*, 2402–2408.

[133] Schulz, S.; Roesky, H. W.; Koch, H. J.; Sheldrick, G. M.; Stalke, D.; Kuhn, A. *Angew. Chem. Int. Ed.* **1993**, *32*, 1729–1731.

[134] Purath, A.; Dohmeier, C.; Ecker, A.; Schnöckel, H.; Amelunxen, K.; Passler, T.; Wiberg, N. *Organometallics* **1998**, *17*, 1894–1896.

[135] Sitzmann, H.; Lappert, M. F.; Dohmeier, C.; Üffing, C.; Schnöckel, H. *J. Organomet. Chem.* **1998**, *561*, 203–208.

[136] Cui, C.; Roesky, H. W.; Schmidt, H.-G.; Noltemeyer, M.; Hao, H.; Cimpoesu, F. *Angew. Chem. Int. Ed.* **2000**, *39*, 4274–4276.

[137] Baker, R.; Jones, C. *Coordination Chemistry Reviews* **2005**, *249*, 1857–1869.

[138] Jones, C.; Junk, P. C.; Platts, J. A.; Stasch, A. *J. Am. Chem. Soc.* **2006**, *128*, 2206–2207.

[139] Nagendran, S.; Roesky, H. W. *Organometallics* **2008**, *27*, 457–492.

[140] Chu, T.; Korobkov, I.; Nikonov, G. I. *J. Am. Chem. Soc.* **2014**, *136*, 9195–9202.

[141] Villegas-Escobar, N.; Gutiérrez-Oliva, S.; Toro-Labbé, A. *J. Phys. Chem. C* **2015**, *119*, 26598–26604.

[142] Crimmin, M. R.; Butler, M. J.; White, A. J. P. *Chem. Comm.* **2015**, *51*, 15994–15996.

[143] Zhang, X.; Cao, Z. *Dalton Trans.* **2016**, *45*, 10355–10365.

[144] Schoeller, W. W.; Frey, G. D. *Inorg. Chem.* **2016**, *55*, 10947–10954.

[145] Chu, T.; Boyko, Y.; Korobkov, I.; Kuzmina, L. G.; Howard, J. A. K.; Nikonov, G. I. *Inorg. Chem.* **2016**, *55*, 9099–9104.

[146] Hicks, J.; Vasko, P.; Goicoechea, J. M.; Aldridge, S. **2018**, *557*, 92–95.

[147] Yang, Z.; Zhong, M.; Ma, X.; De, S.; Anusha, C.; Parameswaran, P.; Roesky, H. W. *Angew. Chem. Int. Ed.* **2015**, *127*, 10363–10367.

[148] Yang, Z.; Zhong, M.; Ma, X.; Nijesh, K.; De, S.; Parameswaran, P.; Roesky, H. W. *J. Am. Chem. Soc.* **2016**, *138*, 2548–2551.

[149] Tan, G.; Szilvási, T.; Inoue, S.; Blom, B.; Driess, M. *J. Am. Chem. Soc.* **2014**, *136*, 9732–9742.

[150] Zidan, R.; Garcia-Diaz, B. L.; Fewox, C. S.; Stowe, A. C.; Gray, J. R.; Harter, A. G. *Chem. Comm.* **2009**, 3717.

[151] Graetz, J.; Reilly, J.; Yartys, V.; Maehlen, J.; Bulychev, B.; Antonov, V.; Tarasov, B.; Gabis, I. *Journal of Alloys and Compounds* **2011**, *509*, S517–S528.

[152] Metzler-Nolte, N. *New J. Chem.* **1998**, *22*, 793–795.

[153] Sundermann, A.; Reiher, M.; Schoeller, W. W. *Eur. J. Inorg. Chem.* **1998**, *1998*, 305–310.

[154] Tuononen, H. M.; Roesler, R.; Dutton, J. L.; Ragogna, P. J. *Inorg. Chem.* **2007**, *46*, 10693–10706.

[155] Eckhardt, A. K.; Schreiner, P. R. *Angew. Chem. Int. Ed.* **2018**, *57*, 5248–5252.

[156] Wheeler, S. E.; Houk, K. N.; Schleyer, P. v. R.; Allen, W. D. *J. Am. Chem. Soc.* **2009**, *131*, 2547–2560.

[157] Wheeler, S. E. *Wiley Interdisciplinary Reviews: Computational Molecular Science* **2012**, *2*, 204–220.

[158] Hehre, W. J.; Ditchfield, R.; Radom, L.; Pople, J. A. *J. Am. Chem. Soc.* **1970**, *92*, 4796–4801.

[159] Pople, J. A.; Radom, L.; Hehre, W. J. *J. Am. Chem. Soc.* **1971**, *93*, 289–300.

[160] Dunning, T. H.; Peterson, K. A.; Wilson, A. K. *J. Chem. Phys.* **2001**, *114*, 9244–9253.

[161] Wilson, A. K.; Dunning, T. H. *J. Phys. Chem. A* **2004**, *108*, 3129–3133.

[162] Matthews, D. A.; Stanton, J. F. *J. Chem. Phys.* **2015**, *143*, 204103.

[163] Shao, Y. et al. *Mol. Phys.* **2015**, *113*, 184–215.

[164] Rao, B. K.; Jena, P.; Burkart, S.; Ganteför, G.; Seifert, G. *Phys. Rev. Lett.* **2001**, *86*, 692–695.

[165] Kiran, B.; Jena, P.; Li, X.; Grubisic, A.; Stokes, S. T.; Ganteför, G. F.; Bowen, K. H.; Burgert, R.; Schnöckel, H. *Phys. Rev. Lett.* **2007**, *98*, 256802.